CHALMERS

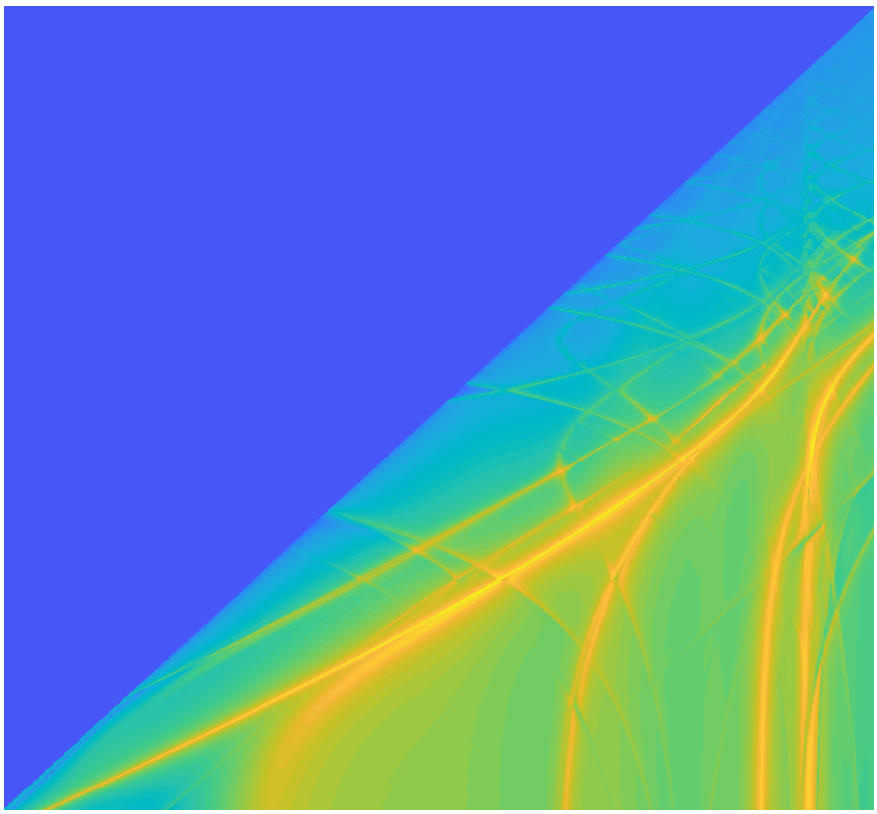

Modelling the acoustic performance of slab tracks

JANNIK THEYSSEN

Department of Architecture and Civil Engineering
Division of Applied Acoustics
CHALMERS UNIVERSITY OF TECHNOLOGY
Gothenburg, Sweden 2020

THESIS FOR THE DEGREE OF LICENTIATE IN
APPLIED ACOUSTICS

Modelling the acoustic performance of slab tracks

JANNIK THEYSSEN

Department of Architecture and Civil Engineering

Division of Applied Acoustics

CHALMERS UNIVERSITY OF TECHNOLOGY

Gothenburg, Sweden 2020

Modelling the acoustic performance of slab tracks
JANNIK THEYSSEN

Thesis for the degree of Licentiate
Series name: Lic / Architecture and Civil Engineering / Chalmers University of Technology

Department of Architecture and Civil Engineering
Division of Applied Acoustics
Chalmers University of Technology
SE-412 96 Gothenburg
Sweden
Telephone: +46 (0)31-772 1000

Cover:
Surface plot of the radiated sound power of a discretely supported rail, indicating high power levels by bright colours over frequency (horizontally) and wavenumber (vertically). The harmonic excitation is a point load acting vertically on the rail head. The axes are increasing from the bottom left. In the upper-left half of the plane, only near fields are created, which are exponentially decaying and thus not radiating outwards. The lower-right half shows radiation in the far field, where the bright lines roughly follow the dispersion curves of the different waves in the rail. The cut-on frequencies of these waves are visible as vertical lines. The repetitive pattern is an effect of the discrete support. The calculations were carried out using the implementations of the Waveguide Finite Element Method and Wavenumber Boundary Element Method used in this work.

Chalmers Reproservice
Gothenburg, Sweden 2020

Modelling the acoustic performance of slab tracks
Thesis for the degree of Licentiate in Applied Acoustics
JANNIK THEYSSEN
Department of Architecture and Civil Engineering
Division of Applied Acoustics
Chalmers University of Technology

Abstract

Transport is a major contributor to anthropogenic greenhouse gas emissions. Railway transport has a small footprint compared to other means of transport. This is one reason for the construction of new high-speed railway lines world-wide. These lines are often constructed using slab track technology, in which the traditional track configuration of concrete sleepers and ballast is replaced by concrete slabs. In earlier work, it has been found that traffic on slab tracks has higher noise emissions than on ballasted tracks. Rolling noise, radiated from wheels and track, is an important contributor to these noise emissions. To predict the acoustic performance of slab tracks, first, a model for the high-frequency vibration in these tracks is necessary, for which there is currently no standard solution. Further, the effect of the reflective slab track surface on the wheel radiation has not been researched.

In this work, a model for the high-frequency vibrations and acoustic radiation of slab tracks has been developed and implemented. The validity of the dynamic model has been tested on a full-scale test rig. The developed model was then used for researching the influence of track parameters on noise emission. In this investigation, the rail pad stiffness was identified to have a major influence. Besides, a model for the sound radiation of railway wheels over hard reflective surfaces was developed, implemented, and validated. The effect of the slab track surface on the radiation efficiency of the vibrating wheel was evaluated and found negligible. The developed models are steps towards predicting the rolling noise generated by rail vehicles on slab tracks, which is significant both for the planning of new lines and the investigation of potential abatement measures.

Keywords: slab track, railway noise, rolling noise, numerical modelling, acoustic optimisation

Preface

Anything that grows in nature can only reach its full potential when the surrounding conditions for its growth are ideal. Likewise, the work and development towards a Ph.D. will be most fruitful in a supportive environment. I would like to acknowledge the ones who are creating and sharing such an environment with me.

Thank you, Wolfgang and Astrid, you are an essential part of this environment. Wolfgang, I am grateful for our countless discussions in which your experience and knowledge helped to keep things in perspective, which made me grow both in my research and personal life. Thank you, Astrid, for your competent support, your comprehensive feedback, and your belief in my work, which makes it a pleasure to work with you.

Dear colleagues at Applied Acoustics, thank you for all the small chats and deep thoughts during coffee or tea, in between doors, in hallways, or (sometimes) on blackboards. Carl, thanks not only for all the idea-bouncing and maths-talk. Thank you Börje, Jens, Jens, Patrik, Hannes, Carmen, Fati, and Georgios, for your important contributions to our environment.

The work in this thesis has been accomplished from September 2019 to May 2020 at the Division of Applied Acoustics at Chalmers University of Technology within the research project VB13 "Noise from slab tracks". It has been a part of the research activities within the Centre of Excellence CHARMEC (CHAlmers Railway MEChanics). In particular, the support from Trafikverket (the Swedish Transport Administration) is acknowledged. Dear colleagues at CHARMEC, thank you for your support. Thank you, Emil, your systematic approach to problem solving, skilled diplomacy, and patience were vital. Jens, I am thankful for your encouragement, critical feedback, and expertise. I very much appreciate the fruitful discussions and valuable inputs from you, Anders Ekberg, Andreas Andersson, and Martin Li. Thank you, Monica Waaranperä and Martin Schilke, for seamless communication. I look forward to continued cooperation with all of you.

Dear friends and Ph.D.-colleagues at Chalmers, thank you for being such an active part of my environment, making me thrive in so many ways. To my friends in Germany and Sweden, I am grateful to have you in my life. And, most importantly, thanks and love to my family, unconditionally on my side in the ups and downs which life offers me to grow.

Steninge, May 2020

Jannik Theyssen

Thesis

This thesis consists of an extended summary and the following appended papers:

Paper A J. Theyssen, A. Pieringer and W. Kropp. The Influence of Track Parameters on the Sound Radiation from Slab Tracks. *Proceedings of the 13th International Workshop on Railway Noise (IWRN 2019)*, Ghent, Belgium (2019).

Paper B F. Fabre, J. Theyssen, A. Pieringer and W. Kropp. Sound Radiation from Railway Wheels including Ground Reflections: A half-space formulation for the Fourier Boundary Element Method. *Submitted for international publication* (2020).

Paper C J. Theyssen, E. Aggestam, S. Zhu, J. Nielsen, A. Pieringer and W. Kropp. Calibration and validation of two dynamic slab track modelling approaches using measurements from a full-scale test rig. *To be submitted for international publication* (2020).

The appended papers were prepared in collaboration with the co-authors. The author of this thesis was responsible for the major progress of the work including taking part in the planning of the papers, developing the theories and the numerical implementation, performing the numerical simulations and writing the papers. The development of parts of the methodology and parts of the implementation leading up to **Paper B** were carried out by François Fabre. The planning and realisation of the measurements, the numerical simulations and the writing of **Paper C** were conducted in close collaboration with Emil Aggestam.

Contents

Part I
Extended summary

1 Introduction

1.1 High-speed railway lines and slab tracks

In 2017, 24.6% of the total greenhouse gas (GHG) emissions in the European Union (EU) originated from transportation [1]. This sector is therefore a key focus to reducing GHG emissions. According to a 2011 White Paper by the European Commission [2], carbon emissions due to transport are to be reduced by 60% by 2050 with respect to 1990.

Figure 1.1 presents the total travelled distance in the EU by mode of transportation. While railway transport shows a constant, moderate increase, there is a large increase in air transport in the past decade. Considering the large CO_2 emissions from air transport per passenger-km in comparison to other means of transport, this indicates a need for a more resource efficient transport system[1]. High-speed rail connections could provide a viable alternative to some domestic flights for most European countries.

Today, rail transport is the fourth largest mode of passenger transport in the EU and plays a significant role in many other countries. In 2017, railways covered a share of 7.8% of passenger transport in the EU, of which 27% were high-speed connections [1]. It is clear that a more railway-focused transport system is envisioned by the EU: In the 2011 White Paper by the European Commission a key goal is a 50% shift of medium distance intercity passenger and freight journeys from road transport to rail and water-borne transport [2]. One step to achieving this shift is the continued construction and development of high-speed railway lines.

The development of high-speed railway lines started with the Japanese Shinkansen railway line, operating at a speed of 210 km/h, connecting Tokio and Osaka [3]. The definition of "high speed" has since then been increased to 250 km/h, and high-speed railway lines were introduced in many other countries such as France, Germany, and China [3]. In the last decade, the global traffic in high-speed railway lines has grown substantially, from 245 billion passenger-km (pkm) in 2010 to 956 billion pkm in 2018. This growth is to the largest part a product of the increased Chinese railway network (46 billion pkm in 2010 to 680 billion pkm in 2018) [4].

Ballasted tracks were used in the original Shinkansen line, building on earlier experience with this common type of track. Ballasted tracks are designed such that the rails are mounted on sleepers, which rest on a ballast layer. Sleepers are concrete or wooden

[1] The UIC states the equivalent carbon dioxide emissions for a 600 km trip to be 93 kg for air transport, 67.4 kg for transport by private car and and 8.1 kg for railway transport [3].

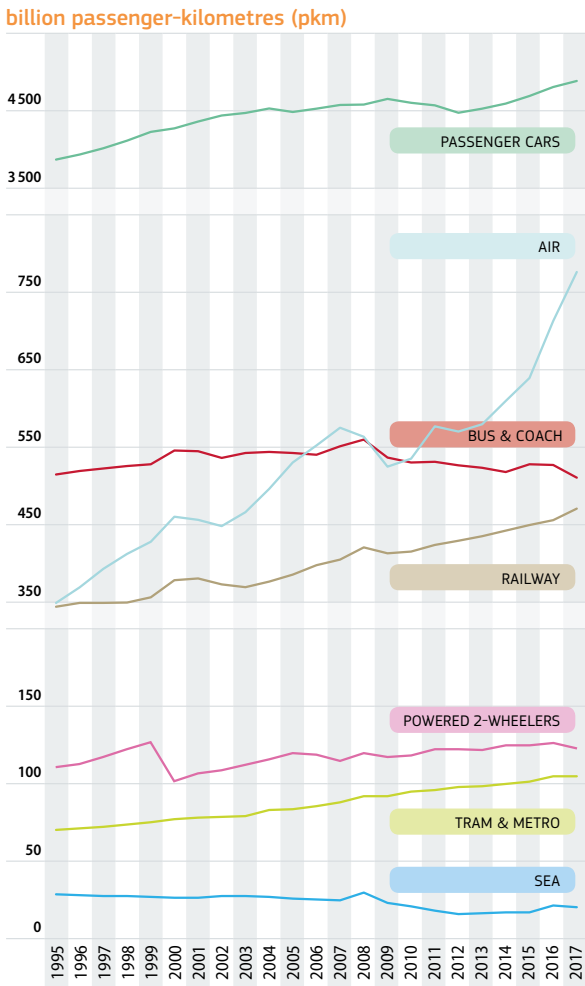

Figure 1.1: EU-28 performance for passenger transport 1995-2017, from [1].

beams which are placed perpendicularly to the track direction such that they connect both rails. The ballast layer can undergo geometrical alteration during use, creating a need for frequent and costly maintenance [5, 6].

In order to mitigate this geometrical deterioration, new tracks were developed in which the sleepers were replaced with large concrete panels. These so-called slab tracks or ballastless tracks are railway tracks in which the rails are supported by a solid, often concrete structure that connects both rails and extends parallel to the track. The stiffer support leads to a longer lifetime and reduced maintenance, and therefore higher availability of the line [6]. Slab track sections were first introduced into the Shinkansen line in 1972 and are now extensively used for high-speed railway lines in e.g. China, Japan and Germany.

There are challenges in the design of new high-speed railway lines using slab tracks. A main factor next to the higher construction costs are the lower noise and vibration absorption of this type of track compared to ballasted track [6]. This can lead to a higher noise exposure for residents.

1.2 Challenges: Noise from traffic on slab tracks

Traffic noise is a major health concern. Its effect on humans is quantified by indicators like the L_{den}, a noise indicator used to assess annoyance during day, evening and night, and the L_{night}, which is used to assess sleep disturbance. These parameters measure a long-term average exposure on residents as defined in ISO 1996-1:2016(E) [7]. The World Health Organisation (WHO) recommends an exposure of less or equal to ($L_{\text{den}}/L_{\text{night}}$) 53/45 dB for road traffic, 54/44 dB for rail, 45/40 dB for air traffic. However, according to the UIC, more than 18 million people are exposed to noise levels (L_{den}) larger than 55 dB [8]. The L_{den} indicator increases with an increasing number of trains per day on a given track. In combination with the envisioned railway-focussed transport, a reduction of $L_{\text{den}}/L_{\text{night}}$ can only occur by reducing or absorbing the noise radiated by individual vehicles and tracks.

To reduce the noise radiated by individual vehicles, an understanding of the processes involved in noise generation is necessary first. In general, railway rolling noise occurs due to the interaction of the rail and the moving wheel, in which the surface roughness of both components excites structural vibrations and ultimately noise. The vertical excitation of wheel and rail is the predominant source for rolling noise [9]. The two components interact in the contact patch, a small area in which the roughness of the surfaces influences the vibrations [10]. Wavelengths that are short in comparison to the contact patch, or in the same order as the contact patch, excite the wheel/rail system less effectively than longer wavelengths [11, 10]. This is called the contact filter effect. If the interaction in the contact patch is simplified to a single Hertzian spring in numerical models, the contact filter effect has to be added explicitly [12, 13, 14, 10]. The wavelength in the roughness spectrum is coupled to the excited frequency by the speed of the moving wheel. For high-speed railway lines, it is known that the noise from the rails and the wheels dominates over other sources, for example aerodynamic noise from the pantograph, at

least up to 300 km/h [15, 16], at relevant frequencies for human perception. Although this is not specific to ballast-less tracks, it shows the necessity to focus on the wheels, the rail and the track as noise sources in a wide speed range.

Some challenges in the understanding and modelling of the radiation from wheels and rails on slab tracks are stated below. The first question when focussing on slab tracks is the comparison to ballasted tracks. Even though extensive measurement campaigns and detailed simulation models have been used to quantify the increase in noise radiation, there is no simple way to quantify the difference between ballasted tracks and slab tracks. Related to this point is a second challenge: a large body of research exists for the key parameters that influence the sound radiation from ballasted tracks. However, it is not clear that these parameters will have the same effect on slab tracks. In order to e.g. evaluate mitigation measures, an investigation of these parameters is relevant. Thirdly, when researching the high-frequency vibro-acoustic properties of slab tracks, accurate numerical models can give further insights. The large size of the structure makes it costly to use detailed numerical models. Finally, with the slab track surface in close proximity to the vibrating wheel, the radiation efficiency of the wheel can be affected. This effect is not as relevant in ballasted tracks, since the ballast does not have an acoustically hard surface (the air in the ballast has absorptive character). This could, for wheels on slab tracks, lead to an increase of the pass-by sound pressure level not only due to the lacking decrease due to ballast absorption but also due to a more efficient sound radiation. These challenges are addressed in the following.

1.3 Overview

1.3.1 Context

This thesis aims to improve modelling approaches to solving vibro-acoustic issues related to rolling noise generation on different slab track. The components involved in the noise generation are the rail, the rail support (i.e. sleepers or a slab) and the wheels. Often, four stages of the calculation process can be found in models. Figure 1.2 shows these four stages in the calculation process.

1. *The frequency response functions* - The dynamic properties of the wheel and the rail are pre-calculated and used in the following two steps. Typical input parameters are the geometry, material data and information about the contact positions. The dynamic response can include support systems, e.g. the wheel suspension or sleepers.

2. *The contact problem* - The complex interaction of the rail and the wheel in their contact needs to take the combination of their individual roughnesses into account. The contact forces can be calculated based on an interaction model, which serve as input to the structural vibrations. Input parameters typically also include the wheel load and vehicle speed.

3. *The structural vibration* - The structural response of the wheel and the rail to the contact forces is calculated using the receptances and forces from the two earlier steps.

4. *The sound radiation* - Based on the vibrations, the sound radiation from both the wheels and the track is calculated. Their contributions are summarised at an observer position.

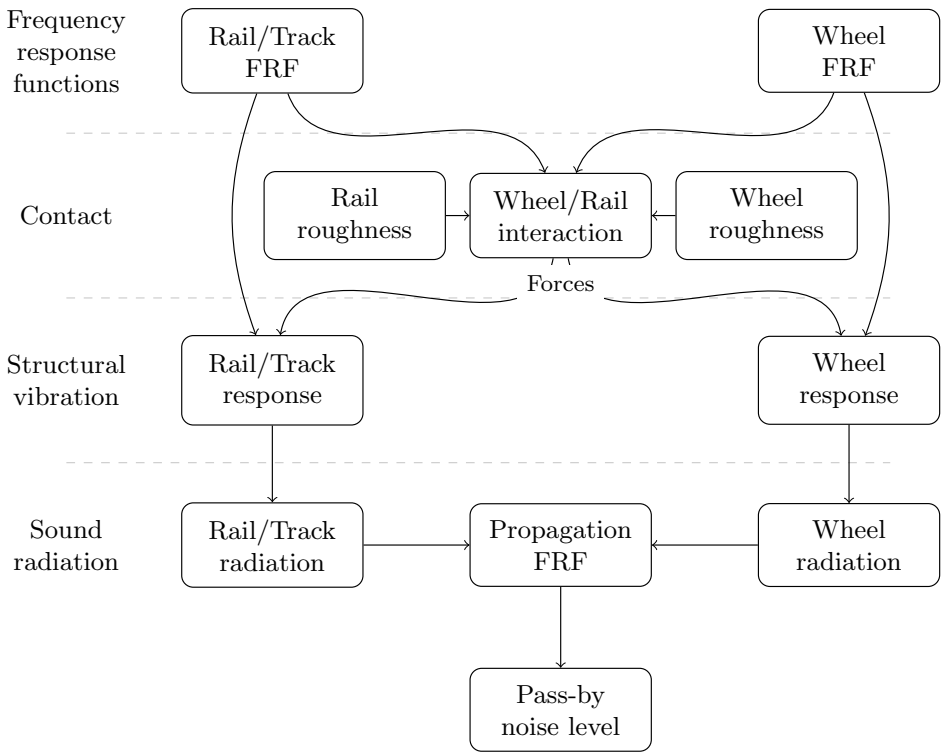

Figure 1.2: Visualisation of the components involved in railway rolling noise modelling. A large focus in this thesis is the evaluation of the frequency response functions (FRF).

A model of this type is visualised by Remington in [17], however the concept is already used in [12]. Every stage in this model can be evaluated using different methods, as e.g. the contact can be solved in frequency or time-domain, and the frequency response functions can be solved using analytical models or numerical models as Finite Element Method (FEM) in spatial or Waveguide FEM (WFEM) in wavenumber-domain. In [17], analytical models are used in all four steps based on earlier research, e.g. by Munjal et al. for the track [18] and for the wheel [19]. A model of this type is also presented in [13], in which numerical models for all stages are introduced. The modularity of this approach

allows e.g. introducing a new type of track or a different wheel radiation characteristic. This modularity is used in this thesis to address the challenges mentioned in Section 1.2.

1.3.2 Objectives

This thesis is focused on the development of appropriate models for the noise radiation from slab tracks and wheels above slab tracks. These models are then applied to deepen the understanding of their acoustic properties. The key objectives are

- to develop a numerical method for predicting the vibration in slab tracks,
- to predict the sound radiation from slab tracks,
- to predict the sound radiation from wheels over reflective surfaces, and
- to identify key track parameters for the noise radiation from slab track.

1.3.3 Outline

This thesis is structured as follows:

Chapter 2 presents existing work about the increase in rolling noise from trains on slab tracks compared to ballasted tracks.

Chapter 3 presents models for the dynamic response of the track. In Section 3.1, an overview over existing slab track systems is presented. Out of these, the most relevant system for this thesis is selected. A methodology for evaluating the dynamic response of this track system is developed in **Paper A** and summarised in Section 3.2. The model is calibrated and validated in **Paper C**. Using this model, a method for calculating the noise emissions from slab tracks is introduced in Section 3.3, which is presented in **Paper A**.

Analogously, in Chapter 4, the wheel dynamics and noise are described. It is focussing on the dynamic response in Section 4.1 and the noise radiation in Section 4.2. This chapter builds on **Paper B**, in which a methodology to simulate the dynamic response as well as the acoustic radiation from railway wheels is developed.

Finally, the appended papers are summarised in Chapter 5. Chapter 6 concludes this work and Chapter 7 gives a perspective on future work.

2 The rolling noise generated on slab tracks compared to ballasted tracks

The research of acoustical differences between ballasted and slab tracks has been a major focus in the last two decades due to the increased application of slab tracks in high-speed railway lines. In the year 2000, the project "acoustical innovative ballast-less track design" (AIFF) carried out in Germany was presented by Diehl et al. [20]. In the publication, it is stated that based on simulations, a significant difference in the noise level between the two track types for interior noise and the structure-borne noise on the rail is found. Further, increased sound radiation from the rails was found in the frequency range 500 Hz to 1500 Hz predominantly due to the higher vibration levels in the rail at these frequencies. The higher vibration level was discovered to be due to the significantly lower damping of the rail due to the lower rail pad stiffness. As a result of this project, an optimised track including a sleeper base with increased damping was presented.

Parallel to that, in the Netherlands, there was the project "Stiller Treinverkeer" (silent railway traffic), focussing on the same issue. It is stated that a ballast-less track is expected to lead to a 3 dB(A) higher noise radiation. With the help of numerical models, an acoustically optimised track was developed [21], which showed a potential reduction of between 4 dB(A) and 6 dB(A) compared to ballasted track. The German prediction model "Schall 03 2006", presented by Moehler et al. [22], estimates an increase of about 4 dB(A) to 2 dB(A) for slab tracks compared to ballasted tracks for an ICE 1, decreasing with increasing speed. In [23], the difference is found to be about 3 dB(A) in sound pressure level when measured at 25 m distance from the track. For one specific case, three factors were identified as reasons for this, being (i) a difference in rail roughness due to different maintenance, (ii) a difference in the track decay rate, and (iii) the change in propagation path due to reflections from the slab. In addition to the lower fastening stiffness, Gautier [6] gives a second reason for the increase in noise radiation from slab tracks. The noise absorption, which the ballast in a ballasted track provides, is replaced with a surface that acts as a pure noise reflector. A recommendation is given to address the noise issue by following a comprehensive system approach in future designs. In [24], these differences are researched based on numerical models. It is found that the resulting differences strongly depend on the initial assumptions about the track, such as the rail roughness and the track decay rate. Furthermore it is pointed out that the ground conditions adjacent to the track affect the pressure spectra.

3 Slab track dynamics and noise modelling

This section covers the track related components of the modelling approach described in Section 1.3.1. First, existing non-ballasted tracks are categorised in Section 3.1. Then, relevant models for the structural vibration and the sound radiation from non-ballasted tracks are discussed in Section 3.2, which includes the model developed in this work. Finally, the developed method of calculating the noise from slab tracks is presented in Section 3.3.

3.1 Slab track systems

In the following, a short overview and categorisation of existing slab track systems is given. For a more extensive description of the tracks, see e.g. Esveld [5]. This summary follows Figure 3.1.

The systems are first categorised by how the rail is supported along the track, which can be either continuous or discrete. Some systems use a continuous rail support. The rail is then either discretely clamped on or embedded in an elastomeric material. Thus, there is no periodic variation in track stiffness as in a discretely supported rail. This lowers the dynamic loads [25]. In embedded rail systems (ERS) as e.g. produced by edilon)(setra or the Balfour Beatty system, the rail is enclosed by an elastic compound, see Figure 3.2a. As shown in [15], this has significant benefits in terms of noise reduction. An example of a system with a discretely clamped and continuously supported rail is the Cocon track [5]. Due to the rail support being poured in-situ, there is little possibility for readjusting the rail, which is one major downside of this system.

In high-speed railway lines built using slab tracks, discrete support systems dominate, either with or without sleepers. These can be differentiated by how the sleepers are mounted. Three types of sleeper mounts are presented in the following. Firstly, one of the more commonly used systems is the RHEDA system, in which the rail is attached by pre-cast twin-block sleepers. The sleepers are embedded in a reinforced concrete slab resting on a hydraulically bonded layer [26]. Secondly, there are designs in which the sleeper is not embedded, for example the Getrac system [27]. Here, pre-stressed concrete sleepers are anchored on an asphalt layer, which rests on several support layers, possibly including hydraulically bonded layers. The sleepers can also be anchored on a concrete panel (Beton-Tragschicht mit Direktauflagerung, BTD). A strength of this system is its fast installation. And thirdly, another approach is to mount individual or twin-block sleepers on an elastic material, which itself is embedded in a concrete panel. This is the case in the STEDEF or Sonneville-LVT systems [6].

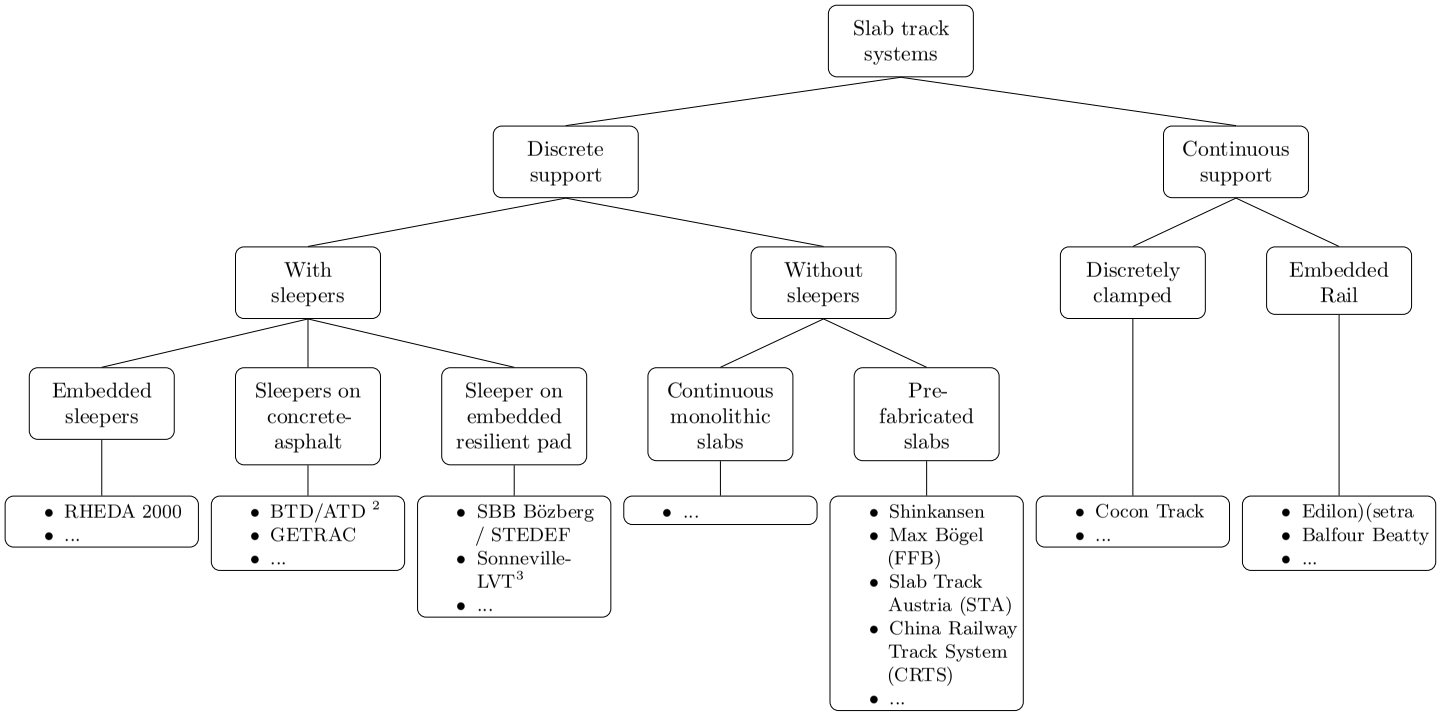

Figure 3.1: Categorisation of slab track systems.

[2]**B**eton-/**A**sphalt **T**ragschicht mit **D**irektauflagerung (Sleepers resting on concrete layer)
[3]Low vibration track

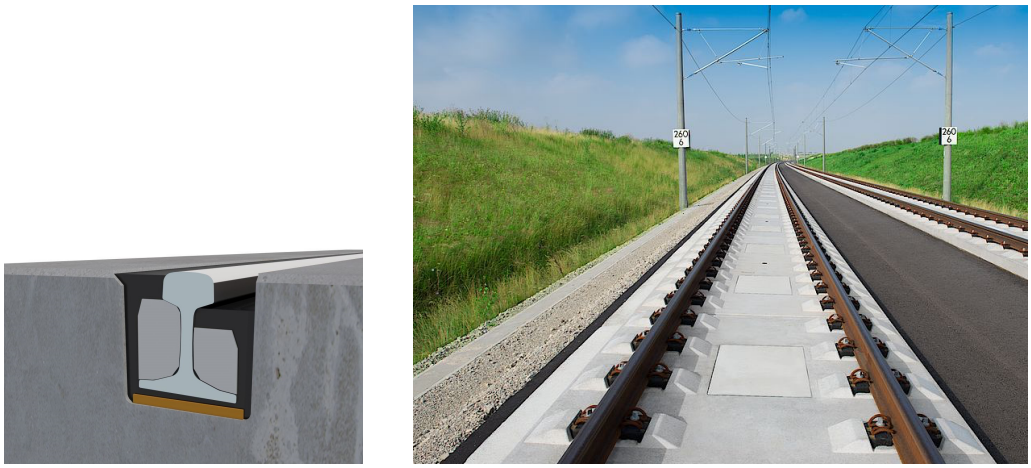

(a) (b)

Figure 3.2: Different types of slab track. (a) A sketch of a continuously supported, embedded rail (from [29]). (b) A slab track system with discrete rail supports without sleepers and pre-fabricated slabs called Slab Track Austria (from [30])

Systems without sleepers can either be continuous monolithic slabs, which are typically produced in-situ, or pre-fabricated slabs. Monolithic structures are rarely used to cover large distances but are well suited for civil structures like bridges [25]. Systems using pre-fabricated slabs are very commonly used in high-speed railway lines [6]. With the introduction of the SHINKANSEN train in Japan in 1964 [3], these systems have been continuously developed. Today, the German Max Bögel system, the Austrian system developed by ÖBB and the company PORR called Slab Track Austria (STA) and the Chinese CRTS series CRTS I – CRTS III are commonly used in high-speed slab track lines worldwide [6, 28]. Figure 3.2b shows an example of the STA system, representing the group of pre-fabricated slabs. In this work, the focus is mainly on the latter types of slab track. Figure 3.3 shows the setup of the CRTS III system, consisting of the pre-fabricated slabs resting on several different base layers. In this system, the slab sections are typically in the order of 5 m in length.

3.2 Slab track dynamics

Different applications require different levels of detail when modelling railway tracks. For the goal of simulating vehicle system dynamics, a (rigid) multi-body dynamics model can be sufficient [6]. This is largely due to the comparatively low upper frequency limit. For in-depth analysis of the structural behaviour of the track, such as internal stresses, a full Finite Element model of the track often necessary [25]. The rail can be approximated by Timoshenko beam elements if the upper frequency limit is not higher than about 1 kHz,

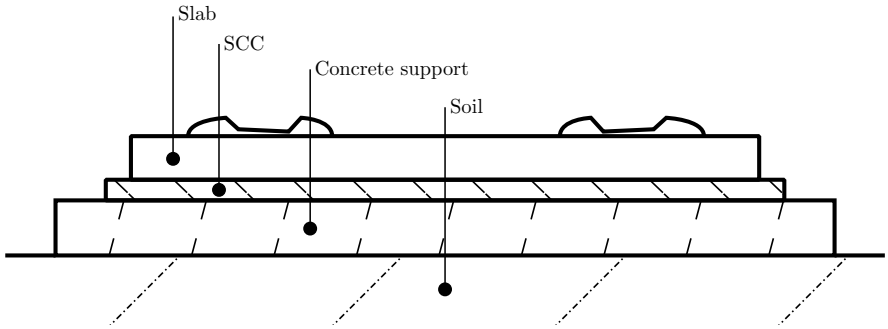

Figure 3.3: Cross section of a CRTS III slab track system. The slab rests on a layer of self-compacting concrete (SCC). Setup according to [28].

since below that, the cross-sectional deformation and vertical/lateral cross-coupling are small [31]. For the application of predicting structural vibrations and simulate noise radiation, the frequency range of human hearing becomes relevant, and therefore the beam model is no longer a good approximation. According to Thompson [15], the largest contributions from the rail to the radiated sound pressure level in a pass-by measurement can be expected below 3 kHz. In this section, numerical models of the structural dynamics of rails, aiming for simulating sound radiation, are presented. Dynamical models for calculating slab track behaviour are not readily available, and an approach to solving this issue is presented in the attached papers.

One of the first numerical models for the structural dynamics of the rail was a finite element (FE) based model that has been introduced by Thompson [32]. Here, a rail section was modelled with shell elements and symmetric and/or anti-symmetric boundary conditions on both ends to represent an infinite extent of the rail. A different FE-based approach, assuming wave propagation along the free rail, was introduced by Gavric et al. [33]. This approach makes use of the fact that the rail has a constant cross-section over its length and it thus acts as a waveguide. This approach is called the waveguide finite element (WFE) method[4]. This has the disadvantage that the rail either needs to be modelled free in space or with a continuous support condition over the whole length. However, in practice, the rail seats provide a coupling of the rail in discrete points along the rail. The issue of the discrete coupling is addressed in the spatial domain for a rail based on Timoshenko beam theory by Heckl et al. [34] and again in the wavenumber domain using a waveguide finite element model by Sheng et al. [35]. A combination of the wavenumber domain and the spatial domain is used by Zhang et al. [36].

Nilsson et al. [37] use the WFE method to reproduce the modal, high-frequency behaviour of a rail on a continuous support. In addition, the wavenumber boundary element method (WBEM) is applied to better capture the acoustic radiation from the

[4]The WFE method is sometimes called a 2.5D FE method, however, there is no reduction in dimensionality when transforming to the wavenumber domain. This approach will thus be referred to as the WFE method.

track along the length of the track. The presented method of combining the waveguide finite element method and the wavenumber boundary element method is frequently used to investigate the noise radiation of the rail (see e.g. [38, 39, 40]).

The presented papers **Paper A** and **Paper C** address the issue of a lacking, high-frequency model for slab track. In the WFE method, there is a considerable reduction of required degrees of freedom when reducing the mesh from 3D to 2D, which makes this method computationally advantageous when calculating large structures like the superstructure of a railway track. In this work, the WFE method has been implemented in an in-house code as described by Nilsson et al. [37]. This software has been applied to model both the vibrations in the rail as well as the rest of the superstructure. A method of introducing the discrete coupling between the two models has been implemented similar to the method presented by [36].

In this Section, the implemented WFE model of the rail is first compared to measurements of a ballasted track to validate the model and implementation for its use in rails. Then, a validation for the use of the WFE method to model the dynamic properties of the slab track is presented in a summary in **Paper C**.

3.2.1 WFE rail on simple support

For high-frequency vibrations, above about 1 kHz to 2 kHz depending on the rail and support stiffness, the rail is mostly decoupled from the vibrations in supporting structures like sleepers or slab. The receptance of the track then mainly depends on the receptance of the free rail. For frequencies below that, the receptance of the track is a product of the interaction between all the elements in the track superstructure. Nevertheless, a rather simple support model can accurately represent the track receptance in a large frequency range. This is shown in this section by creating a model of a UIC 60 rail using the implemented WFE method. This model is coupled to a simple support as described below, and compared to a measurement of a ballasted track, which was carried out by Thompson et al. [41] as part of the Roll2Rail project.

The WFE rail is coupled to an analytically calculated receptance in both vertical and lateral direction in three points across the foot of the rail. Along the track, the rail is coupled in 159 locations, using the concept described by Zhang et al. [36]. The analytical receptances are based on the assumption that the ballast and rail pad can be approximated by linear springs and the sleeper can be approximated by a simple mass. Damping is introduced by using a complex stiffness. Table 3.1 lists the parameters of the support and the rail. A principal sketch of the setup is shown in Figure 3.4. Note that only the elements relevant for the vertical direction are presented; an identical setup of springs exists for the lateral direction.

The receptance α is the chosen frequency response function to describe the response of the track. It is defined as the displacement η normalised with the harmonic force input F, $\alpha = \eta/F$. The derivation of the analytical expression for the receptance of the support is carried out in four steps following Figure 3.5.

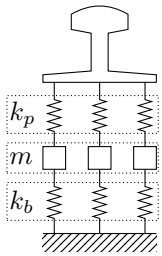

Figure 3.4: A principal sketch of the model setup.

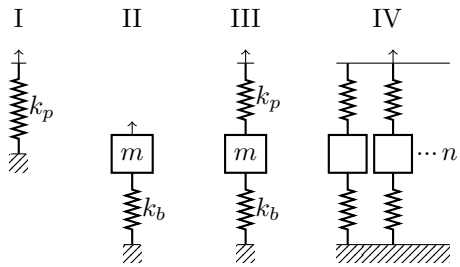

Figure 3.5: Steps in the derivation of the analytical expression for the foundation receptance at each contact node.

The receptance of the rail pad is modelled as a linear spring, thus the receptance is expressed as

$$\alpha_I = \frac{1}{k_p} \tag{3.1}$$

with the pad stiffness k_p. With the assumption of stationary harmonic excitation, the receptance at the top of the sleeper resting on the ballast is expressed as

$$\alpha_{II} = \frac{1}{k_b - m\omega^2} \tag{3.2}$$

with the ballast stiffness k_b and half the sleeper mass m. It is assumed that only half of the sleeper mass contributes to the dynamic system response. Coupling the receptances α_I and α_{II} in series is expressed as an addition,

$$\alpha_{III} = \frac{1}{k_p} + \frac{1}{k_b - m\omega^2} = \frac{k_p + \left(k_b - m\omega^2\right)}{k_p\left(k_b - m\omega^2\right)}. \tag{3.3}$$

This receptance could for example be used in combination with a single DOF beam model of the rail. However, the WFE produces results for flexural waves in three dimensions, so connecting a single degree of freedom along the width of the rail foot to α_{III} is likely inaccurate at higher frequencies. The continuous contact between the rail foot and the rail pad in lateral direction is instead approximated by coupling multiple (n) degrees-of-freedom (DOF) along the rail foot to the foundation.

Table 3.1: Parameters included in the simple support model.

	unit	vertical	lateral
Rail pad stiffness k_p	kN/mm	114	15.4
Rail pad damping coefficient η_p	-	0.25	0.08
Ground stiffness k_b	kN/mm	58	3.5
Sleeper mass m_s	kg	140	
Rail density ρ	kg/m^3	7850	
Rail poisson ratio ν	-	0.3	
Rail damping coefficient η	-	0.001	
Rail Young's modulus E	MPa	210	

However, coupling the rail to the receptance α_{III} multiple times does not produce the correct foundation stiffness. The partial receptance of each parallel strand α_{part} is introduced as a scaled version of α_{III} in order to achieve $\alpha_{IV} = \alpha_{III}$. With n identical (non-scaled) receptances α_{III} in parallel, their combined receptance α_{IV} is

$$\frac{1}{\alpha_{IV}} = n\frac{1}{\alpha_{III}} \rightarrow \alpha_{IV} = \frac{\alpha_{III}}{n}. \tag{3.4}$$

Thus, to approximate the receptance α_{III} with the setup in Figure 3.4, the partial receptance of each parallel strand needs to be multiplied with the number of strands n. The partial receptance α_{part} in one strand is thus described by

$$\alpha_{\text{part}} = n\alpha_{III} = \frac{n(k_p + k_b - \omega^2 m)}{k_p(k_b - \omega^2 m)} \tag{3.5}$$

where in this case, $n = 3$. The complex stiffness of the rail pad is evaluated as $k_p(1 + j\eta_p)$ and likewise for the ballast stiffness.

Figure 3.6 shows the implemented WFE model of the UIC 60 rail on ballasted track compared to the measurement [41] in terms of the vertical receptance. A close match is found between the measurement and the model. Especially the high-frequency behaviour of the rail is captured well. The same comparison is made for the lateral direction. In Figure 3.7, a very good correlation is found between the lateral rail receptances in the frequency range up to about 7 kHz. It is especially notable that the modal behaviour of the rail is captured well throughout this range.

One way to evaluate the decay of the vibration along the rail is the track decay rate. This quantity can especially be used as an indicator to estimate the noise emissions from the track [42]. Figures 3.8 and 3.9 show a comparison of the modelled and measured track decay rate and a close match is found here as well. In conclusion, it is found that the WFE model in combination with a simple analytical receptance for the support can provide a very good estimate of the behaviour of a ballasted track in the frequency range above about 80 Hz.

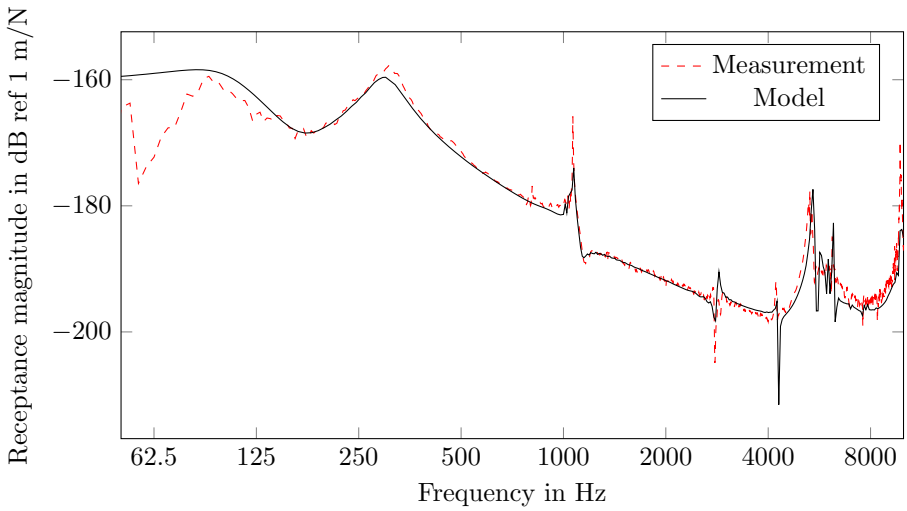

Figure 3.6: Vertical receptance of a UIC 60 rail on a ballasted track. The curve shows the vertical displacement response of the rail head when excited and measured at mid-span. A close match is achieved using the WFE model on a simple support.

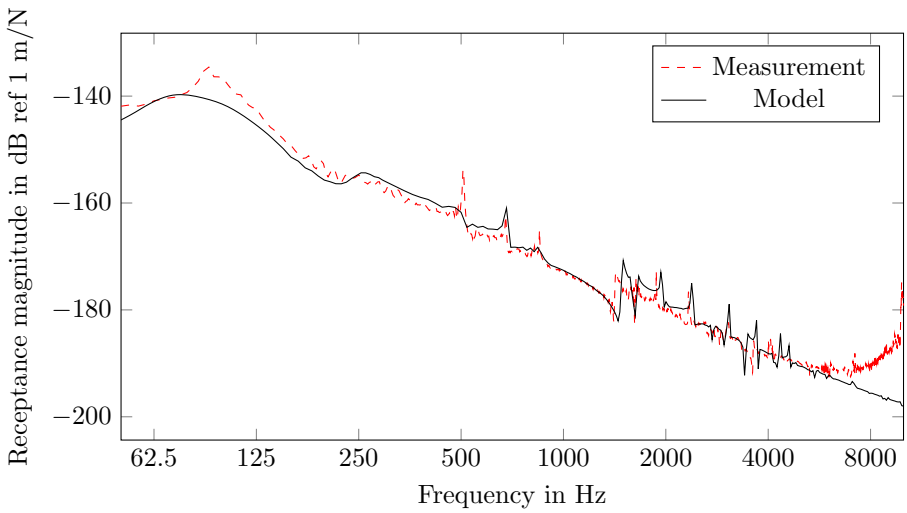

Figure 3.7: Lateral receptance of a UIC 60 rail on a ballasted track. The curve shows the lateral displacement response of the rail head when excited and measured at mid-span. A close match is achieved using the WFE model on a simple support.

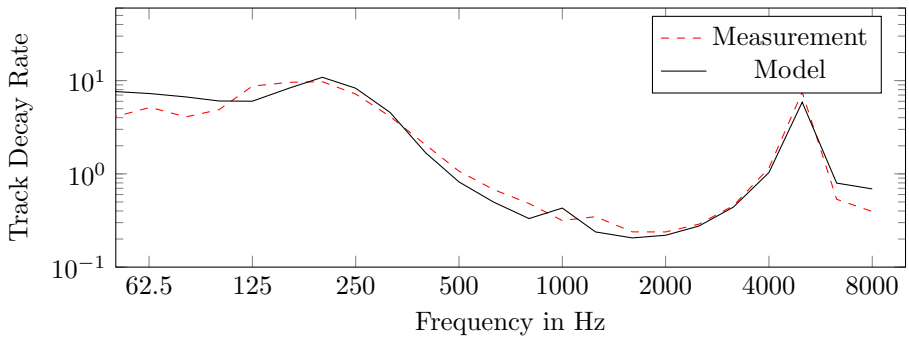

Figure 3.8: Vertical track decay rate of model and measurement.

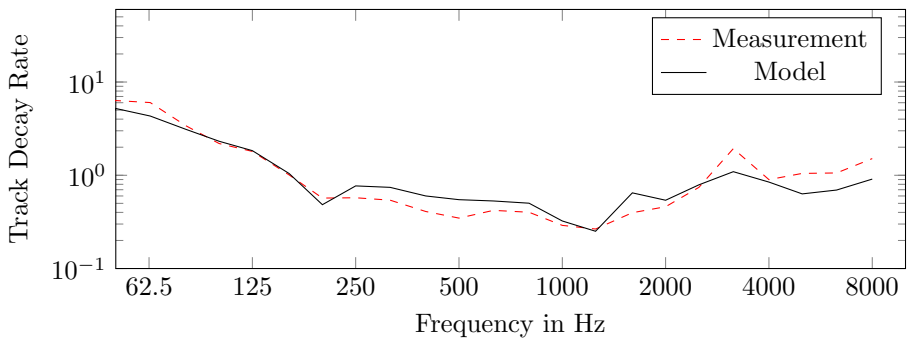

Figure 3.9: Lateral track decay rate of model and measurement.

3.2.2 WFE rail on WFE slab

Different models have been proposed for modelling the structural vibrations in slabs, e.g. based on beam theory [43], based on FEM using shell elements [44] or 3D brick elements [45], or a combination of FE and boundary elements (BE) [46]. A model based on the WFEM has been presented in [40]. The models based on 3D FEM and WFEM can likely fulfil the requirement on a high upper frequency limit for simulating noise radiation. An additional benefit of the WFEM is the lower computational cost and the inherent infinite extent of the track. In the following, a new method is presented based on discretely coupling two WFE models, which has been described in the appended **Paper A** and validated in **Paper C**. A similar approach followed in [40] uses the WFE model only for the slab and the layers below, but couples the slab to a beam model for the rail. The new modelling approach is summarised here.

In this method, the response of the free rail is evaluated using the WFE method. The response of the slab and the rest of the support layers is likewise evaluated using the WFE method. A section of the ground is included as a solid material, whose underside is fixed in space using Dirichlet boundary conditions. A principal sketch of the setup is shown in Figure 3.10. Notice the connection of the rail to the slab in three nodes across the rail foot. It is not necessary to use an equal spacing d_s of the rail seats in longitudinal direction [36].

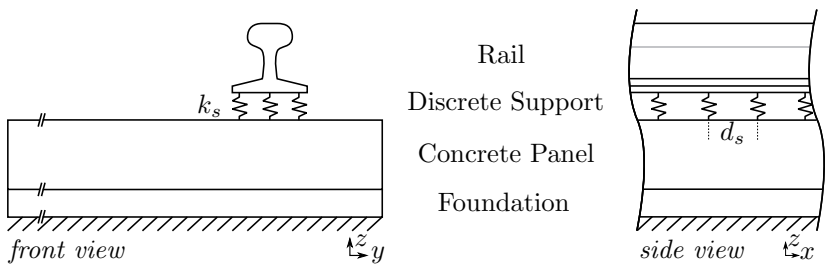

Figure 3.10: Sketch describing the discrete coupling of a rail with a concrete panel resting on a foundation. The combined spring stiffness k_s represents the rail pad stiffness. The spacing between the supports d_s can be varied.

The developed method as been implemented in the in-house WFEM code. To validate the modelling approach, the Chinese CRTS III track has been modelled. **Paper C** describes the realisation of this model in more depth. Further, validation measurements were conducted on a full-scale slab track test rig in the State Key Laboratory of Traction Power, South West Jiaotong University, Chengdu, China. Figure 3.11 shows the setup of the nodes of the 2D FE mesh, applied to the Chinese CRTS III slab track system shown in Figure 3.3. After conducting a parameter study and applying a genetic algorithm to calibrate the model parameters, a good match for multiple transfer functions is achieved. One such match is presented in Figure 3.12.

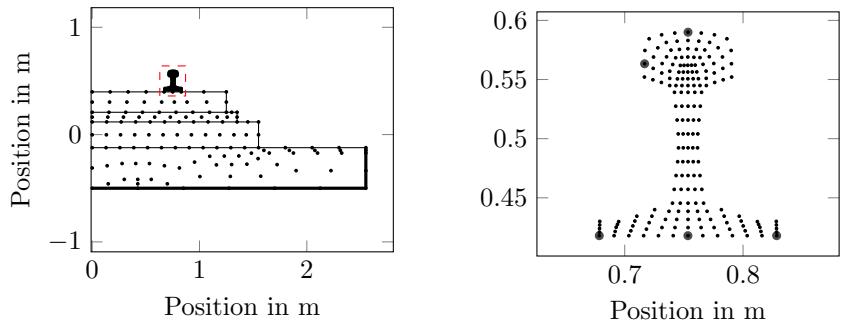

Figure 3.11: Nodes of the 2D finite element meshes of the CRTS III track system. (a) Track and rail. Note that only half of the symmetric mesh is shown. Top to bottom: Rail, slab, SCC layer, support layer, soil. Thick lines indicate a fixed boundary condition for the nodes on that boundary. The rail mesh is enlarged in (b). The nodes at which loads are applied are marked on the rail head. Likewise, nodes connected to the slab via springs are marked on the rail foot.

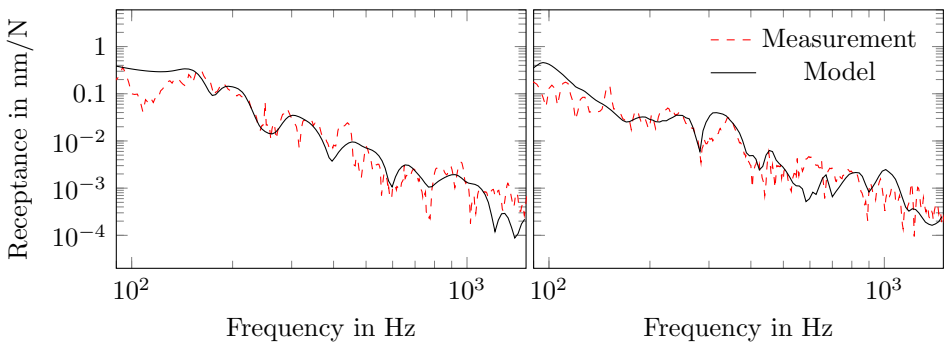

Figure 3.12: Comparison of the receptance magnitude for different excitation and measurement directions on the CRTS III track. The left and right figures show a vertical and a lateral receptance, respectively. The vertical receptance refers to a vertical excitation at the top node in Figure 3.11b, and the lateral receptance refers to an outward excitation at the node on the left side of the rail head. The response point is located on the slab, next to a rail seat.

3.3 Noise from slab tracks

Different methods for the sound radiation from rails and tracks are summarised in [15, Ch. 6.4]. One method combines the WFEM method presented above with the wavenumber boundary element method (WBEM). This was used by Nilsson et al. [37] for a free and an embedded rail and has since then been used in several other studies [24, 38, 39, 47]. In this work, the WBEM is used to calculate sound radiation from both the rail and the track.

In **Paper A**, the WFEM/WBEM approach is followed to calculate the sound radiation from the rail. However, instead of using only one BEM model, additionally, the vibrations from the concrete slab surface are included in the calculation. This enables the evaluation of the combined sound radiation from a slab track surface and the discretely supported rail. As described in Sec. 3.2.2, both the slab and the rail are modelled as WFE models. Therefore, the surface velocities of both bodies can be evaluated in wavenumber-frequency domain. The projection of these velocities on the surface normal direction produces the surface normal velocity which is then used as the input to the WBEM calculation.

In the paper, the transfer function for a unit force input at the top of rail to the total radiated sound power is evaluated. To identify parameters that influence the sound radiation from slab tracks, a parameter study is conducted focussing on (i) the rail pad stiffness, (ii) the thickness of the slab, and (iii) the type of support: continuous or discrete. It was found that similar to ballasted tracks, the rail pad stiffness has a major influence on the radiated sound power. By increasing this stiffness, a stronger coupling between the rail and its support is achieved. As pointed out by Thompson [15], this stronger coupling to the support decreases the vibration amplitude of the rail, increases the track decay rate, and ultimately leads to a lowered total radiated sound power. However, the rail pad stiffness is of major significance only for the discretely coupled rail. For a continuously supported rail, the total sound power is reduced and the rail pad stiffness is less influential.

In the WBEM, the slab and rail contributions are calculated separately. An evaluation of the contribution of the slab vibration to the total noise shows a minor significance of the noise produced by the slab surface. Nevertheless the slab can be expected to have a major influence on the directivity and the absorption characteristics of the radiated noise from the rails.

4 Railway wheel dynamics and noise modelling

This section addresses the modules related to the wheel in Figure 1.2. In Section 4.1, a description of commonly used models for the dynamics of railway wheels is given. Section 4.2 focusses on sound radiation from railway wheels.

4.1 Railway wheel dynamics

Analytical as well as numerical models have been applied to model the dynamic wheel response. In [48], the modes of vibration of a railway wheel are categorised like those of a flat circular plate. Consequently, the modes are described by their number of nodal diameters n and nodal circles m. This can be applied both to out-of-plane modes, also called axial modes, and in-plane modes, which could be either radial or circumferential modes. In this work the common notation to describe modes (n, m, a/r/c) is adopted with a, r and c for axial, radial and circumferential modes, respectively.

For numerical models, it is common to utilise the axi-symmetry of the structure. Thus, the size of the numerical problem can be drastically reduced by simplifying the geometry to its planar representation. Thompson [48] introduces a modelling approach based on the finite element method using axi-symmetric shell elements. In **Paper B**, an alternative modelling approach is applied to the case of a railway wheel, building on literature using the WFE method for curved structures for car tyres [49, 50]. Conceptually, here the wheel is considered an infinite waveguide with propagating waves around its axis of rotation. In contrast to straight waveguides, in which modes occur on a continuous wavenumber spectrum, here modes only occur at integer wavenumbers, due to the necessary continuity around the wheel.

Figure 4.1 presents the mesh of the cross-section of a railway wheel of type BA093 as e.g. used in the noise measurement car (Schallmesswagen, SMW) of DB Systemtechnik, described by Pieringer in [51]. The axle, indicated by the grey rectangle, is modelled as a rigid body. This approach was previously used by Thompson et al. [52], as it is pointed out in [48] that mainly the wheel modes of order $n = 0$ and $n = 1$ couple to the bending, extension and torsional modes of the axle. As, according to [52], these are not the main contributors to rolling noise, the dynamic properties of the axle can be ignored here.

The dynamic response of the wheel was evaluated using the WFE method for curved structures. The dispersion relation is shown in Figure 4.2. The dynamic response of the wheel at the contact point with the rail is described by its point mobilities, which are evaluated via modal superposition. The point mobility is the velocity response of the structure at a certain position, normalised by the corresponding harmonic excitation in the same position. Four modes are visualised in Figure 4.3.

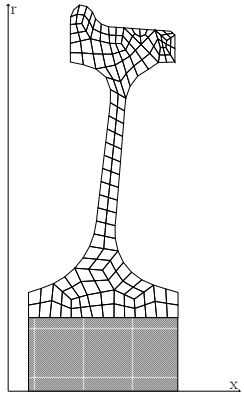

Figure 4.1: Finite element mesh of a railway wheel of the type BA093.

4.2 Noise from railway wheels

One convenient way to calculate the outward sound radiation in an unbounded domain is the Boundary Element Method (BEM). It is possible to formulate the method in cylindrical coordinates, see e.g. [53, 54]. There, the sound radiation is calculated using a Fourier series (FBEM), in which each element represents one order of the series. This method is used in Thompson et al. [52], where an engineering model for the sound radiated by railway wheels was developed. There, a key observation was that the radiation efficiency from lower order modes follows a power rule. In **Paper B**, this effect was reproduced using the in-house implementation of the FBEM. The connection to the power rule is visible for the radiation from the SMW wheel shown in Figure 4.1.

Figure 4.4 shows the radiation ratio for different numbers of nodal diameters and an axial excitation at the contact point. It is visible that the radiation ratio of each order n first follows a slope that is proportional to a f^{2n+2} and then tends towards unity for high frequencies. This is in line with [52] and further described in [15, Ch. 6.3].

The engineering models in [52] were developed for a wheel in free space. However, with the slab track surface in close proximity to the wheel, this assumption needs to be re-evaluated. In **Paper B**, a half-space formulation of the Green's functions is used in the BEM to account for ground reflection from an acoustically hard ground, i.e. a reflection factor $R = 1$. The acoustically hard ground could, for example, be a slab track surface or the street surface in an embedded rail tram system.

The radiation ratio of the wheel above an acoustically hard ground was evaluated using the developed model. Figure 4.5 shows the resulting radiation ratio. It was found that the presence of the track surface has the largest effect at low frequencies, up to about 200 Hz, leading to an increase of about 3 dB. Yet, the radiation ratio of the wheel is comparatively low in that frequency range. While it can be concluded that the slab track surface does not have a large impact on the radiation ratio, there can be a considerable influence on the directivity.

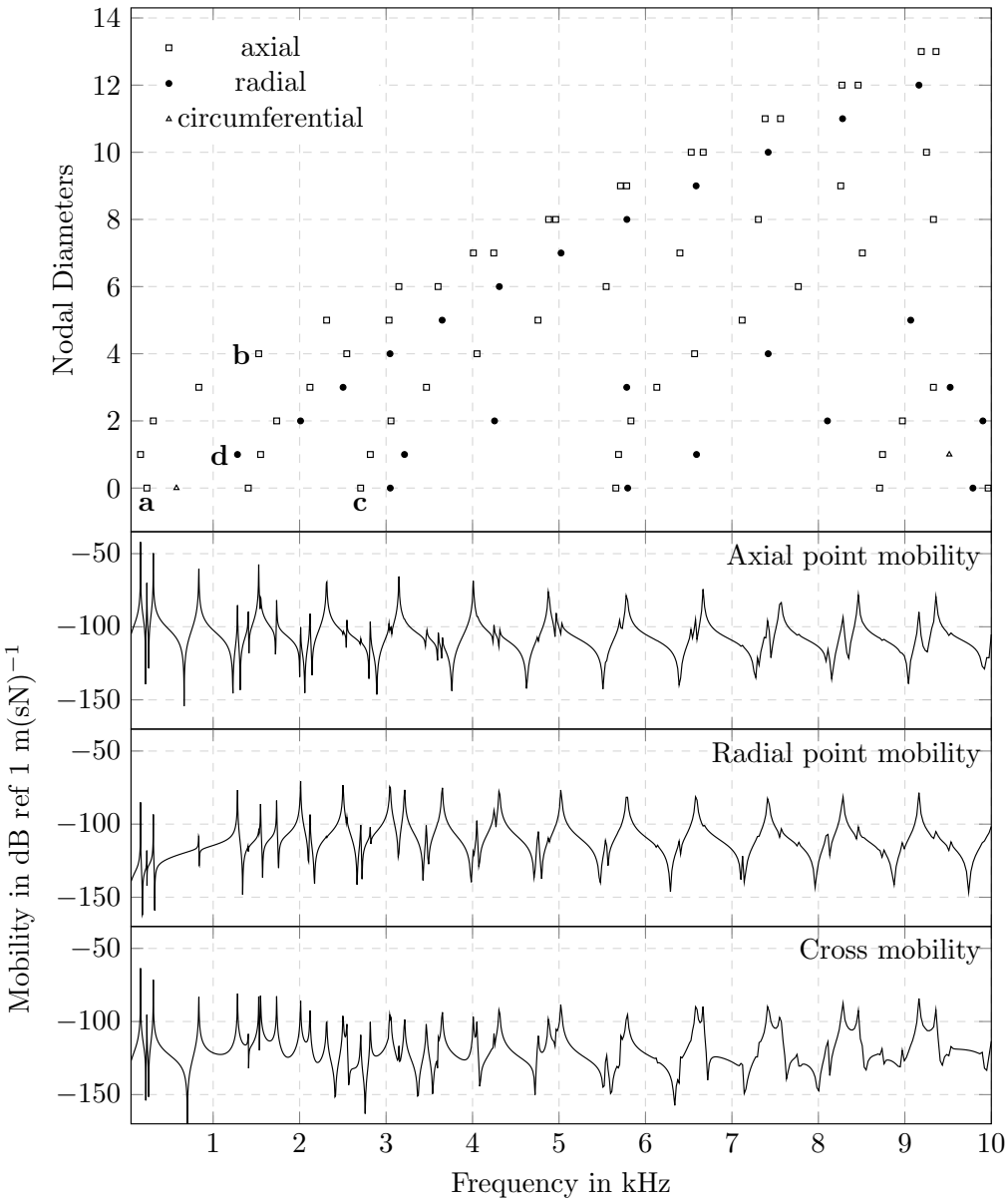

Figure 4.2: Top: Dispersion relation for the SMW wheel. Marked modes are **a**(0,0,a), **b**(4,0,a), **c**(0,2,a) and **d**(1,0,r). The lower figures show the axial, radial and axial/radial mobility at the contact point, centred on the running surface of the wheel.

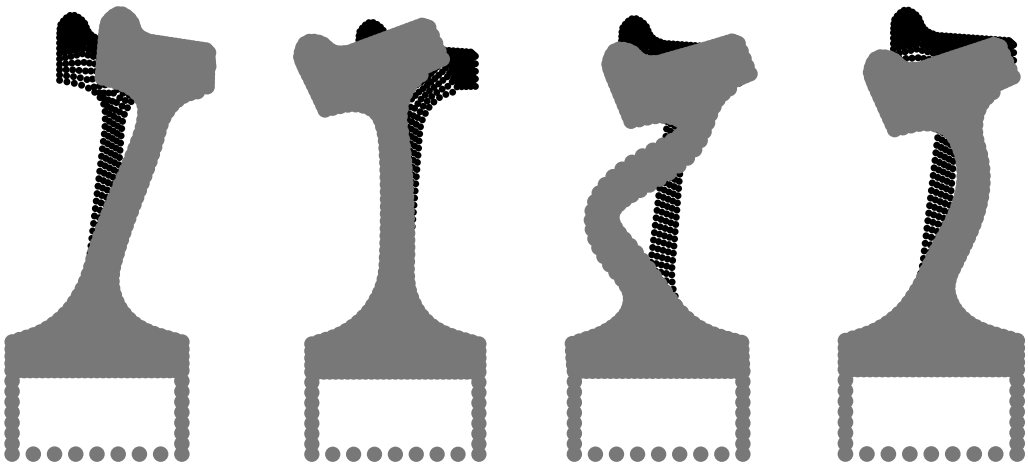

(a) (0,0,a) (b) (4,0,a) (c) (0,2,a) (d) (1,0,r))

Figure 4.3: Cross-sectional modal deflection shapes for the modes (a)-(d) indicated in Figure 4.2.

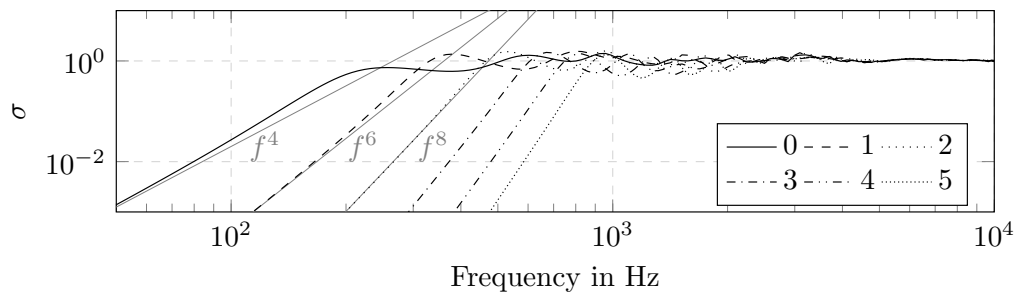

Figure 4.4: Radiation ratio σ of the wheel for different numbers of nodal diameters and an axial excitation at the contact point. The slopes of functions proportional to f^4, f^6 and f^8 are included as a reference.

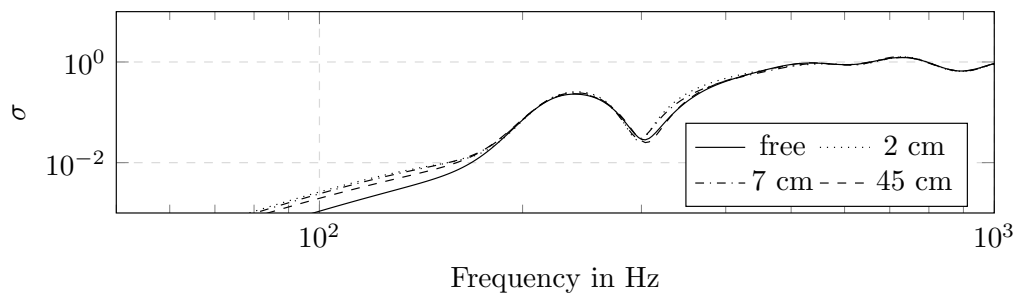

Figure 4.5: Radiation ratio for different heights of the wheel above the reflective surface.

5 Summary of appended papers

Paper A: The Influence of Track Parameters on the Sound Radiation from Slab Tracks

A frequency-wavenumber domain model for the dynamic response of slab tracks is developed including the discrete coupling of rail and slab. The surface velocities are used as the input to a wavenumber domain boundary element model. This enables the evaluation of the transfer function for a unit force input at the top of rail to the total radiated sound power. A parameter study is conducted focussing on (i) the rail pad stiffness, (ii) the thickness of the slab and (iii) the type of support: continuous or discrete. Comparable to ballasted tracks, an increasing rail pad stiffness is found to decrease the total radiated sound power. The rail pad stiffness is of major significance especially for the discretely coupled rail. For a continuously supported rail, the total sound power is reduced and the rail pad stiffness is less influential. The slab and rail contributions are calculated separately. An evaluation of the contribution of the slab vibration to the total noise shows a minor significance of the noise produced by the slab surface.

Paper B: Sound Radiation from Railway Wheels including Ground Reflections: A half-space formulation for the Fourier Boundary Element Method

This paper develops a method to evaluate the sound radiation from axi-symmetric bodies based on the curved Waveguide Finite Element and Fourier series Boundary Element Method. A half-space formulation of the Green's functions is applied in the Boundary Element Method to account for ground reflection from an acoustically hard ground. The acoustically hard ground could for example be a slab track surface or the street surface in an embedded rail tram system. The developed method is compared to analytical models as well as noise measurements of a vibrating steel disk. Using this method, the influence of the reflective plane on the radiation efficiency of railway wheels is researched. It is found that for the researched railway wheel, there is no major influence of the track surface on the radiation efficiency.

Paper C: Calibration and validation of two models for the dynamic response of slab track using data from a full-scale test rig

The calibration and validation of track dynamics simulation models is the focus in this paper. Impact hammer measurements were conducted on a full-scale slab track test rig in the State Key Laboratory of Traction Power, South West Jiaotong University, Chengdu, P.R. China. Then, both a finite and a waveguide finite element model are developed to represent a section of this track. The finite element model is three-dimensional where the rails are modelled as Rayleigh–Timoshenko beams and the concrete slab and support layer are modelled using linear plate elements. In the waveguide finite element model, a constant cross-section is assumed for the rail and the track, with the assumption of exponentially decaying, propagating waves along the track. The measurements are used to calculate the transfer functions between excitations on the rail and displacements on the slab and substructure. These receptances are then compared to the modelled version. A two step procedure is applied to calibrate the models, including (i) a parametric study

and (ii) a genetic algorithm. Finally, transfer functions from both calibrated models are compared to the measurements. A satisfactory agreement is found between the measured and calculated transfer functions, both for those TFs included in the calibration as well as others which were not included in the parameter matching. This implies that both models can successfully represent the dynamic properties of the test rig and can be considered as validated.

6 Conclusions

In this work, a numerical method for predicting vibrations in slab tracks has been developed, implemented and tested. The modelling approach is based on calculating frequency response functions separately in the rail and the rest of the superstructure in wavenumber-frequency domain, and then coupling the two systems in the positions of several rail seats in spatial-frequency domain. The developed method and implementation has been tested by comparison to measurements conducted on a full-scale slab track test rig, in which a good agreement was found.

Furthermore, the wavenumber boundary element method has been implemented to calculate the sound radiation from the vibrating structure. A simple slab track model has then been used to study the effect of track parameters such as the rail pad stiffness and the type of rail support (discrete/continuous). It was found that comparable to ballasted tracks, there is a large dependency of the radiated sound power to the rail pad stiffness, where an increased rail pad stiffness leads to a decreased radiated sound power. The contributions of the slab vibration to the total sound power was found low although relevant at low frequencies and for high rail pad stiffnesses.

Finally, a method for predicting the sound radiation from railway wheels over an acoustically hard reflective surface was developed, implemented and tested based on the axisymmetric Waveguide Finite Element method, and the Fourier series Wavenumber Boundary Element method combined with a half-space Green's functions approach. The implementation was tested against laboratory measurements and analytical models. A typical railway wheel geometry was modelled using this implementation. No significant change in the radiation efficiency of the wheel was found due to the presence of the surface. Note that this does not describe the influence of the reflecting surface on the directivity of the radiation but solely points at the fact that the total radiated sound power is not significantly affected by the slab surface.

7 Future Work

The components relevant to slab track will be integrated into one simulation tool according to the scheme presented in Figure 1.2. Specifically, a time-domain evaluation of the contact problem as presented by Pieringer [10, 55] will be used to generate realistic time-histories of wheel-rail interaction forces. A combination of the WFE and WBE method has been implemented in this work, tested and used to evaluate the transfer function from force input on the track to sound pressure level on the track-side. Combining this with the information of the time-history of the interaction forces will allow the modelling of track side noise levels during wheel pass-bys.

Further, a model for the vibration and radiation from ballasted track will be developed based on a similar approach as the model for slab track presented here. Then, a comparison of the radiation from ballasted and slab tracks will be conducted. The influence of the input parameters to the model will be researched. A validation of the model can be achieved by lab experiments and/or pass-by measurements on a real track.

Finally, the model will be applied to investigate two abatement measures for high noise levels. The first one, absorption on the track, provides a low profile solution that can potentially be retrofitted on existing tracks. A way to realise this is the introduction of an impedance plane in the developed Boundary Element model as described by Ochmann and Brick [56]. The second step is to investigate low-height barriers close to the track with regard to their acoustic performance, which can e.g. be achieved by introducing their geometry in the Boundary Element formulation.

References

[1] European Commission. Statistical Pocketbook 2019: EU transport. 2019.

[2] The European Commission. White Paper: Roadmap to a Single European Transport Area - Towards a competitive and resource efficient transport system. Retrieved May 17, 2020, from `https://eur-lex.europa.eu/legal-content/EN/TXT/PDF/?uri=CELEX:52011DC0144`. 2011.

[3] International Union of Railways (UIC). High speed Rail. Brochure. Retrieved May 8, 2020, from https://uic.org/passenger/highspeed. 2018.

[4] International Union of Railways (UIC). High Speed Traffic in the World. Document. Retrieved May 8, 2020, from https://uic.org/passenger/highspeed. 2020.

[5] C. Esveld. Modern Railway Track. Ed. by D. Zwarthoed-van Nieuwenhuizen. 2nd ed. Zaltbommel, The Netherlands: MRT-Productions. 2001.

[6] P. E. Gautier. Slab track: Review of existing systems and optimization potentials including very high speed. *Construction and Building Materials*. **92** (Feb. 2015), 9–15.

[7] ISO. *Acoustics — Description, measurement and assessment of environmental noise — Part 1: Basic quantities and assessment procedures*. Standard ISO 1996-1:2016(E). Geneva, Switzerland: International Organization for Standardization, 2016.

[8] International Union of Railways (UIC). UIC NETWORK NOISE & VIBRATION. Brochure. Retrieved May 8, 2020 from https://uic.org/IMG/pdf/uic_noise_flyer_2019.pdf. 2019.

[9] D. THOMPSON and C. JONES. A review of the modelling of wheel/rail noise generation. *Journal of Sound and Vibration*. **231**(3) (2000), 519–536.

[10] A. Pieringer, W. Kropp and D. J. Thompson. Investigation of the dynamic contact filter effect in vertical wheel/rail interaction using a 2D and a 3D non-Hertzian contact model. *Wear*. **271**(1-2) (2011), 328–338.

[11] D. Thompson. On the relationship between wheel and rail surface roughness and rolling noise. *Journal of Sound and Vibration*. **193**(1) (1996), 149–160.

[12] P. J. Remington. Wheel/rail noise-Part IV: Rolling noise. *Journal of Sound and Vibration*. (1976), 419–436.

[13] D. J. Thompson. Wheel-rail Noise Generation, Part I: Introduction And Interaction Model. *Journal of Sound and Vibration*. **161**(3) (Mar. 1993), 387–400.

[14] J. Nielsen and A. Igeland. Vertical dynamic interaction between train and track influence of wheel and track imperfections. *Journal of Sound and Vibration*. **187**(5) (1995), 825–839.

[15] D. Thompson. Railway Noise and Vibration. 1st ed. Oxford, United Kingdom: Elsevier Science. 2008.

[16] T. Kitawaga, K. Nagakura and T. Kurita. Contribution of Rolling Noise and Aerodynamic Noise to the Total Noise Generated from the Lower Part of Shinkansen Cars Running at High-speed. *Quarterly Report of RTRI.* **54**(4) (2013), 214–221.

[17] P. J. Remington. Wheel/rail rolling noise: What do we know? What don't we know? Where do we go from here? *Journal of Sound and Vibration.* **120**(2) (1988), 203–226.

[18] M. L. Munjal and M. Heckl. Vibrations of a periodic rail-sleeper system excited by an oscillating stationary transverse force. *Journal of Sound and Vibration.* **81**(4) (1982), 491–500.

[19] M. L. Munjal and M. Heckl. Some mechanisms of excitation of a railway wheel. *Journal of Sound and Vibration.* **81**(4) (1982), 477–489.

[20] R. J. Diehl, R. Nowack and G. Hölzl. Solutions for acoustical problems with ballastless track. *Journal of Sound and Vibration.* **231**(3) (2000), 899–906.

[21] S. Van Lier. Vibro-acoustic modelling of slab track with embedded rails. *Journal of Sound and Vibration.* **231**(3) (2000), 805–817.

[22] U. Moehler et al. The new German prediction model for railway noise "Schall 03 2006" -Potentials of the new calculation method for noise mitigation of planned rail traffic. *Notes on Numerical Fluid Mechanics and Multidisciplinary Design.* Vol. 99. (2008), 186–192.

[23] F. Poisson. "Railway Noise Generated by High-Speed Trains". *Notes on Numerical Fluid Mechanics and Multidisciplinary Design.* Vol. 126. Springer Verlag. 2015, pp. 457–480.

[24] X. Zhang et al. An engineering model for the prediction of the sound radiation from a railway track. *Journal of Sound and Vibration.* (Aug. 2019), 114921.

[25] E. Aggestam. Simulation of vertical dynamic interaction between railway vehicle and slab track. Licentiate Thesis. Gothenburg, Sweden: Chalmers University of Technology, 2018.

[26] Rail.One. RHEDA 2000® Ballastless Track System. Brochure. Retrieved on May 8, 2020, from https://www.railone.com/fileadmin/daten/05-presse-medien/downloads/broschueren/en/Rheda2000_EN_2011_ebook.pdf. Neumarkt, Germany, 2011.

[27] Rail.One. Getrac® Ballastless Track System. Brochure. Retrieved on May 8, 2020, from https://www.railone.com/fileadmin/daten/05-presse-medien/downloads/broschueren/en/Getrac_EN2012_ebook.pdf. Neumarkt, Germany, 2012.

[28] M. Wang et al. Experimental study on dynamic performance of typical nonballasted track systems using a full-scale test rig. *Proceedings of the Institution of Mechanical Engineers, Part F: Journal of Rail and Rapid Transit.* **231**(4) (2017), 470–481.

[29] Edilon)(sedra. One system crossing the boundaries. Brochure. Retrieved on May 8, 2020, from https://www.edilonsedra.com/ts-download/edilonsedra-corkelast-ers-embedded-rail-system-for-optimum-integration-into-tunnel-station-and-bridge-structures. Haarlem, The Netherlands, 2015.

[30] I. Avramovic, ÖBB-Porr. (Private communication). May 2020.

[31] D. J. Thompson, B. Hemsworth and N. Vincent. Experimental validation of the twins prediction program for rolling noise, part 1: Description of the model and method. *Journal of Sound and Vibration.* **193**(1) (1996), 123–135.

[32] D. J. Thompson. Wheel-rail Noise Generation, Part III: Rail Vibration. *Journal of Sound and Vibration.* **161**(3) (Mar. 1993), 421–446.

[33] L. Gavrić. Computation of propagative waves in free rail using a finite element technique. *Journal of Sound and Vibration.* **185**(3) (1995), 531–543.

[34] M. A. Heckl. Coupled waves on a periodically supported Timoshenko beam. *Journal of Sound and Vibration.* (2002), 849–882.

[35] X. Sheng, C. Jones and D. J. Thompson. Responses of infinite periodic structures to moving or stationary harmonic loads. *Journal of Sound and Vibration.* **282**(1-2) (2005), 125–149.

[36] X. Zhang et al. A model of a discretely supported railway track based on a 2.5D finite element approach. *Journal of Sound and Vibration.* **438** (2018), 153–174.

[37] C. M. Nilsson et al. A waveguide finite element and boundary element approach to calculating the sound radiated by railway and tram rails. *Journal of Sound and Vibration.* **321**(3-5) (2009), 813–836.

[38] X. Zhang, G. Squicciarini and D. J. Thompson. Sound radiation of a railway rail in close proximity to the ground. *Journal of Sound and Vibration.* **362** (2016), 111–124.

[39] X. Sheng, T. Zhong and Y. Li. Vibration and sound radiation of slab high-speed railway tracks subject to a moving harmonic load. *Journal of Sound and Vibration.* **395** (2017), 160–186.

[40] X. Zhang et al. The noise radiated by ballasted and slab tracks. *Applied Acoustics.* **151** (2019), 193–205.

[41] D. Thompson et al. Assessment of measurement-based methods for separating wheel and track contributions to railway rolling noise. *Applied Acoustics.* **140**(May) (2018), 48–62.

[42] C. Jones, D. Thompson and R. Diehl. The use of decay rates to analyse the performance of railway track in rolling noise generation. *Journal of Sound and Vibration.* **293**(3-5) (June 2006), 485–495.

[43] X. Yang et al. Effect of track irregularity on the dynamic response of a slab track under a high-speed train based on the composite track element method. *Applied Acoustics*. **99** (2015), 72–84.

[44] E. Aggestam, J. C. Nielsen and R. Bolmsvik. Simulation of vertical dynamic vehicle–track interaction using a two-dimensional slab track model. *Vehicle System Dynamics*. **56**(11) (2018), 1633–1657.

[45] E. Aggestam, J. C. O. Nielsen and N. Sved. Simulation of Vertical Dynamic Vehicle–Track Interaction – Comparison of Two- and Three-Dimensional Models. *Advances in Dynamics of Vehicles on Roads and Tracks*. Ed. by M. Klomp et al. Cham: Springer International Publishing. (2020), 415–422.

[46] P. Galvín, A. Romero and J. Domínguez. Vibrations induced by HST passage on ballast and non-ballast tracks. *Soil Dynamics and Earthquake Engineering*. **30**(9) (2010), 862–873.

[47] X. Zhang et al. The effects of ballast on the sound radiation from railway track. *Journal of Sound and Vibration*. **399** (July 2017), 137–150.

[48] D. J. Thompson. Wheel-rail Noise Generation, part II: Wheel Vibration. *Journal of Sound and Vibration*. **161**(3) (Mar. 1993), 401–419.

[49] S. Finnveden and M. Fraggstedt. Waveguide finite elements for curved structures. *Journal of Sound and Vibration*. **312**(4-5) (2008), 644–671.

[50] C. Hoever. The simulation of car and truck tyre vibrations, rolling resistance and rolling noise. PhD Thesis. Chalmers University of Technology, 2014, pp. 1–118.

[51] A. Pieringer. Acoustic monitoring of rail faults in the German railway network. *13th International Workshop on Railway Noise*. Ghent; (2019).

[52] D. J. Thompson and C. Jones. Sound radiation from a vibrating railway wheel. *Journal of Sound and Vibration*. **253**(2) (2002), 401–419.

[53] A. F. Seybert et al. A special integral equation formulation for acoustic radiation and scattering for axisymmetric bodies and boundary conditions. *Journal of the Acoustical Society of America*. (1986), 1241–1247.

[54] A. H. W. M. Kuijpers, G. Verbeek and J. W. Verheij. An improved acoustic Fourier boundary element method formulation using fast Fourier transform integration. *The Journal of the Acoustical Society of America*. **102**(3) (1997), 1394–1401.

[55] A. Pieringer. Time-domain modelling of high-frequency wheel / rail interaction. Ph.D. Thesis. Chalmers University of Technology, 2011.

[56] M. Ochmann and H. Brick. "Acoustical Radiation and Scattering above an Impedance Plane". *Computational Acoustics of Noise Propagation in Fluids - Finite and Boundary Element Methods*. Berlin, Heidelberg: Springer Berlin Heidelberg. 2008, pp. 459–494.

Part II
Appended Papers A–C

Paper A

The Influence of Track Parameters on the Sound Radiation from Slab Tracks

The Influence of Track Parameters on the Sound Radiation from Slab Tracks

Jannik S. Theyssen, Astrid Pieringer, and Wolfgang Kropp

Chalmers University of Technology, Applied Acoustics, 412 96 Gothenburg, Sweden
jannik.theyssen@chalmers.se

Abstract. The influence of track parameters on the sound radiation has so far mainly been studied for ballasted tracks. The increasing usage of slab tracks in new railway lines worldwide makes a review of these parameters relevant. In this paper, the structural vibrations of rail and slab are evaluated based on two waveguide finite element models that are coupled in a finite number of positions. This discretely supported rail is compared to a rail on a continuous support. The sound radiation from rail and slab is evaluated based on a wavenumber boundary element method. The slab and rail contributions are evaluated separately. It is found that comparable to ballasted tracks, the rail pad stiffness has a large influence on the radiated sound power. For a continuously supported rail, the total sound power is reduced and the rail pad stiffness is less influential.

Keywords: Slab Track, Infinite Waveguide, Boundary Elements, Discrete Coupling, Sound Power, Rail Pad Stiffness

1 Introduction

Slab tracks are a common type of track in high-speed railway lines. With the increasing length of high-speed lines in the world, more residents close to these lines are affected by noise emissions related to these tracks. Multiple references describe increased noise levels of slab tracks compared to ballasted tracks. A simulation of both track types reported in [1] showed an increase of 1.5 to 3 dB(A) for the slab track. Poisson [2] describes an observed increase of 3 dB(A) at 25 m distance from the track based on a number of measurements of different trains at different speeds. Thompson [3] describes the strong effect of the rail pad stiffness on the radiated noise for ballasted tracks. An increased pad stiffness leads to a decreased noise radiation. This decrease is described to be due to the stronger coupling of the rail to the sleepers, leading to a higher track decay rate. Since slab tracks use a lower pad stiffness by design, a higher sound radiation due to the weaker coupling is expected. However, slab tracks give the opportunity for supporting the rail continuously, increasing the coupling. Slab tracks furthermore have a larger mass than a system with sleepers, decreasing the receptance under the rail pad. These effects are investigated in the following.

Different methods of calculating the radiated sound power from slab tracks have been proposed. In [1], the radiation from the rail is calculated using equivalent sources. The slab radiation is calculated for a continuously supported rail

using a Finite Element model. The sound radiation from the rails and slab is treated separately in [4] as well. Here, the rail radiation is evaluated in a 2.5D boundary element model. The slab is modelled as a baffled plate. In the following, an integrated method of calculating the combined receptance and radiated sound power from rail and slab is introduced based on waveguide finite elements for the structural vibrations and a wavenumber boundary element model for the radiation.

2 Methodology

In this section, the waveguide finite element (WFE) method is described. Then the discrete coupling of multiple WFE-models is introduced. Finally, the coupling to the acoustic domain using the wavenumber boundary element (WBE) method is summarized.

2.1 Waveguide Finite Element Method

The following is a summary of the method, a more extensive derivation can for example be found in [5]. In this work, this method is applied to the geometry of a rail as well as the superstructure of a slab track.

A structure that is sufficiently large in one dimension with a constant cross-section can be approximated as a waveguide. The WFE method uses the assumption of travelling waves along the waveguide to reduce the finite element problem to the cross-section A of the structure. A lies in the y, z-plane and is discretized using conventional 2-dimensional, nine-node, iso-parametric quadrilateral elements with quadratic polynomials as shape functions.

A stationary motion at circular frequency ω is assumed with the time dependency $\mathrm{e}^{j\omega t}$. A matrix equation for the relationship between the element nodal displacements u_i and the nodal forces f_i is derived for each element by applying Hamilton's principle. Assembling these matrices leads to the expression

$$\left[\mathbf{K}_2 \frac{\delta^2}{\delta x^2} + \mathbf{K}_1 \frac{\delta}{\delta x} + \mathbf{K}_0 - \omega^2 \mathbf{M}\right] \hat{\mathbf{U}} = \hat{\mathbf{F}} \tag{1}$$

with the stiffness matrices $\mathbf{K}_i$ and the mass matrix $\mathbf{M}$. Using the Fourier Transform, the displacements $\hat{\mathbf{U}}$ and forces $\hat{\mathbf{F}}$ in spatial domain are expressed in wavenumber domain $\tilde{\mathbf{U}}$

$$\left[\mathbf{K}_2(-j\kappa)^2 + \mathbf{K}_1(-j\kappa) + \mathbf{K}_0 - \omega^2 \mathbf{M}\right] \tilde{\mathbf{U}} = \tilde{\mathbf{F}} \tag{2}$$

Considering $\tilde{\mathbf{F}} = \overrightarrow{0}$ this represents a linear eigenvalue problem when specifying a wavenumber κ or a quadratic eigenvalue problem when prescribing a frequency ω. The solution of the quadratic eigenvalue problem produces n complex conjugate pairs of wavenumbers κ_n corresponding to propagating, decaying waves. The

right and left eigenvectors $\mathbf{U}_{nR}$ and $\mathbf{U}_{nL}$ are superposed to calculate the total response for a force input at one node and $x = 0$ for each frequency,

$$\hat{\mathbf{U}}_{\mathbf{0}} = \sum_n A_n \mathrm{e}^{-j\kappa_n x} \quad \text{for } x \geq 0 \tag{3}$$

with

$$A_n = j \frac{\tilde{\mathbf{U}}_{nL} \tilde{\mathbf{F}}_0}{\tilde{\mathbf{U}}_{nL} \mathbf{D}(\kappa_n) \tilde{\mathbf{U}}_{nR}} \tag{4}$$

and

$$\mathbf{D}(\kappa_n) = -2\kappa_n \mathbf{K}_2 - j\mathbf{K}_1. \tag{5}$$

Eq. 3 is expressed in wavenumber domain,

$$\tilde{\mathbf{U}}_0 = \sum_n A_n \tilde{\mathbf{U}}_{nR} \left(\frac{-1}{Im(\kappa_n) - j(\kappa + Re(\kappa_n))} + \frac{-1}{Im(\kappa_n) + j(\kappa - Re(\kappa_n))} \right) \tag{6}$$

with Re/Im denoting the real and imaginary part of the complex wavenumber.

2.2 Discrete Support

Two WFE models, the rail and the superstructure, can be discretely coupled at a finite number of locations x along the waveguide. The displacement at any point on the coupled rail u_i^r is, similar as described in [4], a superposition of the free WFE response due to the excitation force $\hat{F}_e$ and the response to the reaction forces $\hat{F}_j$ in the coupling points,

$$u_i^r = \alpha_{ie}^r \hat{F}_e - \sum_j \alpha_{ij}^r \hat{F}_j \tag{7}$$

where the transfer functions α_{i*} describe the free rail response at location x_i for an excitation at x_*. Likewise the displacement at any point of the track t is the result of the superposition of the reaction forces.

$$u_i^t = \sum_j \alpha_{ij}^t \hat{F}_j \tag{8}$$

The transfer functions α_{ij}^r and α_{ij}^t are evaluated for each WFE model, which in case of the track includes essential boundary conditions. At each of the n_c coupling locations along the waveguide, the structures are coupled in m degrees of freedom of the FE-mesh. The coupling condition is described by a receptance α^p. Here, this is achieved using linear springs. The vertical and lateral direction are considered uncoupled.

$$u_i^r - u_i^t = \alpha_i^p \hat{F}_i \tag{9}$$

Eq. 9 links Eq. 7 with Eq. 8. The $n_c \cdot m$ transfer functions α^* for each system are assembled to form a system of equations

$$\left(\boldsymbol{\alpha}^p + \boldsymbol{\alpha}^r + \boldsymbol{\alpha}^t\right) \hat{F} = \boldsymbol{\alpha}_e^r \hat{F}_e \tag{10}$$

which is solved for the vector of reaction forces $\hat{F}$. These are then reintroduced in Eq. 7 and Eq. 8 to calculate the receptance in spatial domain at any point on either of the structures. The reaction forces at the discrete coupling locations are expressed as a wavenumber spectrum at the origin x_0.

$$\tilde{F}_{m,0}(k) = \sum_{i=1}^{n_c} \hat{F}_{m,i} \, \mathrm{e}^{jkx_i} \tag{11}$$

This force spectrum is introduced as an excitation in Eq. 6 to calculate the receptance on each structure. For the rail, the excitation force is either included in the force spectrum, or Eq. 6 is used to calculate the free response as well as the response due to the reaction forces and their displacements are superposed.

2.3 Wavenumber Boundary Element Method

The wavenumber boundary element method is described in [5]. The wavenumber in air $k = \omega/c$ is divided into the in-plane component α and the component along the waveguide matching the wavenumber in the structure κ by

$$\alpha = \sqrt{k^2 - \kappa^2}. \tag{12}$$

The in-plane boundary element problem is solved for each κ based on the 2D Helmholtz equation [6]. The normal velocity $\tilde{v}_{ni}$ serves as the Neumann boundary condition

$$\tilde{v}_{ni} = j\omega \tilde{\mathbf{u}}_i \mathbf{n} \tag{13}$$

where the nodal displacement vector $\tilde{\mathbf{u}}_i$ is the direct result of Eq. 6 and $\mathbf{n}$ is the outward normal direction.

In the case of the discrete support, multiple radiating boundaries are included. Their geometries and nodal displacements are combined in one BE model. For the continuous support, the air gap between the rail and the slab does not exist and only one boundary needs to be considered. Ground reflection is included in the Green's function formulation [7]. An acoustically rigid ground is placed right below the model. The CHIEF method is used to prevent internal resonances. Having determined the pressure at the boundary, the radiated sound power P can be calculated by integrating the intensity over the surface. In the wavenumber domain this is a double integral over the wavenumber spectrum and the perimeter. Contributions from individual bodies to the total sound power can be calculated by integrating over their surfaces individually.

$$P = \frac{1}{2} Re \left(\int_{-k}^{k} \int_{\Gamma} \tilde{p}^*(\kappa) \tilde{v}_n(\kappa) \mathrm{d}\Gamma \mathrm{d}\kappa \right) \tag{14}$$

2.4 Model and Parameter Description

The cross-section of the geometry is shown in Fig. 1. For the discrete support, the slab and the rail are separate WFE-models which are connected via vertical

and lateral springs in three points over the width: in the centre and on either side of the rail foot. In longitudinal direction the supports are evenly spaced with the support distance $d_s = 0.65\,\mathrm{m}$.

The rail geometry is a standard UIC60 rail. The geometry of the track is a simple concrete slab that is resting on a soft ground with $100\,\mathrm{MN/m^3}$ foundation stiffness. The width of the concrete slab and ground is 2.4 m, with the rail positioned half the standard track gauge from the centre. The material properties for these structures are given in Table 1. For the continuous support, the Young's modulus of the rail pad is adjusted to the average pad stiffness of the discretely supported rail

$$E_p = \frac{k_p h}{d_s w \lambda} \text{ with } \lambda = \frac{1-\nu}{(1+\nu)(1-2\nu)} \tag{15}$$

with dynamic rail pad stiffness k_p, width of the rail foot w, the height of the rail pad h and the rail seat spacing d_s, to achieve a similar input receptance in vertical direction at the top of the rail. The factor λ compensates for the cross-contraction of the material. The stiffness is assumed linear with respect to displacement and constant over frequency.

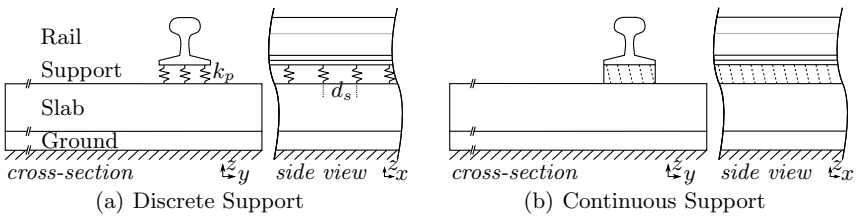

(a) Discrete Support (b) Continuous Support

Fig. 1. Model setup for the discretely and continuously supported rail. (a) The discrete support case. The lateral springs are not shown here. (b) The complete structure modelled as one waveguide.

	E (GPa)	ρ (kg/m^3)	ν (-)	η (-)
Rail	210	7850	0.3	0.01
Rail pad	E_p	1000	0.3	0.25
Slab	36	2400	0.2	0.1
Ground	0.0115	1	0.2	0.2

Table 1. Material properties of the components in the WFE model: Young's modulus E, density ρ, Poisson ratio ν and complex damping coefficient η. The ground density is chosen low to avoid internal resonances.

The researched parameters are the stiffness of the rail pad, the thickness of the slab and the type of support. The vertical rail pad stiffness takes the values 10, 20, 40, 80, 160 or 320 kN/mm. The lateral stiffness is set to 10% of these values. The slab thickness is 10 cm or 20 cm. It should be noted that some of these parameters can be considered unrealistic. The goal is solely to investigate their effect.

3 Results

In the following, the rail is excited using a unit force at the top of the rail, 3 mm off-centre towards the inside of the track. For the discrete support, the excitation is above a rail pad. The vertical and lateral direction are treated separately. The input and transfer receptance for both the continuous and the discretely supported rail are compared in Fig. 2. A good agreement is found below 1 kHz. The effect of the discrete support is visible for example at the pinned-pinned frequency around 950 Hz in vertical direction.

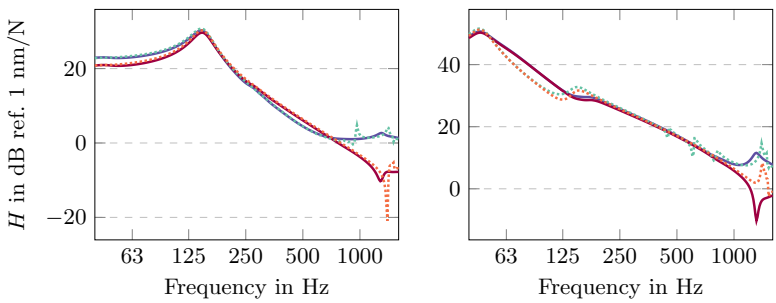

(a) Vertical Receptance (b) Lateral Receptance

Fig. 2. Receptance H of the continuous support (input ——, transfer ——) compared to discrete support (input ·····, transfer ·····). The transfer receptance describes the receptance to the top of the rail at mid-span, or the equivalent distance for the continuous support.

The radiated sound power for the different rail pad stiffnesses and both types of support is shown in Fig. 3. For both supports and both excitation directions it is found that the radiated sound power is in general lower for stiffer rail pads. This is in line with the prediction made in [3] for ballasted tracks. The structural resonance at which the slab and the rail vibrate vertically out of phase produces a peak in the spectrum. It is the largest peak in the spectrum for the continuously supported rail. The slope of the curves in 3(a) is about 20 dB/octave. Fig. 3(b) shows the same behaviour before reaching the structural resonance. Note that the rail pad stiffness does not seem to affect the radiated sound power much after this resonance occurs. For lateral excitation, the difference between the rail pad stiffnesses is less apparent for both supports. The main difference is around the first lateral bending resonance of the rail, below which a stiffer pad is beneficial.

The contribution of the slab and the rail to the total sound power is evaluated separately and presented in Fig. 4 for the discretely supported rail with vertical excitation. In general, the sound power spectrum is dominated by the radiation from the rail. However, a stronger coupling between the rail and the slab leads

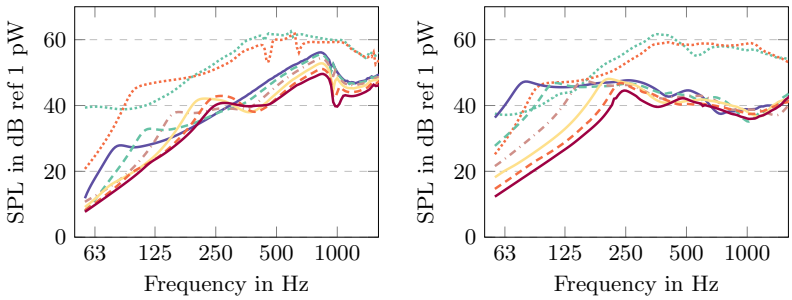

(a) Discrete Support (b) Continuous Support

Fig. 3. Radiation from a 20 cm slab at vertical excitation for different k_s: 10 kN/mm (——), 20 kN/mm (– – –), 40 kN/mm (–·–·–), 80 kN/mm (——), 160 kN/mm (– – –) and 320 kN/mm (——). Lateral excitation included for 20 kN/mm (·····) and 160 kN/mm (·····).

to a larger contribution of the slab, especially below the structural resonance. It was found that the contribution of the slab is negligible when exciting the rail in lateral direction.

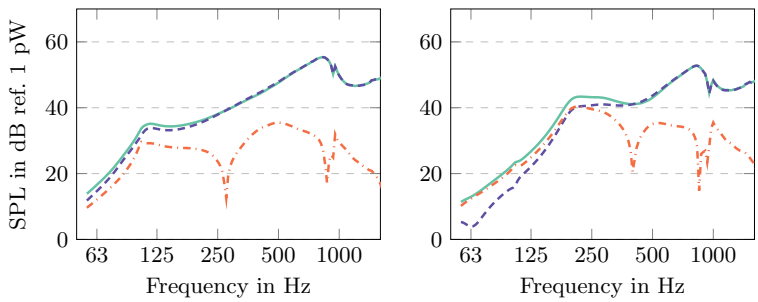

(a) $k_p = 20$ kN/mm (b) $k_p = 80$ kN/mm

Fig. 4. Contribution of rail (– – –) and slab (–·–·–) to the total radiated sound power (——) in case of a discretely supported rail on a 20 cm thick slab.

Different slab thicknesses are compared for the discretely supported rail with vertical excitation. Fig. 5 shows that the slab has minor influence on the radiated noise for soft pads. With increasing stiffness of the pad, the modal behaviour of the thinner slab becomes more influential.

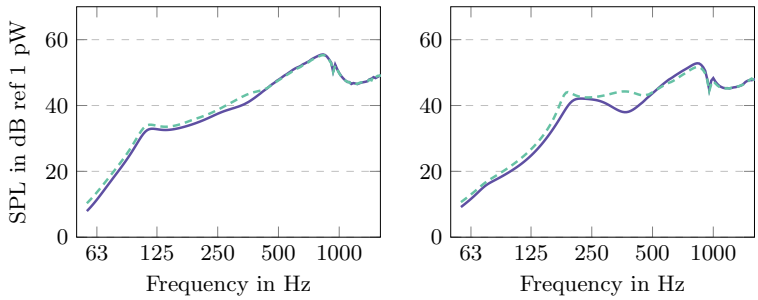

(a) $k_p = 20$ kN/mm (b) $k_p = 80$ kN/mm

Fig. 5. Comparing the radiated sound power of a discretely supported, vertically excited rail on a 10 cm (- - - -) and 20 cm slab (——).

4 Conclusion

A numerical method of calculating the structural response of slab tracks based on discretely coupled waveguides and a wavenumber BE method has been developed and implemented. The sound radiation from the combined rail and track vibration is modelled for a set of parameters. The results show a decrease in radiated sound power for higher rail pad stiffnesses. The rail is the main noise source. Its stronger coupling to the slab reduces the vibration levels on the rail. It leads to a relevant contribution of the slab to the total radiated noise for frequencies below the vertical structural resonance. Using a continuous support significantly decreases the total radiated sound power for higher frequencies.

Acknowledgements This work is part of the research activities in the Chalmers Competence Centre in Railway Mechanics *CHARMEC*. Especially the support from Trafikverket (the Swedish Transport Administration) is acknowledged.

References

1. S. Van Lier, "Vibro-acoustic modelling of slab track with embedded rails," J. Sound Vib., vol. 231, no. 3, pp. 805–817, 2000.
2. F. Poisson, "Railway noise generated by high-speed trains", Jens C.O. Nielsen et al. (eds.), Noise and Vibration Mitigation for Rail Transportation Systems, pp. 457–480, Berlin, Heidelberg, 2015. Springer Berlin Heidelberg.
3. D. J. Thompson, Railway Noise and Vibration, ISBN 9780080451473, 2009.
4. X. Zhang et al., "A model of a discretely supported railway track based on a 2.5D finite element approach," J. Sound Vib., vol. 438, pp. 153–174, 2018.
5. C. M. Nilsson, C. J. C. Jones, D. J. Thompson, and J. Ryue, "A waveguide finite element and boundary element approach to calculating the sound radiated by railway and tram rails," J. Sound Vib., vol. 321, no. 3–5, pp. 813–836, 2009.
6. T. W. Wu, "Boundary Element Acoustics", ISBN 9781853125706, 2000.
7. H. Brick and M. Ochmann, "A half-space BEM for the simulation of sound propagation above an impedance plane," J. Acoust. Soc. Am., 2008.

Paper B

Sound Radiation from Railway Wheels including Ground Reflections: A half-space formulation for the Fourier Boundary Element Method

Sound Radiation from Railway Wheels including Ground Reflections: A half-space formulation for the Fourier Boundary Element Method

François Fabre, Jannik S. Theyssen*, Astrid Pieringer, Wolfgang Kropp

Chalmers University of Technology, Division of Applied Acoustics, Department of Architecture and Civil Engineering, Sven Hultins Gata 8a, 41258 Gothenburg, Sweden

Abstract

Current models for the acoustic radiation from railway wheels assume free field radiation. However, slab tracks are increasingly used for new railway lines. The acoustically hard surface of those tracks makes a re-evaluation of the free field assumption relevant, as such a surface can affect the radiation efficiency of an acoustic radiator. The wheel as the acoustic radiator is most conveniently described in a cylindrical coordinate system, thus making use of its axisymmetry. While this is a viable solution for the structural vibrations, for instance by using the curved Waveguide Finite Element formulation, the axisymmetry breaks when including a reflective plane in the calculation of the acoustic radiation. A convenient method to include an infinitely large, reflective plane is by using half-space Green's functions in combination with the Boundary Element method. This method can be formulated in cylindrical coordinates using the Fourier series BEM (FBEM). However, the FBEM has not yet been combined with half-space Green's functions. This paper provides a half-space formulation for the FBEM, which enables e.g. the evaluation of sound radiation of railway wheels over reflective surfaces. Finally, it is shown that the assumption of free field radiation for railway wheels is valid, as there is no major contribution of the reflective plane to the radiation efficiency of the wheel. The developed method is validated against laboratory measurements as well as analytical models.

Keywords: Axisymmetry, Waveguide FEM, Green's functions, Radiation Efficiency, Railway Wheel, Slab Track

1. Introduction

A solid has axial symmetry when it can be created by rotating a planar geometry around an axis. The axisymmetry of objects is often used to down-

*Corresponding author
Email address: jannik.theyssen@chalmers.se (Jannik S. Theyssen)

scale numerical models, as simplifying the geometry to its planar representation considerably decreases the degrees of freedom in the system. The comparatively more elaborate element formulation of axisymmetric elements pays off in decreased calculation times. This downscaling is utilised in the following for calculating both structural vibrations as well as sound radiation.

Standard axisymmetric finite elements are well established, see e.g. [1], and part of most standard finite element packages [2, 3]. However, there is a large body of research using a curved waveguide finite element (WFE) formulation for axisymmetric bodies, especially in the field of predicting tyre vibrations and noise [4–7]. A summary of the curved WFE method can be found in [8]. In this paper, this WFE method is used for calculating the structural response of railway wheel, which is a novel application of this method.

At least three methods have been used to calculate the sound radiation from axisymmetric structures. Firstly, in [6, 7], the surface velocities are translated into a Cartesian coordinate system. Then, an implementation based on the standard 3D boundary element method (BEM) and half-space Green's functions developed in [9] is used. The inherent benefit of applying BEM on external problems, in which the structure radiates into the surrounding air, is that the Sommerfeld radiation condition [10] is fulfilled. Using BEM, the sound intensity is calculated on a half-sphere enclosing the wheel and the reflective ground plane. However, the computational cost is comparatively high due to the necessary meshing of the 3D surface of the vibrating object.

Secondly, in [5], a curved WFE model is used for calculating the structural vibrations. By introducing coupling elements between the structure and the surrounding air into the WFE model, the axisymmetry can be utilised even for the sound radiation. However, to fulfil the Sommerfeld radiation condition, a perfectly matched layer needs to be used, see e.g. [11].

The third approach, which this paper builds on, combines the benefits of an axisymmetric formulation and the BEM. Here, the acoustic variables of the problem are expanded as a Fourier series, which is why the method is often referred to as the Fourier series BEM (FBEM). The method is based on a paper by Seybert et al. [12], building on earlier research by Meyer et al. [13]. As will be shown in Section 2.2, the drawback of the FBEM formulation is that numerical difficulties occur in the evaluation of circumferential integrals, as these integrals can be singular and oscillatory [14]. The management of these singularities has been attempted using elliptic integrals by Soenarko et al. [15] and Juhl [16]. A major advancement of the method was proposed by Kuijpers et al. [14]. The fact that certain integrals can be calculated using the numerically efficient Fast Fourier Transform (FFT), instead of an integration scheme based on Gaussian quadrature, leads to a major reduction in the calculation time. Note that all methods that make use of the axisymmetry assume sound radiation into free space.

The sound radiation from railway wheels has been found to be one of the major contributors to overall railway noise and has been subject to extensive research [17–20]. In [19], the vibration behaviour of the railway wheel is described by its eigenmodes, which are characterised by their number of nodal diameters

and nodal circles. Physically, this is close to the idea of FBEM, such that each order in the Fourier expansion corresponds to a number of nodal diameters on the structure. At the same place it is pointed out that modes of order two and above have the largest contribution to rolling noise. An engineering model for the sound radiation has been developed by Thompson and Jones [20]. There, the axle geometry is neglected for vibration and radiation, using a fixed constraint at the wheel hub. According to [19], this produces adequate results starting from circumferential mode order 2. In that study, an axisymmetric BE formulation, corresponding to the third approach, is used to analyse the radiation ratio and directivity of wheels with different geometries. This radiation ratio is then evaluated for different modes and numbers of nodal diameters. In [21], this engineering model is compared to the 3D BEM implementation developed in [9] and a good agreement is found.

Reflecting on the presented methods, it is clear that so far there is only the possibility of including a reflective plane when disregarding the benefits of an axisymmetric formulation. This paper presents a method using of half-space Green's functions in the FBEM, which enable the calculation of the sound radiation of axisymmetric bodies in cylindrical coordinates over a reflective ground plane. Considerations regarding the accuracy of this method are presented. This paper then combines the WFE and FBE method for the application on a railway wheel. To the authors' knowledge, these methods have not been combined before and so a validation based on laboratory measurements and analytical models will be given.

2. Method

In the following, the waveguide finite element method as well as the boundary element method for axisymmetric bodies are summarised. A half-space formulation for solving the acoustic radiation problem in Fourier-expanded cylindrical coordinates is introduced. Considerations regarding its efficiency are presented and a validation of the method is shown.

2.1. WFE formulation

A summary of the method is stated here for convenience. A comprehensive overview can be found in [6, 8]. Describing the three-dimensional geometry by its constant cross-section enables the use of a two dimensional element formulation and drastically reduces the degrees of freedom in the system. The cross-section is defined in the (x, r)-plane with the radial direction r. The behaviour in the third dimension, which in case of an axisymmetric body refers to the circumferential direction θ, is described by propagating, decaying waves.

The displacement $\vec{u}$ at any location on the discretised body is described by

$$\vec{u}(x, r, \theta) = \underline{\mathbf{N}}(\xi, \eta)\vec{\mathrm{u}}(\theta) \tag{1}$$

with $\underline{\mathbf{N}}(\xi, \eta)$ a matrix whose entries are shape functions N_i and $\vec{\mathrm{u}}(\theta)$ containing all nodal displacements. For elastic materials without viscosity, Hamilton's

principle is written

$$\delta L = \delta(U - K + A) = 0 \tag{2}$$

with the Lagrangian L, the total strain energy U, the kinetic energy K and the potential energy of the loading A, where δ denotes "the first variation of". For a harmonic motion, Eq. (2) can be rewritten as

$$\delta L = \delta \int_V \left(\vec{\epsilon}^H \mathbf{D} \vec{\epsilon} - \rho\omega^2 \vec{u}^H \vec{u} - \vec{u}^H \vec{f} \right) dV \tag{3}$$

with the volume of the structure V, the material stiffness matrix $\mathbf{D}$ and density ρ. The variable ω represents the circular frequency and $\vec{f}$ is an external force density. The superscript ^{H} denotes the complex conjugate transpose.

The material strain vector $\vec{\epsilon}$ can be expressed on element e in terms of the nodal displacements $\vec{\mathrm{u}}_e$

$$\vec{\epsilon} = \left(\mathbf{E}_0 + \mathbf{E}_1 \frac{\partial}{\partial \theta} \right) \vec{\mathrm{u}}_e \tag{4}$$

as shown in Appendix A. Using this definition, Hamilton's principle can be reformulated to

$$\delta L = \int_0^{2\pi} \left(\sum_{m=0}^{1} \sum_{n=0}^{1} \frac{\partial^n \delta \vec{\mathrm{u}}^H}{\partial \theta^n} \mathbf{A}_{mn} \frac{\partial^m \vec{\mathrm{u}}}{\partial \theta^m} - \omega^2 \delta \vec{\mathrm{u}}^H \mathbf{M} \vec{\mathrm{u}} - \delta \vec{\mathrm{u}}^H \vec{\mathrm{f}} \right) d\theta \tag{5}$$

with the stiffness and mass matrix $\mathbf{A}_{mn}$ and $\mathbf{M}$, respectively, which are obtained by solving $\mathbf{a}_{e,mn}$, $\mathbf{m}_e$ and $\vec{\mathrm{f}}_e$ for each element and assembling to the global matrices

$$\mathbf{a}_{e,mn} = \int_{S_e} {\mathbf{E}_n}^T \mathbf{D} \mathbf{E}_m \; r dr dx \tag{6}$$

and

$$\mathbf{m}_e = \int_{S_e} \mathbf{N}^T \rho \mathbf{N} \; r dr dx \tag{7}$$

with S_e the surface of the element. The integral and the 'first variation of' vanishes after integration by parts of δL with respect to the θ-coordinate. The equation of motion is expressed in spatial and wavenumber domain as follows,

$$\left(\mathbf{K}_2 \frac{\partial^2}{\partial \theta^2} + \mathbf{K}_1 \frac{\partial}{\partial \theta} + \mathbf{K}_0 - \omega^2 \mathbf{M} \right) \vec{u}(\theta) = \vec{F}(\theta) \tag{8}$$

$$\left(\mathbf{K}_2 (-j\kappa)^2 + \mathbf{K}_1 (-j\kappa) + \mathbf{K}_0 - \omega^2 \mathbf{M} \right) \vec{u}(\kappa) = \vec{F}(\kappa) \tag{9}$$

with $\mathbf{K}_2 = -\mathbf{A}_{11}$, $\mathbf{K}_1 = \mathbf{A}_{01} - \mathbf{A}_{10}$ and $\mathbf{K}_0 = \mathbf{A}_{00}$.

Since only integer wavenumbers can propagate in circumferential direction, it is possible to prescribe the wavenumber κ and solve the resulting linear eigenvalue problem for ω. Physically, this corresponds to solving for the cross-sectional modes of the body for each circumferential order. Assuming the equation system is solved for N circumferential orders and S cross-sectional modes

are obtained for each order, then each mode at eigenfrequency $\omega_{0,n,s}$ is described by the corresponding eigenvector $\mathbf{U}_{n,s}$. The nodal displacement $\vec{u}$ for each circumferential order can be obtained by modal superposition [6, Ch. 4],

$$\vec{\mathrm{u}}(\theta,\omega) = \sum_{n=-N}^{N}\sum_{s=1}^{S} \frac{\mathbf{U}_{n,s}^{H} F_n(\omega)}{\left((1+j\eta(\omega))\omega_{n,s}^2 - \omega^2\right) m_{n,s}} \mathbf{U}_{n,s} \mathrm{e}^{-jn\theta} \tag{10}$$

with the loss factor η and the modal mass $m_{n,s}$

$$\delta_{s,t} m_{n,s} = \mathbf{U}_{n,s}^{H} \mathbf{M} \mathbf{U}_{n,t} \tag{11}$$

in which $\delta_{s,t}$ is the Kronecker delta.

The nodal displacements of the FE-nodes at the boundary of the structure can be projected on the boundary normal direction at each node. Multiplication with $j\omega$ produces the surface normal velocity which serves as the input to the boundary element calculation.

2.2. FBEM Formulation

The Kirchhoff-Helmholtz integral equation describes the relation of the pressure amplitude on a boundary to the pressure field in a surrounding fluid. It is the basis for the Boundary Element Method (BEM) and is expressed as

$$c(\vec{r})p(\vec{r}) = \int_S \Big(G(\vec{r};\vec{r}_0)\partial_n p(\vec{r}_0) - \partial_n G(\vec{r};\vec{r}_0) p(\vec{r}_0) \Big) dS_0 \tag{12}$$

$$= -\int_S \Big(j\rho\omega\ G(\vec{r};\vec{r}_0) v_n(\vec{r}_0) + \partial_n G(\vec{r};\vec{r}_0) p(\vec{r}_0) \Big) dS_0 \tag{13}$$

with the Green's function of the considered problem $G(\vec{r};\vec{r}_0)$, the pressure $p(\vec{r}_0)$ and surface normal velocity $v_n(\vec{r}_0)$ at a source point P_S on the boundary S, the density of the fluid ρ. The symbol ∂_n represents the derivative with respect to the outgoing normal direction on the fluid boundary $\vec{n}$. The coefficient $c(\vec{r})$ is 1/2 for an observer point P_{obs} on a smooth boundary, 1 in the fluid and 0 otherwise.

The Fourier Boundary Element Method (FBEM) utilises the axisymmetry of a body similar to WFEM, assuming that the sound field in circumferential direction can be described by a superposition of circumferential orders and therefore expanded in Fourier series. However, the reflection from a non axisymmetric plane is not easily described in this cylindrical coordinate system. The following sections present the necessary steps leading to the numerical implementation of half-space Green's functions in cylindrical coordinates described by the basis vectors $(\vec{x}_b, \vec{r}_b, \vec{\theta}_b)$.

2.2.1. FBEM formulation of the Physical Quantities

Consider the arbitrary axisymmetric body shown in Figure 1 radiating over an infinite plane with a given reflection coefficient R_p. In cylindrical coordinates

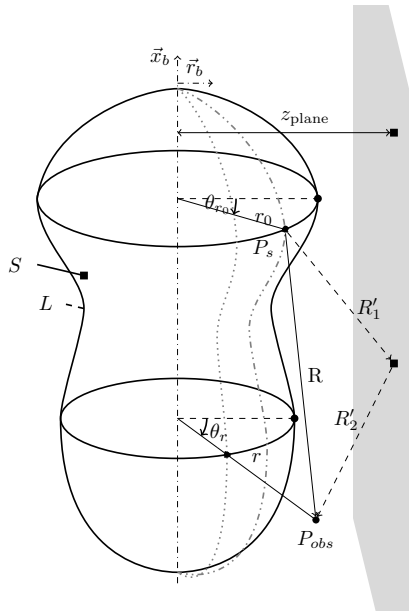

Figure 1: Axisymmetric body over a reflecting plane. R is the path length between the source position P_s and the observer position P_{obs}. Notice the total reflected path length is $R' = R'_1 + R'_2$. The surface S is created by rotating the generator L around the symmetry axis. The distance z_{plane} is measured normal to both the symmetry axis as well as the plane.

the half space Green's function G_{hs} is

$$G_{hs}(\vec{r},\vec{r}_0) = \underbrace{\frac{e^{-jkR}}{4\pi R}}_{G(\vec{r},\vec{r}_0)} + \underbrace{R_p \frac{e^{-jkR'}}{4\pi R'}}_{G_r(\vec{r},\vec{r}_0)} \tag{14}$$

with the first term corresponding to the free field Green's function and the second term describing the reflected field. The distances R and R' are written

$$\begin{aligned} R &= \|\vec{r} - \vec{r}_0\| \\ &= \left[(x-x_0)^2 + (r-r_0)^2 + 2rr_0(1-\cos(\theta_r - \theta_{r_0})\right]^{1/2} \end{aligned} \tag{15}$$

and

$$\begin{aligned} R' = \big[&(x-x_0)^2 + (r-r_0)^2 + 2rr_0(1+\cos(\theta_r + \theta_{r_0})) \\ &+4z_{\text{plane}}(r\cos(\theta_r) + r_0\cos(\theta_{r_0}) + z_{\text{plane}})\big]^{1/2} \end{aligned} \tag{16}$$

with the wavenumber k in circumferential direction.

The surface integral in Eq. (13) becomes $dS_0 = r_0\ dl_0 d\theta_{r_0}$, where dl_0 represents a line segment on the generator L. The necessary circumferential periodicity of all variables leads to the Fourier expansion

$$\begin{aligned} p(\vec{r}) &= \sum_{m=-\infty}^{\infty} P_m^*(x,r)e^{-jm\theta_r}, \\ p(\vec{r}_0) &= \sum_{m=-\infty}^{\infty} P_m(x_0,r_0)e^{-jm\theta_{r_0}}, \\ v_n(\vec{r}_0) &= \sum_{m=-\infty}^{\infty} V_m(x_0,r_0)e^{-jm\theta_{r_0}} \end{aligned} \tag{17}$$

with

$$\begin{aligned} P_m^*(x,r) &= \frac{1}{2\pi}\int_0^{2\pi} p(\vec{r})e^{jm\theta_r}d\theta_r, \\ P_m(x_0,r_0) &= \frac{1}{2\pi}\int_0^{2\pi} p(\vec{r}_0)e^{jm\theta_{r_0}}d\theta_{r_0}, \\ V_m(x_0,r_0) &= \frac{1}{2\pi}\int_0^{2\pi} v_n(\vec{r}_0)e^{jm\theta_{r_0}}d\theta_{r_0} \end{aligned} \tag{18}$$

in which the subscript * denotes that P_{obs} can be located both on the boundary and in the domain. The reflected field $G_r(\vec{r},\vec{r}_0)$ can not be directly expanded on $\theta_r - \theta_{r_0}$. A 2D Fourier Transform has to be applied on $G_r(\vec{r},\vec{r}_0)$ such that $G_{hs}(\vec{r},\vec{r}_0)$ writes

$$\begin{aligned} &G_{hs}(\vec{r},\vec{r}_0) \\ &= \frac{1}{2\pi}\left(\sum_p H_p e^{-jp(\theta_r-\theta_{r_0})} + \sum_{m,n} H_{r_{nm}} e^{-j(n\theta_r - m\theta_{r_0})}\right) \\ &= \frac{1}{2\pi}\sum_m \left(H_m e^{-jm\theta_r} + \sum_n H_{r_{nm}} e^{-jn\theta_r}\right) e^{jm\theta_{r_0}} \end{aligned} \tag{19}$$

with the coefficients H_m and $H_{r_{nm}}$, which are dependent on x, r, x_0 and r_0.

$$\begin{aligned} H_m &= \frac{1}{2\pi}\int_0^{2\pi} 2\pi\ G(\vec{r};\vec{r}_0)e^{jm(\theta_r-\theta_{r_0})}\ d(\theta_r-\theta_{r_0}) \\ H_{r_{nm}} &= \frac{1}{4\pi^2}\int_0^{2\pi}\int_0^{2\pi} 2\pi\ G_r(\vec{r},\vec{r}_0)e^{j(n\theta_r-m\theta r_0)}d\theta_r d\theta_{r_0}. \end{aligned} \tag{20}$$

Analogously,

$$\partial_n G_{hs}(\vec{r},\vec{r}_0) = \frac{1}{2\pi}\sum_m \left(H'_m e^{-jm\theta_r} + \sum_n H'_{r_{nm}} e^{-jn\theta_r}\right) e^{jm\theta_{r_0}} \tag{21}$$

where the coefficients H'_m and $H'_{r_{nm}}$ are the derivatives of H_m and $H_{r_{nm}}$ and dependent on x, r, x_0 and r_0,

$$\begin{aligned} H'_m &= \frac{1}{2\pi}\int_0^{2\pi} 2\pi\partial_n G(\vec{r};\vec{r}_0)e^{jm(\theta_r-\theta_{r_0})}\ d(\theta_r-\theta_{r_0}), \\ H'_{r_{nm}} &= \frac{1}{4\pi^2}\int_0^{2\pi}\int_0^{2\pi} 2\pi\partial_n G_r(\vec{r},\vec{r}_0)e^{j(n\theta_r-m\theta r_0)}d\theta_r d\theta_{r_0}. \end{aligned} \tag{22}$$

At this point, solving $p(x,r,\theta_r)$ is equivalent to solving $P^*_m(x,r)$ for every order m. This means that the initial 3D problem can be replaced by an infinite sum of 2D boundary problems if the the Fourier coefficient amplitudes are known.

2.2.2. Rewriting of the Kirchhoff-Helmholtz integral equation

For clarity, Fourier coefficients are now written without their spatial dependencies. Inserting Eq. (17), Eq. (19) and Eq. (21) in the integral formulation Eq. (13) leads to

$$\begin{aligned} & c(\vec{r})\sum_m P^*_m e^{-jm\theta_r} \\ &= -\frac{1}{2\pi}\iint_S \sum_{p,m}\Bigg[j\rho\omega\left(H_m e^{-jm\theta_r} + \sum_n H_{r_{nm}} e^{-jn\theta_r}\right)V_p \\ &\qquad + \left(H'_m e^{-jm\theta_r} + \sum_n H'_{r_{nm}} e^{-jn\theta_r}\right)P_p\Bigg] e^{-j(p-m)\theta_{r_0}} dS_0 \end{aligned} \tag{23}$$

where the orthogonality property between complex exponentials can be used. The integral over θ_{r_0} yields $m = n$, therefore

$$\begin{aligned} c(\vec{r}) \sum_m P_m^* e^{-jm\theta_r} &= -\int_L \sum_p \Bigg[j\rho\omega \left(H_p e^{-jp\theta_r} + \sum_n H_{r_{np}} e^{-jn\theta_r} \right) V_p \\ &\qquad + \left(H'_p e^{-jp\theta_r} + \sum_n H'_{r_{np}} e^{-jn\theta_r} \right) P_p \Bigg] r_0 dl_0 \\ &= -\int_L \sum_p \Bigg[\left(j\rho\omega H_p V_p + H'_p P_p \right) e^{-jp\theta_r} \\ &\qquad + \sum_n \left(j\rho\omega H_{r_{np}} V_p + H'_{r_{np}} P_p \right) e^{-jn\theta_r} \Bigg] r_0 dl_0 \end{aligned} \tag{24}$$

With that, the Fourier Boundary Integral equation can be expressed in a 3D half-space as

$$\boxed{c(\vec{r}) P_m^* = -\int_L \Bigg[\underbrace{j\rho\omega H_m V_m + H'_m P_m}_{\text{Direct field contribution}} + \underbrace{\sum_p \left(j\rho\omega H_{r_{mp}} V_p + H'_{r_{mp}} P_p \right)}_{\text{Reflected field contribution}} \Bigg] r_0 dl_0}. \tag{25}$$

which can be expressed as

$$\frac{1}{2} P_m = -\int_L \Bigg[j\rho\omega H_m V_m + H'_m P_m + \sum_p \left(j\rho\omega H_{r_{mp}} V_p + H'_{r_{mp}} P_p \right) \Bigg] r_0 dl_0 \tag{26}$$

if the observer point P_{obs} is on the boundary. The efficiency of the calculation of the H_m and H'_m is fundamental to this method and is discussed in the following subsection.

120 *2.2.3. Fast Fourier Transform computations*

H_m and H'_m can be evaluated numerically by means of Gaussian quadrature. However, since they need to be computed for each order, Kuijpers [14] proposed a method using the Fast Fourier Transform (FFT) algorithm, enabling the computation of all necessary orders at once. An expression for the minimum required number of Fourier samples n_{FFT} for the circumferential coordinate $\theta_r - \theta_{r_0}$ is proposed to evaluate the free field contribution $G(\vec{r}, \vec{r}_0)$ in the Green's function. A relative error not exceeding 10^{-3} is obtained in [14] with the expression

$$n_{FFT}(\vec{r}, \vec{r}_0) = 14 \left(c_s + \frac{c_o}{2\pi} \right)^{0.9} \tag{27}$$

with

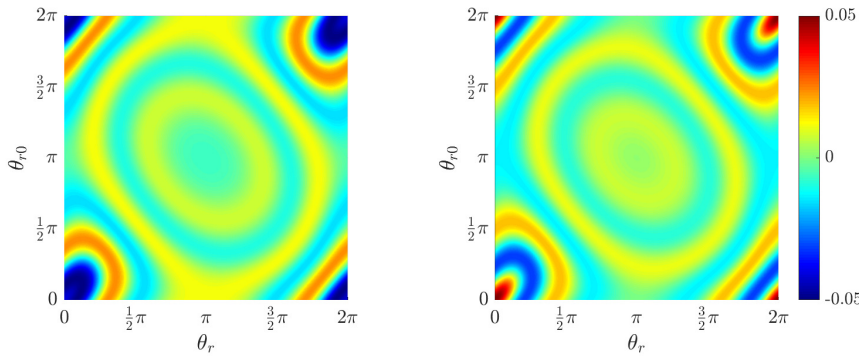

Figure 2: Example of the θ/θ_0-dependency of the Green's function for a given geometric situation. Real (right) and imaginary (left) part of the Green's function for $\vec{r} = (0\text{ m}, 3\text{ m}, [0, 2\pi])$, $\vec{r}_0 = (1\text{ m}, 2.5\text{ m}, [0, 2\pi])$, $z_{\text{plane}} = 3.1$ m at 100 Hz.

- $c_s = \dfrac{R_{max}}{R_{min}}$, a steepness criteria describing the slope of $G(\vec{r}, \vec{r}_0)$ near $\theta_r = \theta_{r_0}$,

- $c_o = k(R_{max} - R_{min})$, an oscillation criteria describing the impact of e^{-jkR} for high frequencies and/or large difference $(R_{max} - R_{min})$.

R_{max} and R_{min} are, respectively, the maximum and the minimum distance between $P_{obs}(\theta_r)$ and $P_s(\theta_{r_0})$ when considering every possible difference $(\theta_r - \theta_{r_0})$. Once $G(\vec{r}, \vec{r}_0)$ is known for a given couple source/observer points for n_{FFT} values, one can obtain H_m by selecting the coefficient at the sought position in the FFT. The same process is applied to $\partial_n G(\vec{r}, \vec{r}_0)$ to get H'_m.

This approach has been adapted for the calculation of the 2D Fourier Transform of $G_r(\vec{r}, \vec{r}_0)$. Since $G_r(\vec{r}, \vec{r}_0)$ is of the same form as $G(\vec{r}, \vec{r}_0)$, the same criteria can be used to evaluate the minimum number of Fourier Transform samples for each angle (n_{FFT_r} and $n_{FFT_{r_0}}$) for a given accuracy. The steepness and oscillation criteria for the Fourier Transform over θ_r are noted c_{s_r} and c_{o_r} while the one over θ_{r_0} are noted $c_{s_{r_0}}$ and $c_{o_{r_0}}$. Figure 2 shows the function $G_r(\vec{r}, \vec{r}_0)$ over both angular coordinates. It is apparent that e.g. for a transformation over θ_r, the slope of $G_r(\vec{r}, \vec{r}_0)$ varies depending on the value of θ_{r_0}. Thus, the criteria are functions of θ_{r_0} and write $c_{s_r}(\theta_{r_0}) = R'_{r_{max}}(\theta_{r_0})/R'_{r_{min}}(\theta_{r_0})$ and $c_{o_r}(\theta_{r_0}) = k(R'_{r_{max}}(\theta_{r_0}) - R'_{r_{min}}(\theta_{r_0}))$. $R'_{r_{max}}(\theta_{r_0})$ and $R'_{r_{min}}(\theta_{r_0})$ are, respectively, the relative maximum and minimum of R' when varying θ_r as shown in Figure 3. In order to obtain an expression for $n_{FFT_r}(c_{s_r}, c_{o_r}) = n_{FFT_r}(\theta_{r_0})$, $G_r(\vec{r}, \vec{r}_0)$ is computed for a large number of pairs of source and observer points so that $c_{s_r} \in [1, 9]$ and $c_{o_r} \in [0, 160]$. These ranges correspond to realistic scenarios when solving on the boundary of a body such as a train wheel in the frequency range $[0, 10000]$ Hz. The Fourier Transform over θ_r is computed by Gaussian quadrature for circumferential orders from 0 to 500 using 5000 integra-

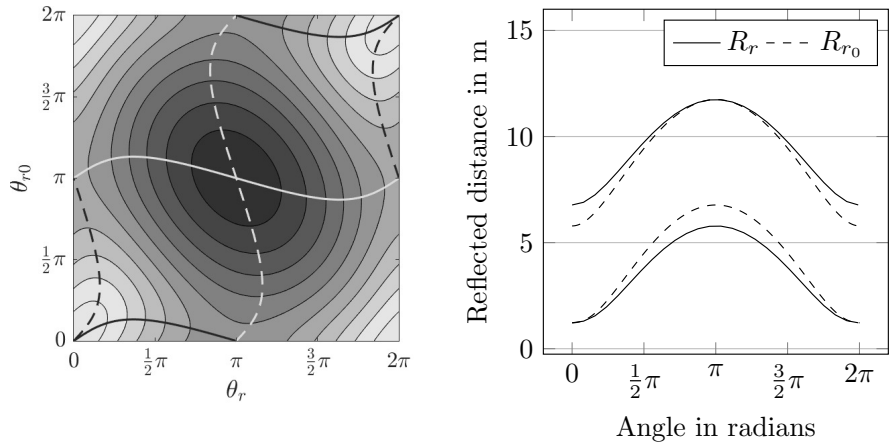

(a) (b)

Figure 3: (a) Reflected distance R'; (b) $R'_{r_{max}}(\theta_{r_0})$, $R'_{r_{min}}(\theta_{r_0})$, $R'_{r_{0_{max}}}(\theta_r)$ and $R'_{r_{0_{min}}}(\theta_r)$

tion points. This computation then used as a reference to determine the specific minimum number of Fourier Transform points n_{FFT_r} for each pair (c_{s_r}, c_{o_r}) to achieve convergence. The condition for the evaluation of the convergence is a relative error not exceeding 10^{-2} for all Fourier coefficients whose value is at least 1% of the maximum Fourier coefficient. These parameter triplets $(n_{FFT_r}, c_{s_r}, c_{o_r})$ are finally used in a curve fitting procedure. The found expression is similar to the one found in [14].

$$n_{FFT_r}(c_{s_r}, c_{o_r}) = 8.45\left(c_{s_r} + \frac{c_{o_r}}{2\pi}\right)^{0.95} + 5 \tag{28}$$

Since the dependency of $G_r(\vec{r}, \vec{r}_0)$ is the same on both angles, the expression of $n_{FFT_{r_0}}(c_{s_{r_0}}, c_{o_{r_0}})$ has to be of the same form. To enable the use of the fast radix-2 FFT algorithm, the next higher number that is a power of two should be used. Wider ranges for c_{s_r} ($[1, 1100]$) and c_{o_r} ($[0, 2000]$) have been studied afterwards to evaluate the robustness of n_{FFT_r} and $n_{FFT_{r_0}}$. The expressions of n_{FFT_r} and $n_{FFT_{r_0}}$ never underestimate the necessary number of Fourier Transform samples. However, when the steepness criterion is large, (e.g. larger than 50, which would be the case when a large body is located very close to the ground or when the observer point is far from the ground), n_{FFT_r} and $n_{FFT_{r_0}}$ start to overestimate the real value. A more complex expression has been developed to limit this overestimation,

$$n_{FFT_r}(c_{s_r}, c_{o_r}) = 7.5\left(c_{s_r}^{1.82} + \left(\frac{c_{o_r}}{2\pi}\right)^{1.88}\right)^{0.52} + 10 \tag{29}$$

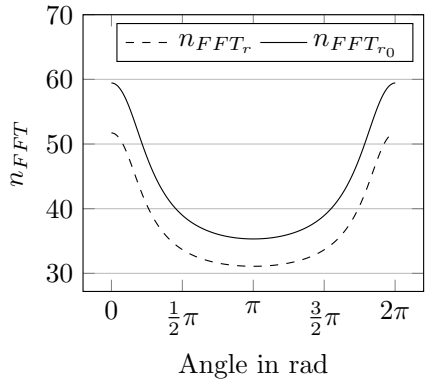

Figure 4: N_{FFT} for different angles

Eq. (28) is thus optimised for solving on the boundary of an object that is under 2 m in diameter and not much closer than one centimetre to the ground. When solving for field points, Eq. (29) is likely more computationally efficient.

Figure 4 represents $n_{FFT_r}(\theta_{r_0})$ and $n_{FFT_{r_0}}(\theta_r)$ for an arbitrarily chosen pair of source and observer point. This case is a representative example to explain how to compute the 2D Fourier Transform. The steps leading to the Fourier coefficients for this case are:

- find $\texttt{min}(\texttt{max}(n_{FFT_r}(\theta_{r_0})),\ \texttt{max}(n_{FFT_{r_0}}(\theta_r)))$
  (here $n_{FFT_r} = 60$ for $\theta_{r_0} = 0$),
- create θ_r from $\texttt{max}(n_{FFT_r}(\theta_{r_0}))$ equally spaced values in $[0, 2\pi[$,
- compute $n_{FFT_{r_0}}(\theta_r)$ for each value of θ_r and create the corresponding θ_{r_0},
- evaluate $G_r(\vec{r}, \vec{r}_0)$ for each value of θ_r and its corresponding values of θ_{r_0},
- calculate the Fourier transform of $G_r(\vec{r}, \vec{r}_0)$ over θ_{r_0} and transform it over θ_r.

Singularities can occur in the computation of H_m and H'_m. The integration points on the line integral 26 need to be deliberately chosen to avoid this.

2.2.4. Discretisation process

The generator is discretised using quadratic line elements. Any point on the generator can be described by the following coordinates

$$x_0 = \mathbf{N}(\xi)\vec{\mathrm{x}}_e \text{ and } \ r_0 = \mathbf{N}(\xi)\vec{\mathrm{r}}_e \tag{30}$$

where $\mathbf{N}$ is a matrix containing the second order iso-parametric shape functions, $\vec{\mathrm{x}}_e$ and $\vec{\mathrm{r}}_e$ contain the nodal coordinates of the element to which $\vec{r}_0$ belongs and ξ

is the local element coordinate. $P_m(x_0, r_0)$ and $V_m(x_0, r_0)$ can now be expressed by the same formulation

$$P_m(x_0, r_0) = \mathbf{N}(\xi)\vec{\mathrm{p}}_{e_m} \tag{31}$$
$$V_m(x_0, r_0) = \mathbf{N}(\xi)\vec{\mathrm{v}}_{e_m} \tag{32}$$

with $\vec{\mathrm{p}}_{e_m}$ and $\vec{\mathrm{v}}_{e_m}$ containing the nodal values of the corresponding element e. The line segment dl_0 is expressed as a function of $d\xi$

$$dl_0 = \left\| \begin{array}{c} dx_0 \\ dr_0 \end{array} \right\| = \left\| \begin{array}{c} \frac{dx_0}{d\xi} \\ \frac{dr_0}{d\xi} \end{array} \right\| d\xi = J_e d\xi \tag{33}$$

with the Jacobian J_e. With that, the element formulation in Eq. (26) can be written in the discretised form

$$\begin{aligned} \frac{1}{2}P_m(\vec{r}) = \sum_e \Bigg[& \underbrace{-j\rho\omega \int_{-1}^{1} H_m \mathbf{N}\, r_0 \mathrm{J}_e d\xi}_{\mathbf{G}_{e_m}(\vec{r})} \vec{\mathrm{v}}_{e_m} - \underbrace{\int_{-1}^{1} H'_m \mathbf{N}\, r_0 \mathrm{J}_e d\xi}_{\mathbf{H}_{e_m}(\vec{r})} \vec{\mathrm{p}}_{e_m} \\ & + \sum_p \Bigg[\underbrace{-j\rho\omega \int_{-1}^{1} H_{r_{mp}} \mathbf{N}\, r_0 \mathrm{J}_e d\xi}_{\mathbf{G}_{r_{emp}}(\vec{r})} \vec{\mathrm{v}}_{e_p} - \underbrace{\int_{-1}^{1} H'_{r_{mp}} \mathbf{N}\, r_0 \mathrm{J}_e d\xi}_{\mathbf{H}_{r_{emp}}(\vec{r})} \vec{\mathrm{p}}_{e_p} \Bigg] \Bigg] \\ = & \boxed{\mathbf{G}_m(\vec{r})\vec{\mathrm{v}}_m - \mathbf{H}_m(\vec{r})\vec{\mathrm{p}}_m + \sum_p \left[\mathbf{G}_{r_{mp}}(\vec{r})\vec{\mathrm{v}}_p - \mathbf{H}_{r_{mp}}(\vec{r})\vec{\mathrm{p}}_p \right]}. \end{aligned} \tag{34}$$

The vectors $\vec{\mathrm{p}}_m$, $\vec{\mathrm{p}}_p$, $\vec{\mathrm{v}}_m$ and $\vec{\mathrm{v}}_p$ collect the nodal values on the generator. Assembling the entries of the element matrices $\mathbf{G}_{e_m}(\vec{r})$, $\mathbf{H}_{e_m}(\vec{r})$, $\mathbf{G}_{r_{emp}}(\vec{r})$ and $\mathbf{H}_{r_{emp}}(\vec{r})$ produces the global matrices $\mathbf{G}_m(\vec{r})$, $\mathbf{H}_m(\vec{r})$, $\mathbf{G}_{r_{mp}}(\vec{r})$ and $\mathbf{H}_{r_{mp}}(\vec{r})$. P_m at any point of the generator is now linked to its amplitude at every node of the generator. A collocation scheme is used, with P_{obs} being placed successively on each node on the generator. Eq. (34) is written successively for each location, which leads to a solvable system of equations

$$\boldsymbol{\mathcal{C}}\vec{\mathrm{p}}_m = \boldsymbol{\mathcal{G}}_m\vec{\mathrm{v}}_m - \boldsymbol{\mathcal{H}}^*_m\vec{\mathrm{p}}_m + \sum_p \left[\boldsymbol{\mathcal{G}}_{r_{mp}}\vec{\mathrm{v}}_p - \boldsymbol{\mathcal{H}}^*_{r_{mp}}\vec{\mathrm{p}}_p \right] \tag{35}$$

where each row of $\boldsymbol{\mathcal{G}}_m$ is equal to $\mathbf{G}_m(\vec{r})$ evaluated at the corresponding node, and likewise for $\boldsymbol{\mathcal{H}}^*_m$, $\boldsymbol{\mathcal{G}}_{r_{mp}}$ and $\boldsymbol{\mathcal{H}}_{r_{mp}}$. $\boldsymbol{\mathcal{C}}$ is a diagonal matrix collecting the c coefficients. Since Eq. (35) yields a coupling between the Fourier coefficients P_m, it needs to be written for every circumferential order $m = [1 \cdots M]$ which

results in the system of equations

$$\begin{bmatrix} \boldsymbol{\mathcal{H}}_{11} & \cdots & \boldsymbol{\mathcal{H}}^*_{r_{1m}} & \cdots & \boldsymbol{\mathcal{H}}^*_{r_{1M}} \\ \vdots & & \vdots & & \vdots \\ \boldsymbol{\mathcal{H}}^*_{r_{m1}} & \cdots & \boldsymbol{\mathcal{H}}_{mm} & \cdots & \boldsymbol{\mathcal{H}}^*_{r_{mM}} \\ \vdots & & \vdots & & \vdots \\ \boldsymbol{\mathcal{H}}^*_{r_{M1}} & \cdots & \boldsymbol{\mathcal{H}}^*_{r_{Mm}} & \cdots & \boldsymbol{\mathcal{H}}_{MM} \end{bmatrix} \begin{bmatrix} \vec{\mathrm{p}}_1 \\ \vdots \\ \vec{\mathrm{p}}_m \\ \vdots \\ \vec{\mathrm{p}}_M \end{bmatrix} = \begin{bmatrix} \boldsymbol{\mathcal{G}}_{11} & \cdots & \boldsymbol{\mathcal{G}}_{r_{1m}} & \cdots & \boldsymbol{\mathcal{G}}_{r_{1M}} \\ \vdots & & \vdots & & \vdots \\ \boldsymbol{\mathcal{G}}_{r_{m1}} & \cdots & \boldsymbol{\mathcal{G}}_{mm} & \cdots & \boldsymbol{\mathcal{G}}_{r_{mM}} \\ \vdots & & \vdots & & \vdots \\ \boldsymbol{\mathcal{G}}_{r_{M1}} & \cdots & \boldsymbol{\mathcal{G}}_{r_{Mm}} & \cdots & \boldsymbol{\mathcal{G}}_{MM} \end{bmatrix} \begin{bmatrix} \vec{\mathrm{v}}_1 \\ \vdots \\ \vec{\mathrm{v}}_m \\ \vdots \\ \vec{\mathrm{v}}_M \end{bmatrix}. \tag{36}$$

with $\boldsymbol{\mathcal{H}}_{mm} = \boldsymbol{\mathcal{C}} + \boldsymbol{\mathcal{H}}^*_m + \boldsymbol{\mathcal{H}}^*_{r_{mm}}$ and $\boldsymbol{\mathcal{G}}_{mm} = \boldsymbol{\mathcal{G}}_m + \boldsymbol{\mathcal{G}}_{r_{mm}}$.

The pressure on the boundary can now be solved from Eq. (36) inserting $\vec{\mathrm{v}}_m$ for $m = [1 \cdots M]$ as computed by the WFEM.

2.3. Comparison with Measurements

The validation of the method is conducted in two steps, a validation of the combined WFE and free-field FBEM method, and a validation of the half-space axisymmetric FBEM method. For the first part, a directivity measurement on an axisymmetric metal disk was conducted. The disk with the outside diameter of 22 cm, a central hole with 6 cm diameter and 8 mm thickness was suspended in an anechoic environment as shown in Figure 5. A shaker was used to apply an axial excitation at its outer diameter. The force input and acceleration at the input position were measured. A microphone was then manually positioned in 5 degree increments around the structure, where the 0 to 180 degree axis corresponds to the rotational symmetry axis of the structure. Figure 6 shows the measured and calculated input mobility for the structure. The agreement is considered sufficient. The energy input into the structure is high at the resonance frequencies of the body. Due to the contribution of the shaker noise to the sound pressure at all frequencies, which is not included in the model, deviations of the measured and simulated sound pressure level are found, especially in proximity to the shaker. Thus, the comparison focuses on the resonance frequencies, at which the sound radiation from the structure dominates. Figure 7 shows the comparison of the sound pressure level for some resonance frequencies. In general, these match closely. However, some shifts in angle can be observed, which might be due to imprecisions in the manual positioning. The increasingly complex radiation patterns require a higher accuracy and resolution of the positions with increasing frequencies.

The second part of the validation considers the half-space formulation. Here, a numerical solution is compared to analytical models. The researched geometry is a breathing sphere. A semi-circle with $a = 1$ m diameter functions as the generator. A reflective plane is introduced with a distance of 0.51 m from the axis of rotation. To test the effect of the reflection, a reflection factor of -1 is used, effectively phase-shifting the mirror-image by π rad. The effect is shown in Figure 8 as function of the wavenumber in air relative to the diameter of the sphere ka. For low ka, the structure follows the predicted radiation efficiency of a dipole. This is expected considering the phase relation between the sphere and its mirror image as well as the large wavelength compared to the size of the

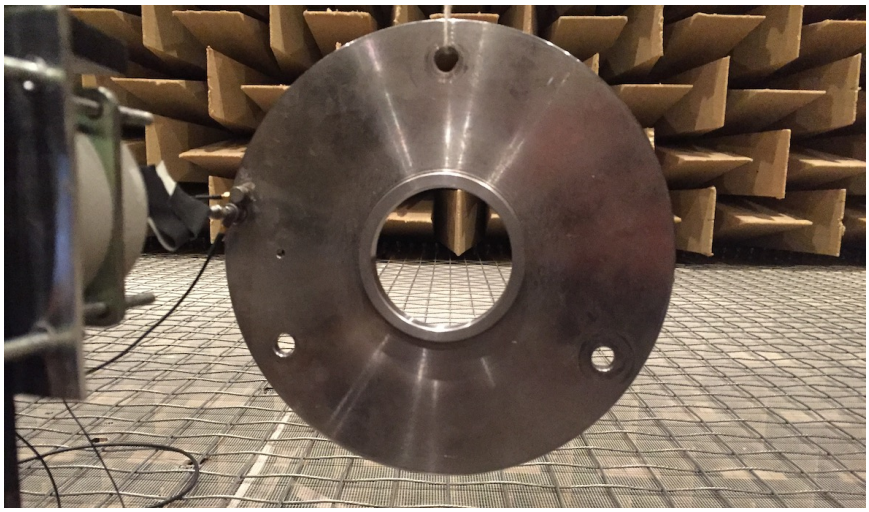

Figure 5: Suspended disk in fully unechoic environment with shaker excitation (left) during validation measurements.

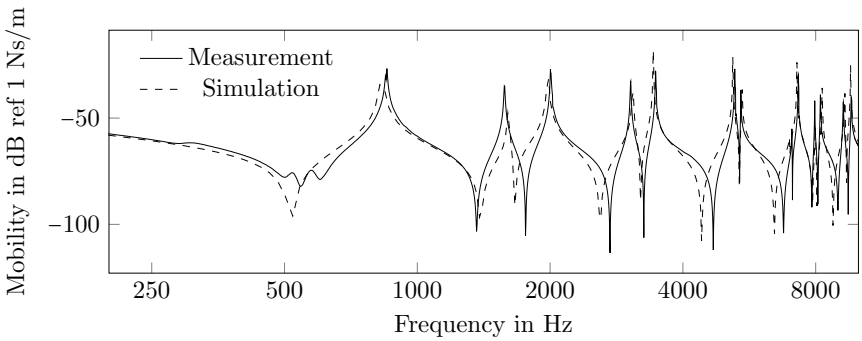

Figure 6: Simulated and measured axial input mobility at the edge of the measured disk.

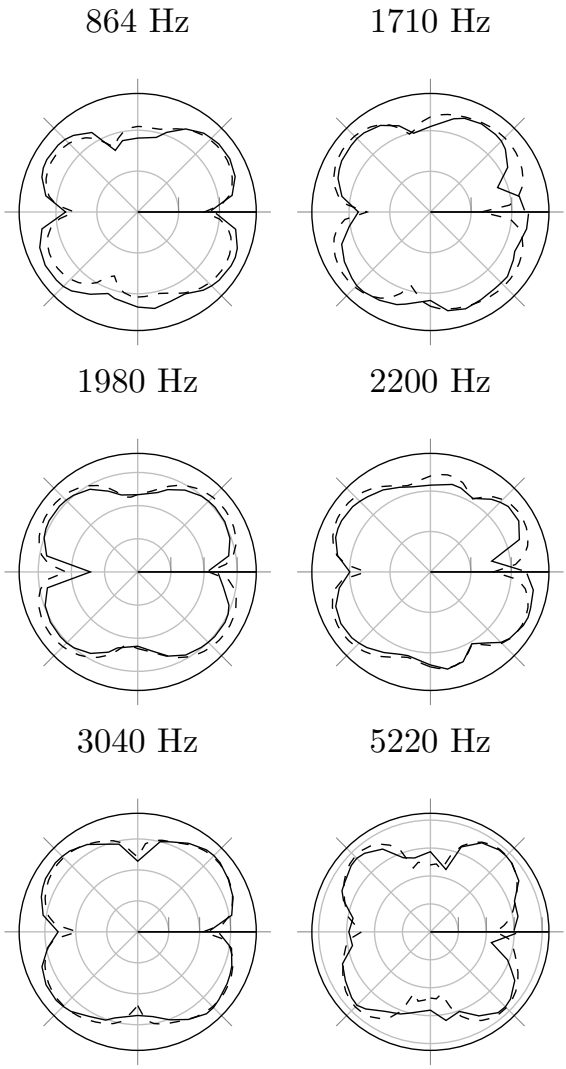

Figure 7: Validation of the free field implementation based on a measurement in an anechoic environment. Sound pressure level in dB, where concentric grid lines correspond to 25 dB steps. (_ _ _) Simulation, (____) Measurement.

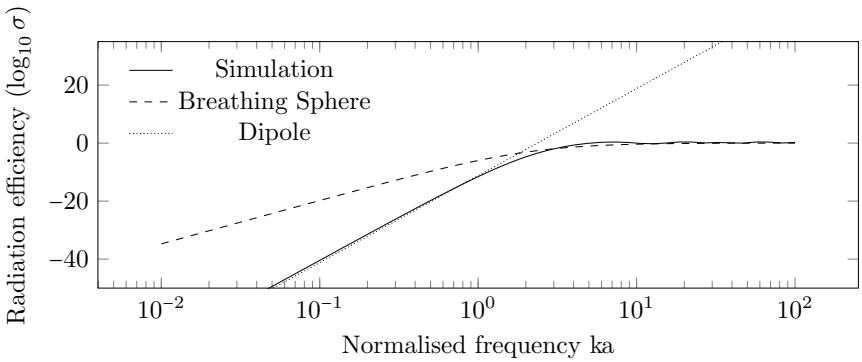

Figure 8: Simulated and analytical solutions for the radiation efficiency.

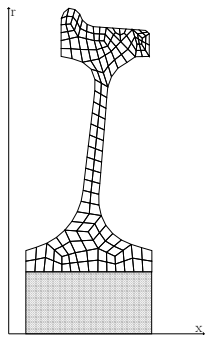

Figure 9: The wheel geometry and FE-Mesh. The grey, dashed rectangle in the bottom represents the axle, providing a fixed constraint on the wheel hub. The x-axis is identical to the axis of symmetry.

radiator. For large ka, the influence of the reflection decreases. Thus, towards high ka, the radiation efficiency approaches that of the breathing sphere.

3. Application on a railway wheel

3.1. Analysis of the structural dynamics

The presented methods are applied on a common railway wheel with a straight web. The wheel geometry is of type BA093 as e.g. used in the noise measurement car (SMW) of DB Systemtechnik, described in [22]. A medium worn profile is assumed with a running radius of 0.47 m rolling radius. Figure 9 shows the geometry and discretisation using 9-node, isoparametric, quadratic elements. As in [20], the extended geometry of the axle is neglected and a rigid connection on the wheel hub is assumed, (dashed rectangle in Figure 9). The dispersion relation for the presented wheel is shown in Figure 10. In the considered frequency range up to 10 kHz, 79 modes are found with up to 13 nodal

diameters. Axial, radial and circumferential modes with an increasing number of nodal circles exist for each number of nodal diameters. The mobility at the contact location is also presented in Figure 10. Expectedly, the axial mobility is mainly determined by the axial modes with a low number of nodal circles. Analogously, radial mode shapes have a dominant influence on the radial mobility. However both directions are coupled due to the non-symmetry of the wheel. The vibration behaviour below 2 kHz is dominated by the axial modes with up to four nodal diameters and up to one nodal circles (see Figure 11a and 11b, with the first radial mode shape (Figure 11d) occuring at 1.3 kHz.

3.2. Radiation Ratios of the free and half-space model

The radiated sound power is evaluated for a harmonic unit force at the contact node, in axial and radial direction, respectively. An analysis similar to [20] is performed by evaluating the radiation ratio

$$\sigma = \frac{P_{rad}}{\rho_0 c_0 S \langle \overline{v^2} \rangle} \tag{37}$$

with the spatially ($\langle\rangle$) and temporally ($\overline{\ }$) averaged squared velocity v on the surface S, the impedance of a plane wave in air $\rho_0 c_0$ and the radiated sound power P_{rad}. The radiation ratio has been evaluated for a wheel in a free field as well as for a half space setup with the lowest point of the wheel 20 cm above an acoustically rigid ground, representing for example the wheel on a rail over a slab track. Figure 12 shows this radiation ratio for six orders for radiation in free field and excitation in axial direction. The low-frequency radiation ratio follows the function described in [20], f^{2n+4} for order n. The behaviour of these orders can therefore be approximated by the radiation of multipoles, with σ tending towards unity once the wavelength in air is in the same magnitude or smaller than the radiating object. The radiation ratio of six orders for a radial force input is shown in Figure 13. The first orders follow the multipole approximation described in [20] for axial modes, f^{2n+4}. This means that the radial force input produces a motion in the axial direction large enough to dominate the radiation. Higher orders follow the predicted pattern of f^{2n+2} for low frequencies, meaning that for those, the radial force input leads to the dominant radiation by radial modes.

Next, the half-space solution is analysed. The wheel is placed in different heights over a reflective plane. Due to the inherent coupling of wavenumbers in the half-space formulation, an analysis of the radiation ratio per order is not meaningful. However, the combined radiation ratio of all included circumferential diameters can be compared. Figure 14 shows this radiation ratio for an axial excitation. The influence of the plane is visible mainly at frequencies below about 170 Hz. Considering that here, the radiation ratio is below 0.01 and decreasing towards lower frequencies, the overall effect of the reflective plane is comparatively small.

A reflecting surface can be close to the outer diameter of the wheel, as it is the case for embedded rails for trams. For a slab track system, this distance

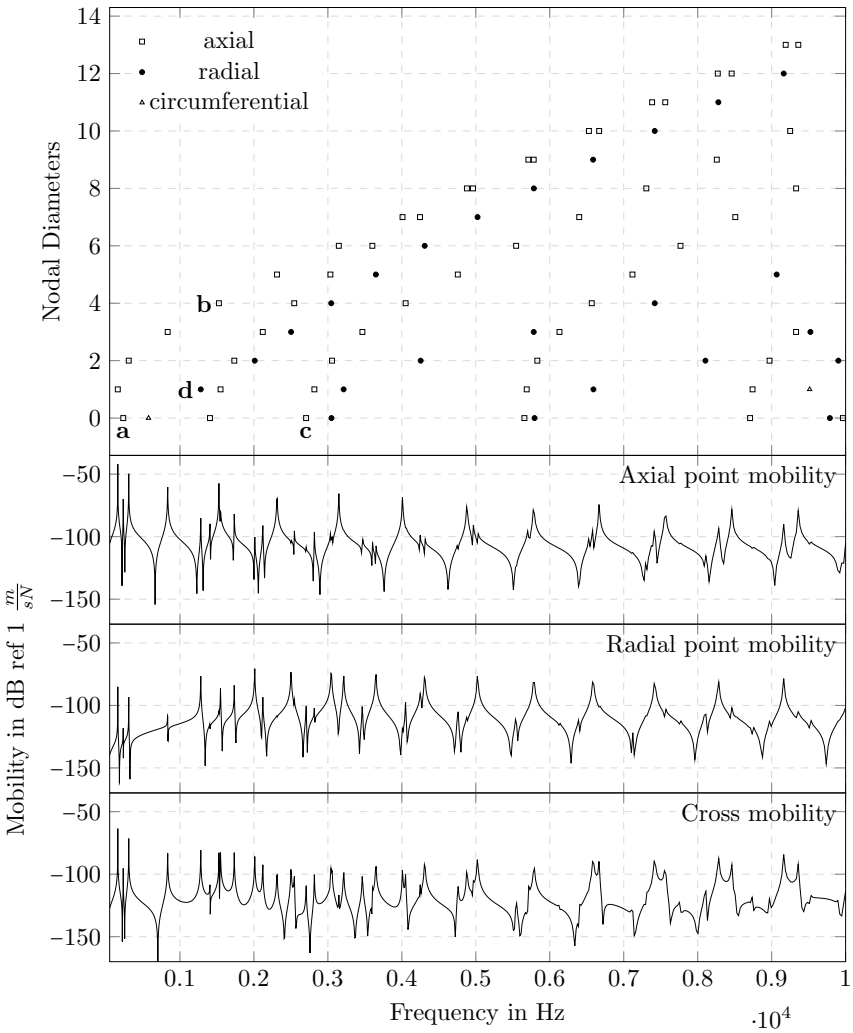

Figure 10: Top: Dispersion relation for the SMW wheel. Marked modes are **a**(0,0,a), **b**(4,0,a), **c**(0,2,a) and **d**(1,0,r). The lower figures show the axial, radial and axial/radial mobility at the contact point.

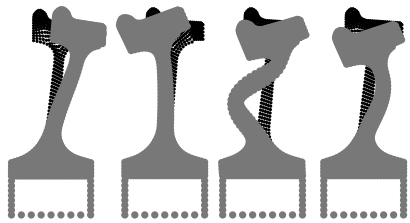

(a) (0,0,a) (b) (4,0,a) (c) (0,2,a) (d) (1,0,r)

Figure 11: The mode shapes of the modes labelled in Figure 10. The notation is (n, m, a/r) with the number of nodal diameters n, the number of nodal circles m and the main direction of motion, axial or radial, respectively.

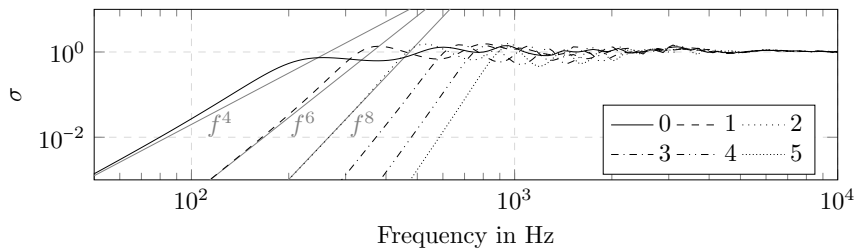

Figure 12: Radiation ratio σ of the wheel for different numbers of nodal diameters and an axial excitation at the contact point. The slopes of functions proportional to f^4, f^6 and f^8 are included as a reference.

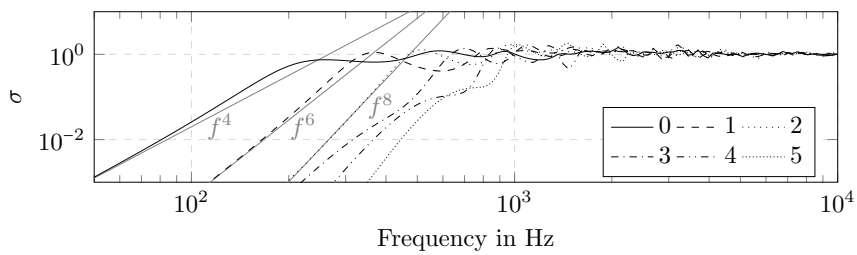

Figure 13: Radiation ratio σ of the wheel for different numbers of nodal diameters and radial excitation at the contact point. The slopes of functions proportional to f^4, f^6 and f^8 are included as a reference.

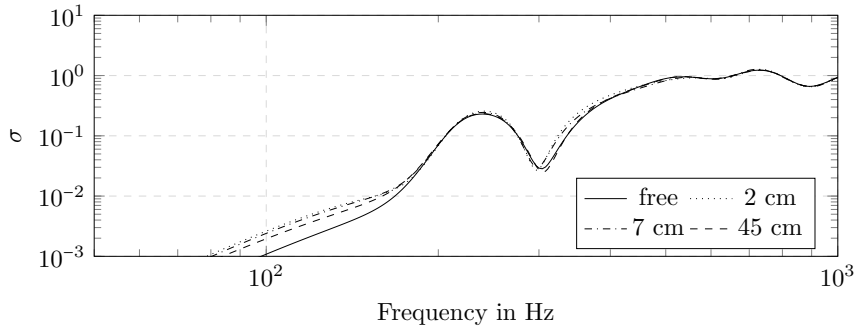

Figure 14: Radiation ratio σ for different heights of the reflective plane.

between the top of the rail and the slab can be around 20 cm to 30 cm. Figure 14 shows the radiation ratio for various distances. The effect is limited to frequencies below about 300 Hz. No significant difference is observed for the selected distances of up to 45 cm.

4. Conclusions

The purpose of this paper is to evaluate the influence of sound radiation from railway wheels over reflective planes. This is of practical interest when researching the influence of the acoustically hard surface of slab tracks on the source strength of wheel radiation. To examine this influence, the existing Fourier series Boundary Element method (FBEM) has been expanded to comprise half space Green's functions. An axisymmetric formulation of the Waveguide Finite Element method (WFEM) has been used for the structural vibrations.

The proposed method of including half space Green's functions in the FBEM has been implemented and validated against numerical models. The combined model of WFEM for structural vibrations and FBEM for sound radiation showed accurate predictions when comparing to laboratory measurements of a real structure. The validated model then successfully reproduced the predictions on the radiation characteristics of a railway wheel in free field from [20]. Furthermore, it was shown that the overall radiation efficiency of a typical railway wheel is low below 150 Hz.

The effect of a reflecting plane on the source strength of a railway wheel was shown to be rather small. Consequently, the assumption used in literature (e.g. [20]) is valid above about 150 Hz. These results confirm that the models currently used to estimate the source strength from railway wheels on ballasted track are also valid approximations for wheels on slab track and even tram wheels on embedded rails. A limitation of the proposed method is the range of researched geometries. The computational cost increases for large bodies that are close to the reflective plane. The presented algorithm has been optimized for bodies in the range of about 1 m diameter and frequencies up to 10 kHz.

5. Acknowledgments

The current study is part of the on-going activities in CHARMEC – Chalmers Railway Mechanics (www.chalmers.se/charmec). Parts of the study have been funded within the European Union's Horizon 2020 research and innovation programme in the project In2Track2 under grant agreement No 826255.

References

[1] O. Zienkiewicz, R. Taylor, J. Zhu, Shells as a Special Case of Three-Dimensional Analysis, in: The Finite Element Method: its Basis and Fundamentals, Butterworth-Heinemann, 2013, pp. 467–491.

[2] Dassault Systèmes Simulia, A. Fallis, D. Techniques, ABAQUS documentation, Abaqus 6.12 (2013).

[3] COMSOL, Introduction to COMSOL Multiphysics 5.3, Manual (2014).

[4] W. Kropp, F. Bécot, S. Barrelet, On the sound radiation from tyres, Acustica 86 (2000) 769–779.

[5] C.-M. Nilsson, Waveguide Finite Elements Applied on a Car Tyre, Ph.D. thesis, Royal Institute of Technology, Stockholm, Sweden, 2004.

[6] C. Hoever, The simulation of car and truck tyre vibrations, rolling resistance and rolling noise, 2014.

[7] J. Winroth, Contact stiffness in tyre / road noise modelling and speed dependencies of tyre / road noise generation mechanisms, Ph.D. thesis, Chalmers University of Technology, 2017.

[8] S. Finnveden, M. Fraggstedt, Waveguide finite elements for curved structures, Journal of Sound and Vibration 312 (2008) 644–671.

[9] H. Brick, M. Ochmann, A half-space BEM for the simulation of sound propagation above an impedance plane, The Journal of the Acoustical Society of America 123 (2008) 3418–3418.

[10] S. H. Schot, Eighty years of Sommerfeld's radiation condition, Historia Mathematica (1992).

[11] A. Bhuddi, M.-L. Gobert, J.-M. Mencik, On the acoustic radiation of axisymmetric fluid-filled pipes using the wave finite element (wfe) method, Journal of Computational Acoustics (2015).

[12] A. F. Seybert, B. Soenarko, F. J. Rizzo, D. J. Shippy, A special integral equation formulation for acoustic radiation and scattering for axisymmetric bodies and boundary conditions, Journal of the Acoustical Society of America (1986).

[13] W. Meyer, W. Bell, B. Zinn, M. Stallybrass, Prediction of the sound field radiated from axisymmetric surfaces., Journal of the Acoustical Society of America 65 (1979) 631–638.

[14] A. H. W. M. Kuijpers, G. Verbeek, J. W. Verheij, An improved acoustic Fourier boundary element method formulation using fast Fourier transform integration, The Journal of the Acoustical Society of America (1997).

[15] B. Soenarko, A boundary element formulation for radiation of acoustic waves from axisymmetric bodies with arbitrary boundary conditions, The Journal of the Acoustical Society of America 93 (1993) 631–639.

[16] P. Juhl, An Axisymmetric Integral Equation Formulation for Free Space Non-Axisymmetric Radiation and Scattering of a Known Incident Wave, Journal of Sound and Vibration 163 (1993) 397–406.

[17] P. J. Remington, Wheel/rail noise-Part IV: Rolling noise, Journal of Sound and Vibration (1976).

[18] P. J. Remington, Wheel/rail rolling noise, I: Theoretical analysis, Journal of the Acoustical Society of America 81 (1987) 1805–1823.

[19] D. J. Thompson, Wheel-rail Noise Generation, part II: Wheel Vibration, Journal of Sound and Vibration 161 (1993) 401–419.

[20] D. J. Thompson, C. J. Jones, Sound radiation from a vibrating railway wheel, Journal of Sound and Vibration 253 (2002) 401–419.

[21] I. Zenzerovic, Time-domain modelling of curve squeal: a fast model for one- and two-point wheel / rail contact, Phd thesis, Chalmers University of Technology, 2017.

[22] A. Pieringer, Acoustic monitoring of rail fauls in the german railway network, 13th International Workshop on Railway Noise (2019).

Appendix A. Finite Element Strain Vector in cylindrical coordinates

In a cylindrical coordinate system, the strain vector is given by

$$\vec{\epsilon}(x,r,\theta) = \left(\frac{\partial u_x}{\partial x}, \quad \frac{\partial u_r}{\partial r}, \quad \frac{1}{r}\frac{\partial u_\theta}{\partial \theta} + \frac{u_r}{r}, \quad \frac{\partial u_r}{\partial x} + \frac{\partial u_x}{\partial r}, \quad \frac{\partial u_\theta}{\partial x} + \frac{1}{r}\frac{\partial u_x}{\partial \theta}, \quad \frac{\partial u_\theta}{\partial r} - \frac{u_\theta}{r} + \frac{1}{r}\frac{\partial u_r}{\partial \theta} \right)^T$$

Thus $\vec{\epsilon}$ can be expressed in term of the nodal displacement $\vec{\mathrm{u}}_e$ by:

$$\vec{\epsilon} = \left(\mathbf{E}_0 + \mathbf{E}_1 \frac{\partial}{\partial \theta} \right) \vec{\mathrm{u}}_e$$

with the tensor operators $\mathbf{E}_0$ and $\mathbf{E}_1$ and the vector $\mathbf{N}$ describing the cross-sectional FE shape functions

$$\mathbf{E}_0(x,r) = \begin{bmatrix} \frac{\partial}{\partial x} & 0 & 0 \\ 0 & \frac{\partial}{\partial r} & 0 \\ 0 & \frac{1}{r} & 0 \\ \frac{\partial}{\partial r} & \frac{\partial}{\partial x} & 0 \\ 0 & 0 & \frac{\partial}{\partial x} \\ 0 & 0 & \frac{\partial}{\partial r} - \frac{1}{r} \end{bmatrix} \mathbf{N}(\xi,\eta) \tag{A.1}$$

and

$$\mathbf{E}_1(x,r) = \begin{bmatrix} 0 & 0 & 0 \\ 0 & 0 & 0 \\ 0 & 0 & \frac{1}{r} \\ 0 & 0 & 0 \\ \frac{1}{r} & 0 & 0 \\ 0 & \frac{1}{r} & 0 \end{bmatrix} \mathbf{N}(\xi,\eta) \tag{A.2}$$

Paper C

Calibration and validation of two models for the dynamic response of slab track using data from a full-scale test rig

Calibration and validation of two models for the dynamic response of slab track using data from a full-scale test rig

Jannik S. Theyssen[a,*], Emil Aggestam[b], Shengyang Zhu[c], Jens C. O. Nielsen[b], Astrid Pieringer[a], Wolfgang Kropp[a]

[a] *Division of Applied Acoustics, Department of Architecture and Civil Engineering, Chalmers University of Technology, 41296 Gothenburg, Sweden*
[b] *Division of Dynamics, Department of Mechanics and Maritime Sciences, Chalmers University of Technology, 41296 Gothenburg, Sweden*
[c] *State Key Laboratory of Traction Power, Southwest Jiaotong University, 111, Section 1 North Second Ring Road Chengdu, 610031, P.R. China*

Abstract

For the development of accurate and reliable simulation models, the procedure of calibration and validation against measurement data is essential. In this paper, a finite element model and a waveguide finite element model of a slab track are calibrated and validated against hammer impact measurement data from a full-scale test rig. The finite element model is three-dimensional, where the rails are modelled as Rayleigh–Timoshenko beams and the concrete slab and support layer are modelled using linear shell elements. In the waveguide finite element model, a constant track cross-section described by two-dimensional finite elements is assumed, and the vibration in the direction perpendicular to the cross-section is described by propagating waves that are decaying exponentially. Measured frequency response functions (FRFs) are compared with the corresponding calculated FRFs from the two modelling approaches. The calibration is conducted in two steps using (i) a parameter study and (ii) a genetic algorithm. For multiple excitation positions and sensor locations, both calibrated models capture the trend of the Single-Input Multiple-Output measurements with rather small deviations compared to the overall dynamic range. This implies that both models can successfully represent the dynamic properties of the test rig and can be considered as validated.

Keywords: Slab Track, Receptance, Hammer impact measurements, Single-Input Multiple-Output, Waveguide finite element, Finite element, Genetic Algorithm.

1. Introduction

In high-speed railway applications, the usage of slab track has increased in recent decades [1, 2]. Compared to ballasted track, slab track has several advantages including reduced

*Corresponding author
Email addresses: jannik.theyssen@chalmers.se (Jannik S. Theyssen), emil.aggestam@chalmers.se (Emil Aggestam), syzhu@swjyu.edu.cn (Shengyang Zhu), jens.nielsen@chalmers.se (Jens C. O. Nielsen), astrid.pieringer@chalmers.se (Astrid Pieringer), wolfgang.kropp@chalmers.se (Wolfgang Kropp)

To be submitted for international publication *May 18, 2020*

maintenance costs and higher track stability. The main drawbacks with slab track are increased construction cost and higher noise levels.

To build optimised slab track structures, the railway industry is dependent on accurate and reliable track models. Depending on the application, different types of models have been developed [3, 4]. Traditionally, finite element models based on beam elements have been used, cf. [5–14]. For applications related to noise radiation modelling, the waveguide finite element method has been applied to model the rail dynamics up to high frequencies, e.g. 4 kHz in Ref. [15] and 80 kHz in Ref. [16]. Recently, several three-dimensional (3D) slab track models have been developed, cf. [17–25]. The main benefit of using a 3D model instead of a two-dimensional (2D) one is that the influence of non-symmetric excitations and support conditions can be studied, whereas the main drawback is the increased computational cost. However, accounting for the periodicity of the track structure and solving the dynamics in the wavenumber domain, cf. [26–29], can decrease this computational cost.

For the development of accurate and reliable simulation models, the procedure of calibration and validation against measurement data is essential. In the literature, different measurement strategies have been described depending on what part of the slab track that was analysed. Often, an impact hammer including an integrated force transducer is used to excite the structure in a Single-Input Multiple-Output (SIMO) test. The response is typically measured using accelerometers [30, 31]. In a study by Cox et al. [32], a dynamic characterisation of different floating slab track systems and direct fixation fastening systems was performed by measuring receptances (displacement over force) in a full-scale test rig. In the test, 12 m long rails were used and boxes of sand were placed at the ends to reduce boundary effects. In 2017, another full-scale test rig was presented by Wang et al. [33]. In their study, the dynamic performance of the China Railway Track System (CRTS) series was analysed by conducting so called wheelset drop tests. Zangeneh et al. [34] analysed the dynamic response of portal frame railway bridges and used a model updating approach to calibrate their finite element model. Finally, Tarifa et al. [35] analysed the fatigue life of reinforced concrete slabs. Their study consisted of several tests including three-point bending tests on full-scale slabs.

In this paper, results from SIMO hammer impact measurements on a section of the CRTS III design are presented. The measurements were performed in the full-scale test rig described by Wang et al. [33]. From the measured receptances, the dynamic behaviour of the CRTS III is analysed. Furthermore, a 3D finite element model and a waveguide finite element model are calibrated and validated with the measurement data. The calibration consists of two steps including (i) a parameter study and (ii) a genetic algorithm. From the comparisons between the models and the measurements, the applicability and accuracy of the presented calibrated and validated slab track models are shown. Finally, the benefits and drawbacks of the two different models are discussed.

2. Measurement description

In Sec. 2.1, the parameter values and geometry of the analysed track section are presented. Details about how the measurements were executed are described in Sec. 2.2.

2.1. Track geometry and parameters

The measurements were performed in the State Key Laboratory of Traction Power of the Southwest Jiaotong University in Chengdu, P.R. China. The full-scale test rig has a total length of about 55 m and includes five sections with different types of slab track and one section with ballasted track. This work focuses on the section with the China Railway Track System III (CRTS III), which has a total length of 16.5 m.

The geometry of the track is presented in Figs. 1 and 2. The considered track section consists of three pre-fabricated concrete slabs. Each concrete slab has a length of 5.5 m, which corresponds to eight rail seat distances. An adjustment layer made of self-compacting concrete (SCC) connects the slabs with the concrete support layer. The support layer rests on a soil layer, which is designed to have homogeneous properties for several meters of depth. The used rail profile, CN60, resembles closely the standard UIC60 rail profile. The fasteners are of type WJ-8, which is a common fastening system on Chinese ballastless high-speed lines.

Deviations in geometry and boundary conditions between the test rig and the models need to be considered in the model validation. One such deviation is that the rails are discontinuous within the investigated section of the track. The rail segments are joined using suspended rail joints (fishplates) with six bolts, see Figs. 2 and 3. The locations of the rail discontinuities are about three rail seat distances away from either end of the CRTS III section. A thin concrete floor resting on the soil is cast on both sides of the concrete support layer (not accounted for in the models). Furthermore, the exact properties of the connection between each pair of concrete slabs are unclear.

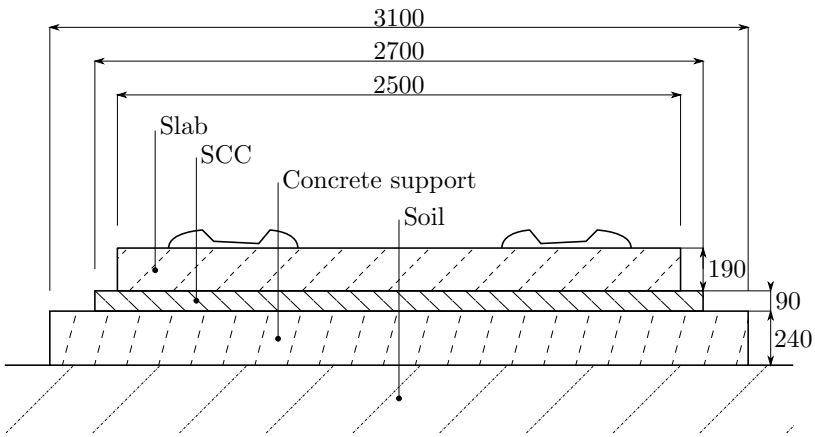

Fig. 1: Cross-section and dimensions of the CRTS III track section (in mm).

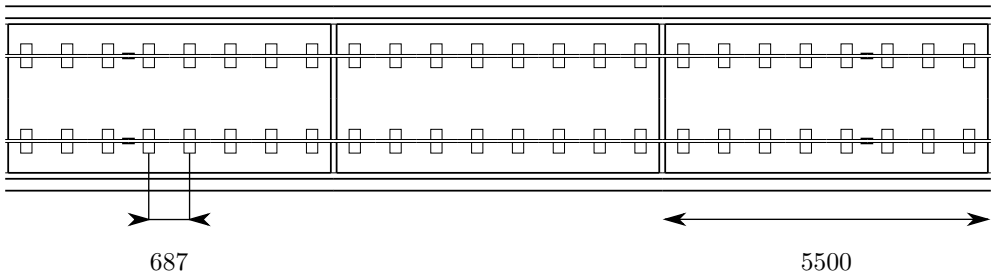

Fig. 2: Top view of the considered track section. The rail discontinuities are located on the outer slabs. The sensors and hammer excitations were placed on the middle slab.

Parameter	Symbol	Unit	CRTS III
Rail mass per unit length	m_{r}	kg	60.6
Rail Young's modulus	E_{r}	GPa	206
Rail cross section area moment of inertia	I_{r}	m^4	$3.22 \cdot 10^{-5}$
Rail pad stiffness	k_{rp}	kN/mm	25
Slab Young's modulus	E_{s}	GPa	36
Slab density	ρ_{s}	$\mathrm{kg/m}^3$	2500
SCC layer Young's modulus	E_{ca}	GPa	28
SCC layer density	ρ_{ca}	$\mathrm{kg/m}^3$	2400
Concrete support layer Young's modulus	E_{cs}	GPa	25.5
Concrete support layer density	ρ_{cs}	$\mathrm{kg/m}^3$	2400
Subgrade stiffness	k_{sg}	MPa/m	190
Subgrade density	ρ_{sg}	$\mathrm{kg/m}^3$	1950

Table 1: Design parameters of the CRTS III track section as described in Ref. [33].

(a)

(b)

Fig. 3: (a) Six-bolt, suspended rail joints connecting the rail sections. (b) Sensor under the rail, next to the rail seat (Sensor 3 as indicated in Fig. 4).

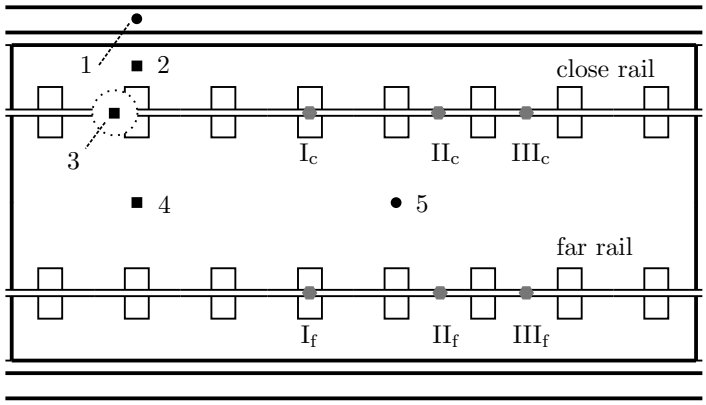

Fig. 4: Locations of the sensors and excitations on the central slab. Sensors are numbered (1–5). Squares indicate tri-axial sensors, whereas circles indicate single-axial, vertical sensors. Sensor 3 is placed below the rail, next to the rail seat. The excitations, indicated by grey hexagons, were carried out both vertically on the railhead and laterally on the inside of the railhead.

2.2. Measurement execution

The aim of the measurements was to obtain transfer functions describing the vibration of the slab for an excitation on the rail. An impulse hammer was used to create an excitation pulse on the rail. The hammer was manually guided to a marked excitation position. A typical amplitude spectrum of the voltage signal of the hammer is shown in Fig. 5. As visible, the steel tip of the hammer produced a fairly flat response up to approximately 7 kHz; the narrow peaks are described below.

The acceleration was measured at five locations on the slab and support layer as indicated in Fig. 4. Each sensor was screwed to a steel plate with dimensions 3 cm x 3 cm x 4 mm, which was glued on the concrete using a two-component glue, see Fig. 3. The measurement equipment is listed in Table 2. All sensors measured the vertical acceleration and the tri-axial sensors were used to additionally measure the lateral acceleration.

Instrument	Type	Quantity
Lance Impact Hammer	LC1304B	1
Dong Hua Tri-axial Accelerometer	1A314E	3
Dytran Accelerometer	3145A	2
m+p international Data Acquisition Unit	VibRunner	1
m+p international Analyzer Software	Version 5.0	

Table 2: Equipment relevant for the measurements.

At each excitation position, the measurements were executed four times. The force signal of the hammer was used to trigger the measurement with a block size of 4 s at a sampling frequency of $f_s = 16\,\mathrm{kHz}$. The recorded time signals were transformed to the frequency domain. Harmonic peaks were found in the spectra as shown in Fig. 5. With the peaks being spaced by 512 Hz and only 1 frequency bin wide, they were considered

non-physical and a moving median operation with a width of 1 Hz was applied to smooth the spectra. From the measured accelerations and the force signal, transfer functions were calculated. The magnitudes of the four measured transfer functions for each transfer path were averaged to produce one magnitude spectrum.

This method of measuring the frequency response has limitations relevant to the model validation. The variance in the manual positioning of the hammer has an effect on the observed response. Fig. 6 shows the variance between four individual measurements and the mean value. Note that there is a variance of about 8 dB for frequencies below 110 Hz with peaks up to 11 dB at 52 Hz, 71 Hz and 100 Hz. The mean receptance used in the following is indicated in black.

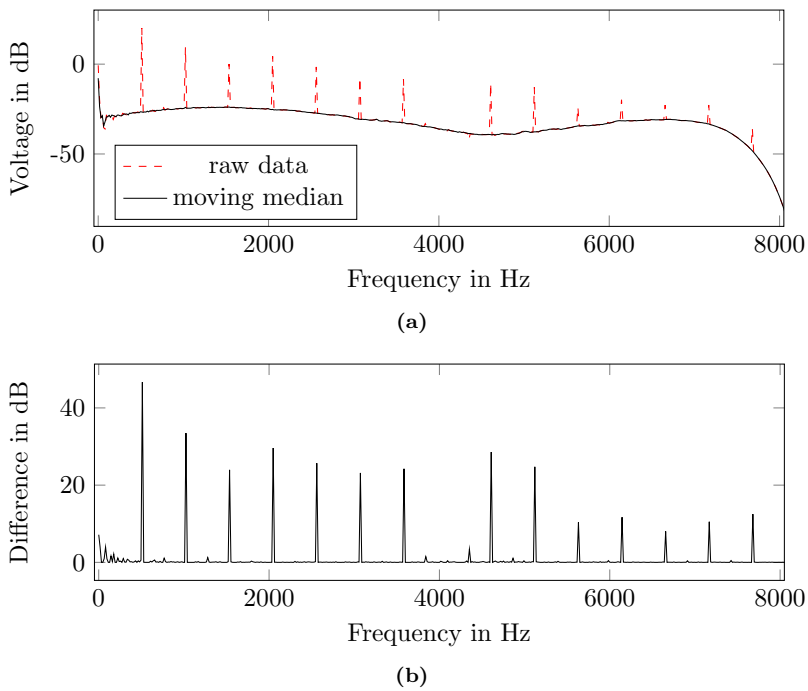

Fig. 5: Signal processing of the frequency response of the hammer signal. (a) Amplitude spectrum before and after applying a four-bin moving median operation. (b) Absolute difference between raw and processed signals.

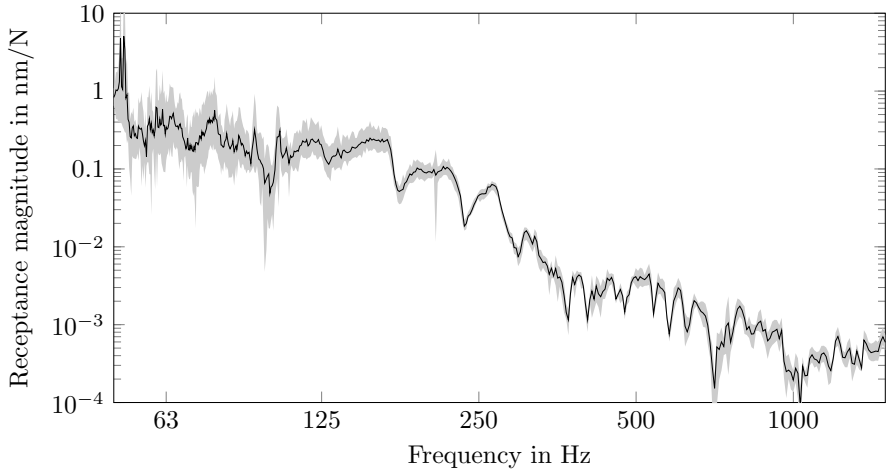

Fig. 6: Variance between the repeated measurements of one transfer path. The measurements were taken for vertical excitations at position I_c, measuring the vertical displacement at sensor 3, see Fig. 4. The black line indicates the mean receptance used in the following.

3. Modelling and tuning of parameters

The measured dynamic responses are compared to simulations with two modelling approaches, namely a discretely coupled waveguide finite element model and a finite element model. In the following, the models are introduced and compared to the measurements. For the calibration and validation, the sensors and excitation positions shown in Fig. 4 were used. Four of the excitation positions (I_c, III_c, I_f and III_f) were used for the calibration, while the other two excitation positions (II_c and II_f) were used for the validation. For both the discretely coupled waveguide finite element model and the finite element model, the calibration was performed using a parametric study and a genetic algorithm. This procedure is described in Sec. 3.1. The description of each model and the simulation results are given in Secs. 3.2 and 3.3.

3.1. Calibration strategy

In the procedure of calibrating the models to the measurement data, the first step is to decide what parameters to include in the calibration process, see Sec. 3.1.1. In this paper, the calibration consists of two steps. In the first step, the stiffness of the rail pad is calibrated by a parameter study, see Sec. 3.1.2. In Sec. 3.1.3, the second step of the calibration is described, where the dampings of the rail pad and soil are determined using a Genetic Algorithm (GA). Finally, since the result of the SIMO measurements is a large number of receptances that are used in the calibration and validation, the information needs to be compressed for visual presentation. In Sec. 3.1.4, a description is given of how the results are visualised in the upcoming parts of the paper.

3.1.1. Parameter selection

Several issues need to be considered when selecting what track parameters to include in the calibration. The most important ones are (i) the influence of the parameter on the

considered track response(s) and (ii) the uncertainty of the parameter values. In this paper, the models will be compared to the measurement data in terms of receptances. Hence, it is crucial to select parameters in the calibration that have a significant effect on the receptance characteristics. In addition, there is no need to calibrate a parameter that by its design can be specified with high accuracy.

In general, the stiffness and damping of the support and resilient layers in the track meet both criteria in terms of affecting the receptance significantly and including an inherent uncertainty. From parameter studies (not shown here), it was concluded that the damping of the soil and the stiffness and damping of the rail pad have a significant effect on the receptances in the studied frequency range. Therefore, these parameters are included in the calibration process. Also, the stiffness of the soil has a significant effect on the receptances, but mostly in the low frequency range. From the measurements, it was found that the coherence at these low frequencies was low. Hence, the stiffness of the soil is not included in the calibration process. Further, the influence of the stiffness and damping of the SCC layer is negligible since this layer is significantly stiffer than the rail pad and the soil. The properties describing the SCC layer are, hence, not included in the calibration process.

The rail parameters as well as the density, dimensions, Young's modulus and Poisson's ratio of the concrete parts have a significant effect on the receptances. These properties are, however, not included in the calibration process since their parameter values can be assumed to be specified with relatively high accuracy.

3.1.2. Parameter study

In Sec. 3.1.1, it was concluded that three properties will be included in the calibration process: (a) the stiffness of the rail pad, (b) the damping of the rail pad and (c) the damping of the soil. Note that the number of parameters that will be tuned is different between the finite element (FE) model and the waveguide finite element (WFE) model since both vertical and lateral parameters are included in the WFE model, whereas only vertical parameters are included in the FE model. Consistently for all the measurements with excitation and response in the vertical direction, a mode can be seen around 140–160 Hz. This mode corresponds to the cut-on frequency of a vertical rail bending mode and is strongly affected by the rail pad stiffness. A description of typical rail cross-sectional modes is presented by Thompson [36]. For a given design of ballasted track, the cut-on frequency for this vertical rail bending mode was found to occur at around 200 Hz [30]. The other parameters used in the calibration, i.e. the dampings of the rail pad and soil, will not affect the frequency of this mode (only its magnitude). Hence, in order to reach a good agreement between simulations and measurements around 140–160 Hz, the rail pad stiffness has to be tuned.

The exact resonance frequency of this mode varies slightly for the different measured receptances. Based on an average over all measured receptances, the resonance frequency is 147 Hz. To determine the rail pad stiffness that meets this resonance frequency, a parametric study was conducted for vertical rail pad stiffnesses spanning from 10–50 kN/mm when using the FE model. For each of the considered rail pad stiffnesses, all different receptances in the vertical direction to be used in the calibration were calculated and the average resonance frequency of the mode was determined. The influence of the rail pad stiffness on the frequency of the mode is shown in Fig. 7. From the figure, the best match between the simulation and measurement is achieved if the rail pad stiffness is

$k_{\mathrm{rp}} = 34$ kN/mm. No specification of the lateral rail pad stiffness for this track has been found in the literature. In a preliminary study (not shown here), a genetic algorithm was used with a larger set of parameters, including the vertical and lateral rail pad stiffness. From this study, it was found that the vertical and lateral rail pad stiffnesses typically converged to similar values. Thus, in the WFE model, the same stiffness is used for both the vertical and lateral stiffnesses. Note that this does not conform with specifications for other types of rail pads, as the lateral stiffness is often specified as lower than the vertical one [37].

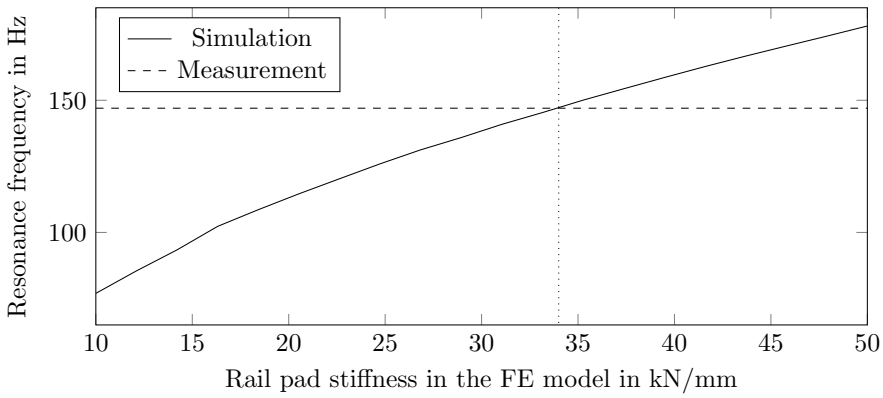

Fig. 7: Location of the cut-on frequency of a vertical rail bending mode as a function of vertical rail pad stiffness.

The calibrated value of the vertical rail pad stiffness (34 kN/mm) is slightly higher than the value provided by Wang et al. [33] (25 kN/mm). However, the stiffness of the rail pad depends on the frequency of excitation, magnitude of the preload, temperature, strain amplitude and strain history [38]. In particular, it has been noted from other measurements that the difference between the static and dynamic rail pad stiffness may vary by a factor of 2–8 [39]. With this in mind, the tuned dynamic rail pad stiffness $k_{\mathrm{rp}} = 34$ kN/mm seems to be reasonable.

3.1.3. Genetic algorithm

The damping values of the rail pad and soil affect the magnitude of the receptance over a wide frequency range. In particular, in the frequency range where the cut-on frequency of a vertical rail bending mode is dominating ($100 < f < 200$ Hz), both the damping values of the rail pad and soil have a significant effect. This implies that varying one of the damping values at a time in a parametric study is not sufficient.

A remedy for more complex calibration problems with several parameters is to use a genetic algorithm (GA). In this paper, the objective function is inspired by the objective function used by Andersson and Abrahamsson [40]. For each considered receptance, the logarithmic difference e between the receptance magnitude of the model H_i^{X} and the

measurement H_i^{A} is calculated as

$$e_{i,k} = \log_{10}\left(\frac{\left|H_i^{\mathrm{X}}(\omega_k)\right|}{\left|H_i^{\mathrm{A}}(\omega_k)\right|}\right), \quad i = 1, 2, \ldots, n_{\mathrm{p}} \quad k = 1, 2, \ldots, n_\omega \tag{1}$$

where n_{p} is the number of receptances used in the calibration and n_ω is the number of considered frequency bins. In this paper, 156 frequency bins were considered, spanning from 25 Hz − 1500 Hz. By collecting all values of $e_{i,k}$ into a vector $\boldsymbol{e}$, the objective function can be written as

$$\boldsymbol{E} = \boldsymbol{e}^{\mathrm{T}}\boldsymbol{Q}\boldsymbol{e} \tag{2}$$

where $\boldsymbol{Q}$ is a non-negative definite weighting matrix with dimensions $n_{\mathrm{p}}n_\omega \times n_{\mathrm{p}}n_\omega$. In this paper, since the damping values of the rail pad and soil have a significant influence on the receptances over a wide frequency range, the weighting matrix is defined as the identity matrix.

By using parallel computations for each individual, the computational cost of a GA can be reduced significantly. In this paper, both models are calibrated using the standard genetic algorithm implemented in Matlab with a population size of 50 and applying 30 iterations. To determine the proper population size and number of iterations, a convergence study was conducted to make sure that the minimum of the objective function was found. In Fig. 8, the convergence of the models can be seen. The objective function has been normalised with the smallest value of the GA in the final iteration. From the figure, it can be seen that the algorithm has converged and that the mean value of the objective function in the final iteration is close to the smallest value.

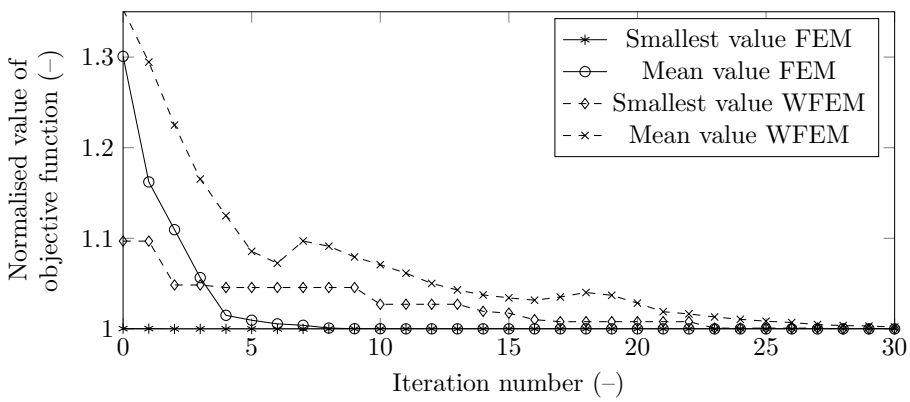

Fig. 8: Convergence of the GA.

For each individual in the genetic algorithm, a new track model has to be generated. For the finite element model, this implies that the Python script that generates the track model in Abaqus has to be called multiple times from Matlab. In Fig. 9, a flowchart of the GA for the finite element model is shown. For the waveguide finite element model, the same steps were used, but Abaqus was not involved. Instead, an in-house Python software was used for the calculation of the track receptance.

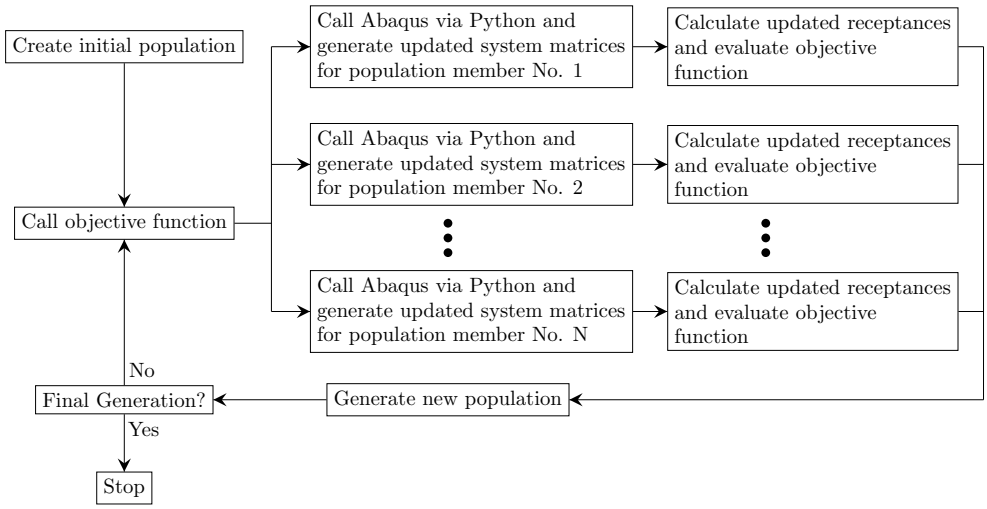

Fig. 9: Flowchart of the GA applied to the finite element model.

3.1.4. Result visualisation

The quality of the match between the measurements and the tuned models is analysed by comparing the individual receptances. However, due to the extensive number of receptances, this information needs to be compressed for visual presentation. In this paper, the similarity between the measured and simulated receptance is determined by calculating their difference in dB, denoted ΔH_{dB}. This similarity measure is calculated for each excitation and response pair as

$$\Delta H_{\mathrm{dB}}(\omega) = 10 \log_{10} \left(\frac{\left| H^{\mathrm{X}}(\omega) \right|}{\left| H^{\mathrm{A}}(\omega) \right|} \right). \tag{3}$$

The difference spectra are then averaged for each one-third octave band and displayed in a surface plot using the colour coding shown in Fig. 10. Here, the brown color indicates an over-estimation by the model, while the blue colour means an under-estimation.

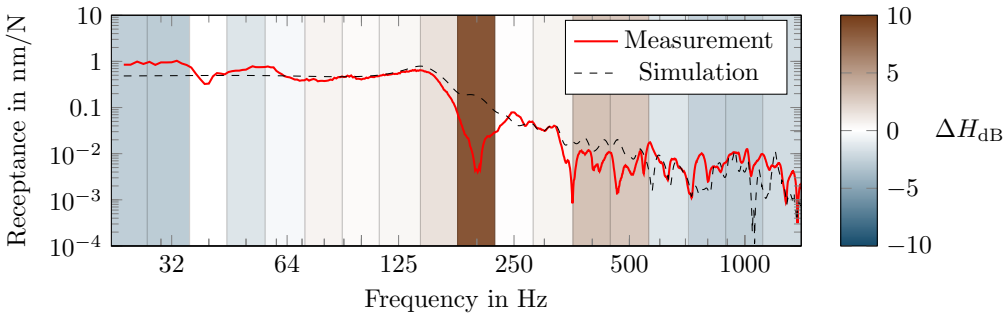

Fig. 10: Receptance magnitude for a vertical excitation at position $\mathrm{III_f}$ to vertical displacement at Sensor 5_v when using the finite element model.

3.2. Discretely coupled waveguide finite element model

The waveguide finite element (WFE) method can be used to model structures that are sufficiently long in one dimension and have a constant cross-section along this dimension [15]. Such a structure acts as a waveguide with propagating, exponentially decaying waves. The WFE method uses the assumption of an infinitely long waveguide. Thus, when discretising the three-dimensional structure, the longer dimension is described by wave functions, and only the cross-section needs to be discretised with two-dimensional finite elements. This process vastly reduces the required number of degrees of freedom (DOFs) in the numerical model.

3.2.1. Model description

Here, the rail and the track are modelled as two separate WFE-models, similar to Ref. [41]. Their cross-sections are meshed using 9-node, quadrilateral isoparametric elements. The dimensions of the track correspond to the dimensions given in Fig. 1. As shown for example in Ref. [15], a partial differential equation relating the displacements and the forces in the cross-section can be derived by using Hamilton's principle. The domain is discretised and the equations are solved for each element. Fig. 11 shows the nodes of the 2D meshes of the rail and the concrete and soil parts of the modelled track cross-section.

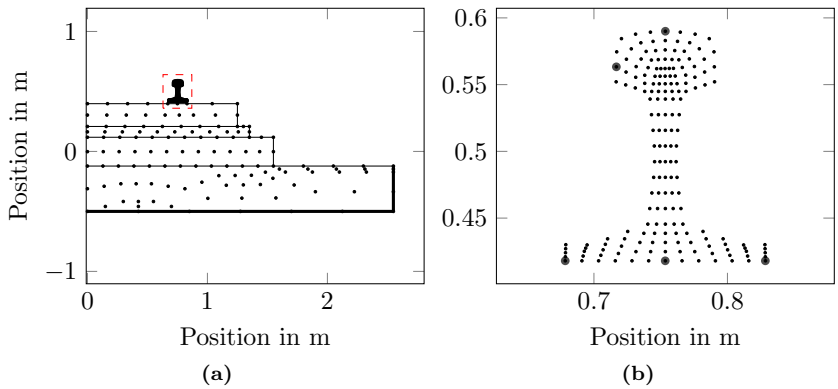

Fig. 11: Nodes of the 2D finite element mesh. (a) Track setup. Note that only half of the symmetric mesh is shown. Top to bottom: Rail, slab, SCC layer, support layer, soil. Thick lines indicate a fixed boundary condition for the nodes on that boundary. The rail mesh is enlarged in (b). The nodes at which loads are applied are marked on the rail head. Likewise, the three nodes connected to the slab via springs are marked on the rail foot.

Assembling the element matrices in the global matrix system gives the expression

$$\left[\boldsymbol{K}_2(-j\kappa)^2 + \boldsymbol{K}_1(-j\kappa) + \boldsymbol{K}_0 - \omega^2\boldsymbol{M}\right]\tilde{\boldsymbol{U}} = \tilde{\boldsymbol{F}} \tag{4}$$

with the mass matrix $\boldsymbol{M}$ and the nodal displacements and forces $\tilde{\boldsymbol{U}}$ and $\tilde{\boldsymbol{F}}$, respectively. The matrices $\boldsymbol{K}_i$ are generalised stiffness matrices. The time dependency $\mathrm{e}^{j\omega t}$ is used with the circular frequency ω. The equation has been transformed to the wavenumber domain using the Fourier transform.

The free response $\tilde{\boldsymbol{F}} = \overrightarrow{0}$ is solved by prescribing a frequency ω and solving the quadratic eigenvalue problem. This generates complex conjugate pairs of eigenvalues corresponding to wavenumbers κ_n, representing propagating, decaying waves, and corresponding left and right eigenvectors $\tilde{\boldsymbol{U}}_{nL}$ and $\tilde{\boldsymbol{U}}_{nR}$.

A superposition of these waves at the origin (index 0) is expressed in the wavenumber domain as

$$\tilde{\boldsymbol{U}}_0 = \sum_n A_n \tilde{\boldsymbol{U}}_{nR}\left(\frac{-1}{Im(\kappa_n) - j(\kappa + Re(\kappa_n))} + \frac{-1}{Im(\kappa_n) + j(\kappa - Re(\kappa_n))}\right) \tag{5}$$

with

$$A_n = j\frac{\tilde{\boldsymbol{U}}_{nL}\tilde{\boldsymbol{F}}_0}{\tilde{\boldsymbol{U}}_{nL}\boldsymbol{D}(\kappa_n)\tilde{\boldsymbol{U}}_{nR}} \tag{6}$$

and

$$\boldsymbol{D}(\kappa_n) = -2\kappa_n\boldsymbol{K}_2 - j\boldsymbol{K}_1. \tag{7}$$

The force vector $\tilde{\boldsymbol{F}}_0$ contains the nodal excitation forces over the length of the rail expressed in the wavenumber domain.

The coupling of the rail with the remaining part of the track is formulated in the spatial domain. The two waveguides are connected in a set of n_c locations x_c. These

do not need to be uniformly spaced [29]. The nodal displacement u at any point i on any of the connected structures ξ is a superposition of the response due to an excitation force $\hat{F}_{\mathrm{e},\xi}$ on the structure and the response due to the reaction forces $\hat{F}_{\mathrm{g}}$ in the coupling points. This can be written as,

$$u_i^{\xi} = H_{i\mathrm{e}}^{\xi}\hat{F}_{\mathrm{e},\xi} - \sum_{g=0}^{n_{\mathrm{c}}} H_{ig}^{\xi}\hat{F}_{\mathrm{g}}. \tag{8}$$

The cross receptance H_{i*}^{ξ} describes the displacement at the location i for a unit force input $\hat{F}_*$. These transfer functions are evaluated individually for the rail and the remaining parts of the track. The structures can be coupled in multiple (m) degrees of freedom in each coupling node. To evaluate the last term in Eq. 8 for one location i, $m \cdot n_{\mathrm{c}}$ transfer functions need to be calculated. The transfer functions $H_{i\mathrm{g}}^{\xi}$ for all contact locations,$i = (x_{\mathrm{c}0}, x_{\mathrm{c}1}, ..., x_{\mathrm{ch}})$ can be assembled into a symmetric matrix $\boldsymbol{H}^{\boldsymbol{\xi}}$ of size $(mn_{\mathrm{c}})^2$.

The rail pad is modelled using linear springs, in which damping is included by assuming a complex stiffness. It is represented by the receptance matrix H^{p} of size $m \cdot m$ such that

$$u_{\mathrm{g}}^{\xi_1} - u_{\mathrm{g}}^{\xi_2} = H^{\mathrm{p}}\hat{F}_{\mathrm{g}}. \tag{9}$$

Inserting Eq. 8 for each structure into Eq. 9 and assembling $\boldsymbol{H}^{\mathrm{p}}$ produces

$$\left(\boldsymbol{H}^{\boldsymbol{\xi_1}} + \boldsymbol{H}^{\boldsymbol{\xi_2}} + \boldsymbol{H}^{\mathrm{p}}\right)\hat{\boldsymbol{F}} = \boldsymbol{H}_{\mathrm{e}}^{\boldsymbol{\xi}}\hat{F}_{\mathrm{e}} \tag{10}$$

with the vector of nodal reaction forces $\hat{\boldsymbol{F}}$.Note that the excitation term on the right hand side contains only the transfer functions of the structure which is excited. This linear system of equations is solved for $\hat{\boldsymbol{F}}$. To connect this to the wavenumber domain calculation above, the reaction forces are expressed as a wavenumber spectrum at the origin,

$$\tilde{F}_0(k) = \sum_{g=0}^{n_{\mathrm{c}}} \hat{F}_{\mathrm{g}}\, \mathrm{e}^{jkx_{\mathrm{cg}}} \tag{11}$$

which can be introduced as an excitation in Eq. 5. This enables the calculation of the response due to the reaction forces. A harmonic excitation of the coupled system can be implemented by superposing the free response of the excited structure with the response due to the reaction forces.

In this paper, a point load on a node of the mesh is assumed as indicated in Fig. 11 (b). The three nodes across the foot of the rail in which the rail and the slab are coupled are indicated in the same figure. The bodies are coupled in both lateral and vertical directions ($m = 6$). The number of rail seats is chosen to be $n_{\mathrm{c}} = 18$, corresponding to the 18 rail seats in between the fishplates.

In total, 64 transfer functions were included in the calibration of parameters, corresponding to eight excitation positions and eight response positions. The considered excitations are at $\mathrm{I_c}$, $\mathrm{III_c}$, $\mathrm{I_f}$ and $\mathrm{III_f}$ in both the vertical and lateral directions, see Fig. 4. The five sensors shown in Fig. 4, three of which are measuring in both the vertical and lateral directions, are included. The calibration was carried out following the description in Sec. 3.1. As discussed in Sec. 3.1.2, the tuned (vertical and lateral) stiffness of the

rail pad is 34 kN/mm. The upper and lower bounds for the optimisation variables (i.e. the rail pad and soil dampings) presented in Table 3 were chosen based on engineering judgement such that values commonly referenced in literature were enclosed, cf. Ref. [33].

Table 3: Parameters used in the GA for the WFE model.

Parameter	Symbol	Unit	Bounds		Result
			lower	upper	
Rail pad vertical damping	$c_{\mathrm{rp,v}}$	-	0.05	0.50	0.23
Rail pad lateral damping	$c_{\mathrm{rp,l}}$	-	0.05	0.50	0.25
Soil damping	c_{s}	-	0.1	0.60	0.32

The prescribed vertical subgrade stiffness k_{sg} is formulated as a stiffness per unit area ($[k_{\mathrm{sg}}]$ = MPa/m) [33]. Assuming a linear elastic material model with Young's modulus E, the stress σ and strain ε are related by

$$\sigma = E\varepsilon, \text{ with } \sigma = \frac{F}{A} \text{ and } \varepsilon = \frac{\Delta l}{l_0} \tag{12}$$

with a force F that is acting on the material with area A and height l_0. Rearranging to solve for E

$$E = \frac{\sigma}{\varepsilon} = \frac{F l_0}{A \Delta l} = k_{\mathrm{sg}} l_0 \tag{13}$$

gives an approximation of the Young's modulus. In this model, where a subgrade thickness of $l_0 = 0.33$ m was chosen, this evaluates to $E_{\mathrm{sg}} = 62.3$ MPa, which is used in the model.

In a pre-study to the optimisation, it was found that the discontinuities in the rail have a significant effect on the measured response in the slab due to the modal behaviour of the rail section. The resulting additional modes can not be directly modelled with a WFE-approach. In addition to that, the GA tends to smoothen the response (e.g. by increasing the damping), as a strong modal behaviour leads to large penalties in the objective function in the case of a frequency shift between the measured and calculated receptances. A two-step procedure was therefore applied; first, the GA was used to determine a good fit for the response without the additional modes. Then, the rail pad stiffness and damping of one rail seat closest to either end of the rail section was increased by a factor three to introduce a discontinuity in the longitudinal direction and to better approximate the measured responses.

3.2.2. Optimisation results

As described in Sec. 3.1.4, the resulting match between the simulated and measured receptances is visualised by a colour scheme in one-third octave bands. In the following, a selection of these matches is presented.

Fig. 12 shows the transfer functions for three vertical excitations on both rails at different distances to the sensors. Note that the upper three rows correspond to lateral response channels. It is observed that for the 50 Hz one-third octave band and below, the model generally underestimates the response. In the 64 Hz to 125 Hz one-third octave

285 bands, the model tends to slightly overestimate the response for both lateral and vertical channels. Above that, the model tends to slightly underestimate the response.

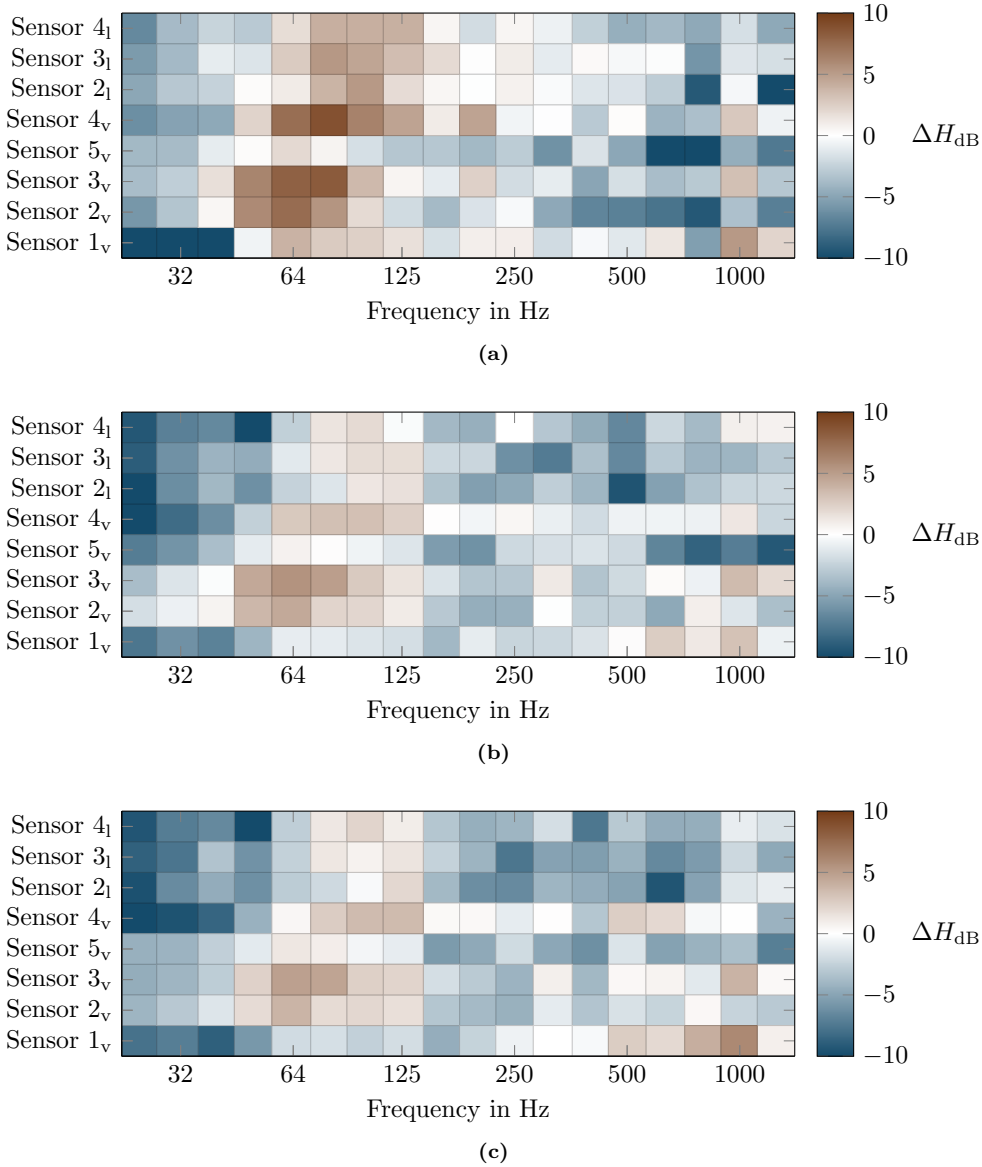

Fig. 12: Similarity measures for vertical excitation at (a) I_f, (b) II_c and (c) III_c.

Figure 13 shows the similarity measure for the same excitation points, but for a lateral excitation. The darker colouring indicates larger differences between the model and the measurements. A fairly close match is observed for the lateral channels at frequencies

above 80 Hz. For lateral excitation, it is noted that the vertical displacements are to varying degrees underestimated by the model.

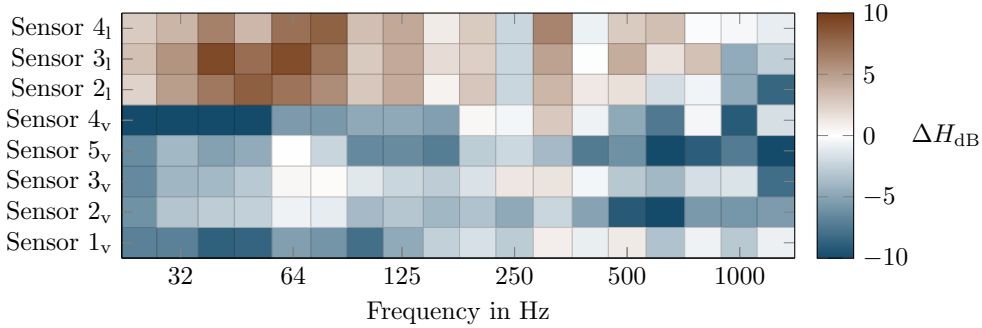

(a)

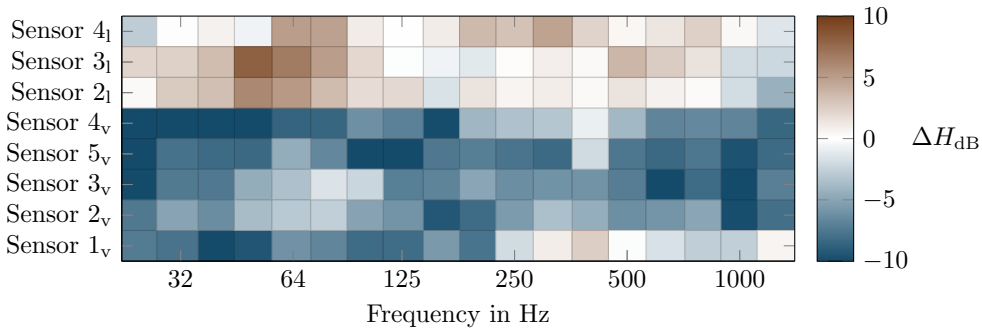

(b)

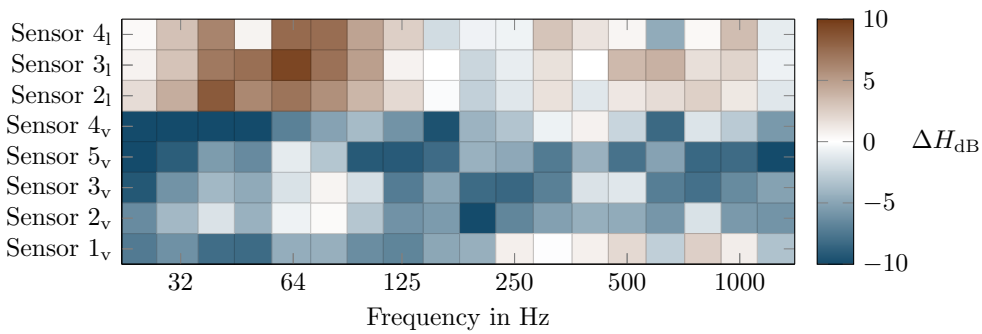

(c)

Fig. 13: Similarity measures for lateral excitation at (a) I_f, (b) II_c and (c) III_c.

In general, it can be noted that larger differences are observed for low frequencies. This is assumed to be a direct result of the low measurement accuracy in that frequency range as described in Sec. 2.2. In each of Figs. 12 and 13 the similarity measures are

shown for three excitation positions are shown for each direction. However, only positions I and III were included in the GA. The central figure, representing excitations at location II, shows matches of similar quality as the other two figures. As the calibrated model is able to predict receptances outside of the calibration process with the same accuracy, the model can be considered to be validated.

A notable observation is that a closer match is achieved when the excitation direction aligns with the measurement direction. This is further investigated in Fig. 14, which presents the receptances for one excitation position and one sensor position, with the excitation and measurement in lateral and vertical directions. In accordance with the findings from Figs. 12 and 13, the single-directional receptances (vertical to vertical or lateral to lateral) match more closely than the cross-directional receptances. It can be assumed that these differences are partly due to the simplifications in the model. The simplifications include the assumption of a continuous slab and representing the complex behaviour of the rail pad by six linear, independently acting springs.

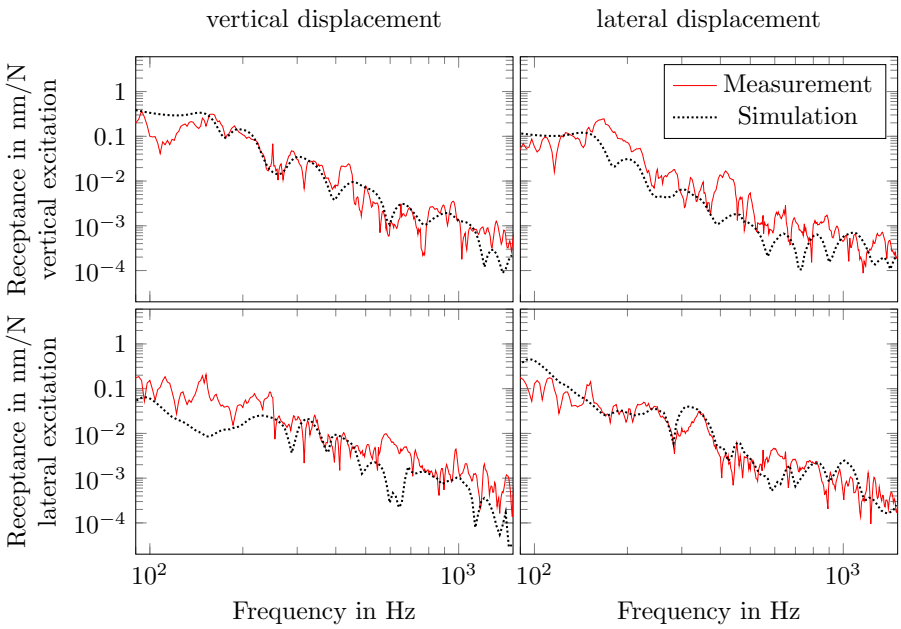

Fig. 14: Comparison of the receptance magnitude for different excitation and measurement directions. The excitation position was III_c and the responses were recorded at Sensor 4.

Finally, the obtained model is used to study the influence of the discontinuous rail. As described in Sec. 3.2.1, the rail pad stiffness of the outer rail pads is increased by a factor three to introduce a discontinuity in the rail support. Fig. 15 visualises this effect. It is observed that the prediction of the model produced by the GA follows the general trend of the measurement. However, when introducing the discontinuity, a visible modal pattern appears starting from about 80 Hz. This modal pattern matches some of the resonances and anti-resonances in the measured response. For this receptance, the updated model seems to resemble more closely with the measurement, especially around

300 Hz.

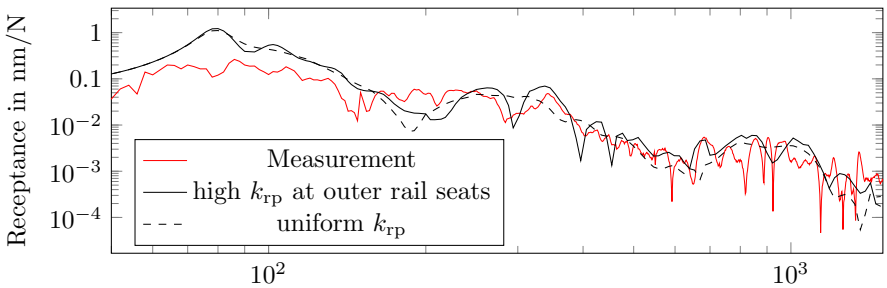

Fig. 15: Effect of introducing a discontinuity in the rail support on the receptance magnitude. This is the transfer function from lateral excitation at position $\mathrm{III_c}$ to lateral displacement at sensor 2.

3.3. Finite element model

The second modelling approach that is considered in this paper is a finite element (FE) model. In this model, only the vertical vibration is considered. In Sec. 3.3.1, the model is described and in Sec. 3.3.2, the results of the calibration and validation are given.

3.3.1. Model description

The parameterised FE model has been developed in Abaqus using Python scripts. The dimensions of the model are according to the CRTS III system and are given in Figs. 1 and 2. The rails are modelled as Rayleigh–Timoshenko beams. Regarding the modelling of the concrete slabs and support layer, it has been verified (not shown here) that the receptance characteristics are similar when using either shell or solid elements. In the upcoming calibration of the model, shell elements were used leading to a lower computational cost. A linear shell element (denoted S4 in Abaqus [42]) was employed and it has been verified (not shown here) that quadratic shell elements give similar results and are not required. Furthermore, the influence of different mesh densities has been investigated. Depending on what frequency range to be studied, the required mesh density varies where a finer mesh is required at higher frequencies. From the investigation, it was concluded that the mesh density used in Fig. 16 with an average element length of 14 cm leads to accurate results.

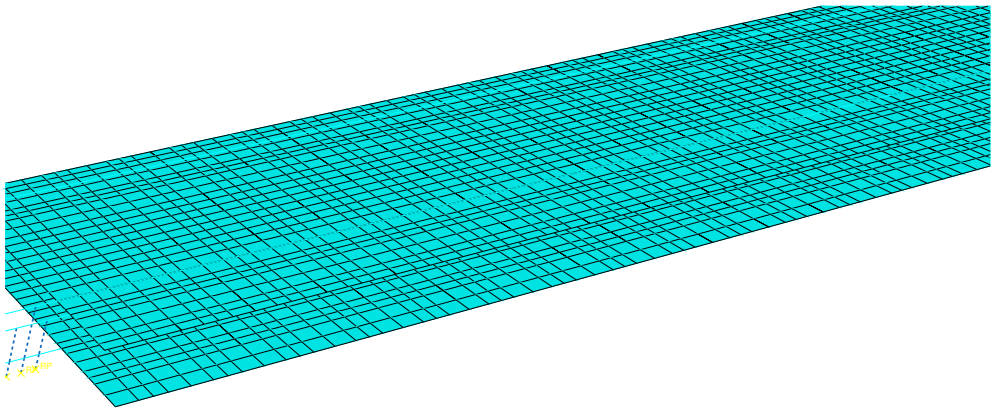

Fig. 16: Three-dimensional parameterised slab track model developed in Abaqus using Python scripts.

The rail pad, soil and SCC layer are modelled as distributed sets of non-interacting springs and viscous dampers. Since the rail pad distributes the force from the rail to the slab over a certain area, a set of springs and viscous dampers acting in parallel is used at each rail seat. This set distributes the load over an area corresponding to the length of the rail pad in the longitudinal direction and the width of the rail in the lateral direction. Also more simplified rail pad models, for example with each rail pad modelled as only one spring and one damper, have been considered and it has been concluded that such simplified models give similar receptances.

To determine the length of the track model, the trade-off between accuracy and computational cost needs to be considered. In the test rig, the CRTS III section has a length of 24 rail seat distances (corresponding to 16.5 m). Before the CRTS III section, there is a section of CRTS II and after the CRTS III section there is a section of a floating slab track (for more details about the test rig, see Sec. 2 and Ref. [33]).In order to reduce the influence of boundary effects in the centre part of the model, six rail seat distances of both the CRTS II and the floating slab track were included in the model giving a total track model length of 24.7 m. Since the track sections of the CRTS II and the floating slab track are included in the model only to reduce boundary effects, they were for simplicity modelled in the same way as the CRTS III track.

As discussed previously, there are several fishplates installed in the test rig. In the model, the fishplates are modelled as beam elements with rectangular cross-section in a similar way as in Ref. [43]. At the joint, the rail is cut and a fishplate is added on either side of the rail. In the test rig, the fishplates were mounted to the rail by using six bolts. In the model, the fishplates are connected to the rail by using a tie constraint at the locations of the bolts. The tie constraint imposes that no relative motion can occur between the rail and fishplates at the locations of the bolts. By comparing the receptances of the track model that includes the fishplates with a simplified model where the rail is continuous, it was verified that additional modes are obtained when fishplates are included (in particular in the high frequency range above 500 Hz).

The calibration and validation of the model are performed using receptances of the track model calculated in the frequency domain. To calculate the receptances, the equa-

Table 4: Viscous damping parameters used in the genetic algorithm for the FEM model.

Parameter	Symbol	Unit	Bounds		Result
			lower	upper	
Rail pad vertical damping	$c_{\mathrm{rp,v}}$	kNs/mm	1	10	6.1
Soil damping	c_{s}	kNs/m^3	10	1000	650

tions of motion are established as

$$\boldsymbol{M}\ddot{\boldsymbol{u}} + \boldsymbol{C}\dot{\boldsymbol{u}} + \boldsymbol{K}\boldsymbol{u} = \boldsymbol{F} \tag{14}$$

where $\boldsymbol{u}$ is a vector containing the DOFs, $\boldsymbol{F}$ contains all external loads and $\boldsymbol{M}$, $\boldsymbol{C}$ and $\boldsymbol{K}$ are the system matrices. Since only steady-state harmonic forces are considered when the receptances are calculated, Eq. 14 can be written as

$$\boldsymbol{E}(\omega)\boldsymbol{u} = \boldsymbol{F} \tag{15}$$

where $\boldsymbol{E}(\omega) = -\omega^2\boldsymbol{M} + j\omega\boldsymbol{C} + \boldsymbol{K}$ is the frequency-dependent dynamic stiffness matrix. To calculate the receptances to be compared with the measurements from the test rig, a vertical harmonic force F is applied at a node in the finite element model that corresponds to a hammer impact position in the measurements. By solving Eq. 15, all displacements are calculated. Let x_i denote a vertical displacement at sensor i. By extracting the displacements x_i from $\boldsymbol{u}$, the receptances are given by

$$H_i(\omega) = \frac{x_i}{F}. \tag{16}$$

3.3.2. Optimisation results

As described in Sec. 3.1, the calibration is performed in two steps. In the first step, the stiffness of the rail pad was tuned using a parameter study and in the second step, the dampings of the rail pad and soil were calibrated using a genetic algorithm (GA). From the parameter study, it was found that a vertical rail pad stiffness of 34 kN/mm should be used. In Table 4, the lower and upper bounds and the optimised results from the GA are shown. To make sure that the selected bounds were reasonable, it was verified that the bounds give stiffness to damping ratios that are in the same order of magnitude as the ratios indicated by Nielsen [44]. Furthermore, it is confirmed that the optimised values of the design variables are not close to any of the bounds.

In Sec. 2, it was described that four excitation locations and five sensors were used in the calibration. For the finite element model, where no lateral dynamics is considered, this means that there are in total 20 receptances that can be used in the calibration. In Fig. 18, one example is shown when comparing the simulation and measurement results. In the figure, also the similarity measure for each one-third octave band is shown.

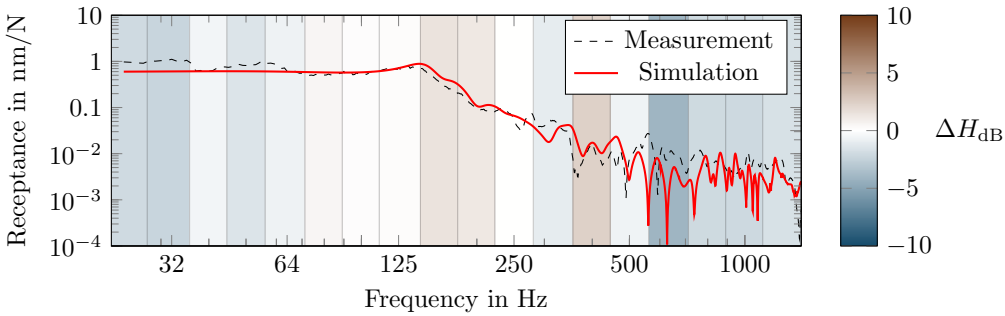

Fig. 17: Comparison of the receptance magnitude between vertical response at Sensor 5 and vertical excitation at I_f.

In Fig. 18, the similarity measure is shown for all of the 20 receptances that were used in the calibration. Each horizontal line corresponds to one receptance as a function of frequency in one-third octave bands. The results from Fig. 17 is shown as the top row in Fig. 18(c). Considering that the dynamic range of the receptance magnitudes is up to 100 dB, it is concluded that there is reasonably good agreement between the simulation and measurement results in Fig. 18. There are, however, some differences between the measurements and simulations. In particular, it can be seen that the model tends to under-estimate the receptances at low frequencies (< 50 Hz). As discussed in Sec. 4, the coherence of the measurements is low in this frequency range, which may explain the discrepancy. In addition, it should be noted that the vertical soil stiffness, which has a strong effect on the receptance in the low-frequency range, is not included in the optimisation. The reason why only the stiffness and damping of the rail pad and damping of the soil is used in the calibration process is described in detail in Sec. 3.1.1.

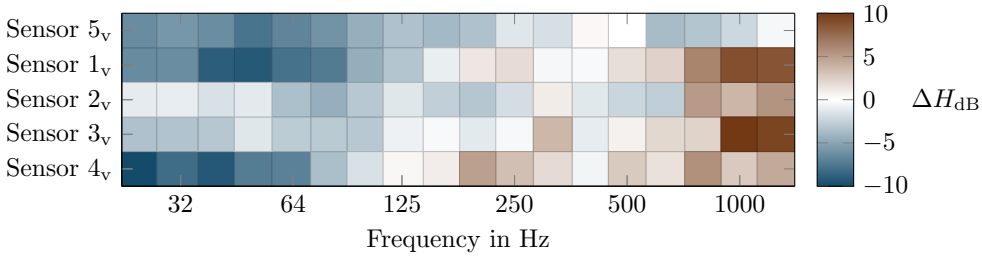

(a)

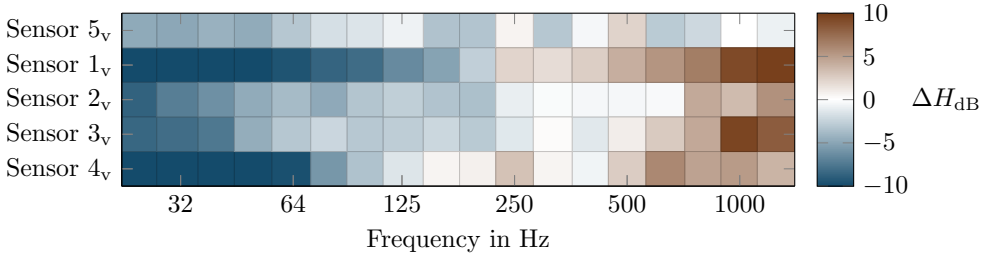

(b)

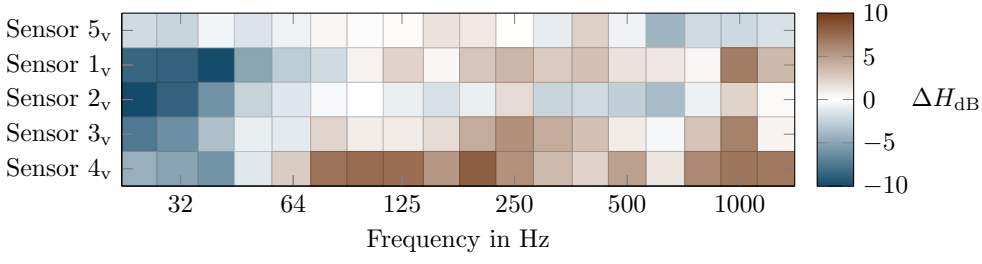

(c)

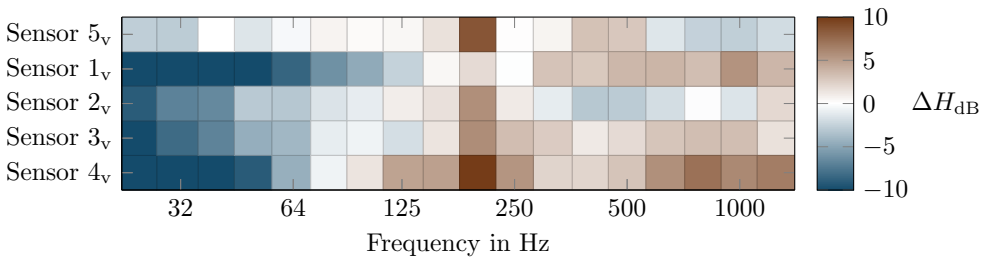

(d)

Fig. 18: Similarity measures for vertical excitation at (a) I_c (b) III_c (c) I_f and (d) III_f.

Using the calibrated parameter values of the track model, a validation of the track model has been conducted. The validation was done by comparing the measurement

data with simulations when considering the excitation positions that were not used in
395 the calibration (see $\mathrm{II_c}$ and $\mathrm{II_f}$ in Fig. 4). In Fig. 19, one example of a cross receptance is shown. Since this validation figure is similar to the calibration figure (Fig. 17) in terms of the similarity measure, the finite element model can be considered as validated. For completeness, Fig. 20 shows the validation version of Fig. 18. The fact that the performance of Figs. 18 and 20 are similar strongly indicates that the model is validated.

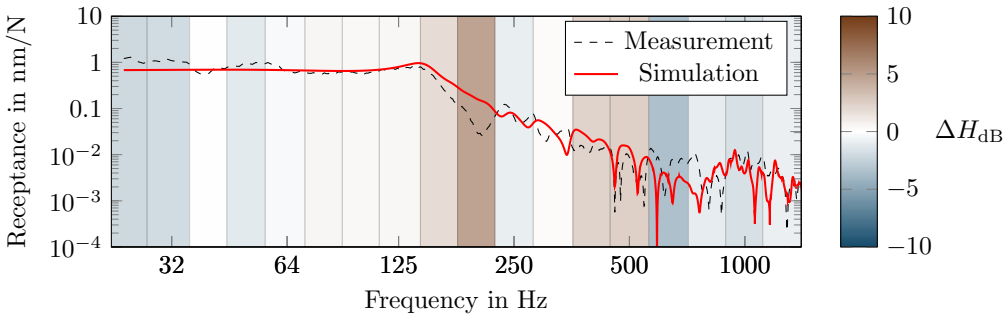

Fig. 19: Receptance between vertical response on Sensor 5 and vertical excitation at $\mathrm{II_f}$.

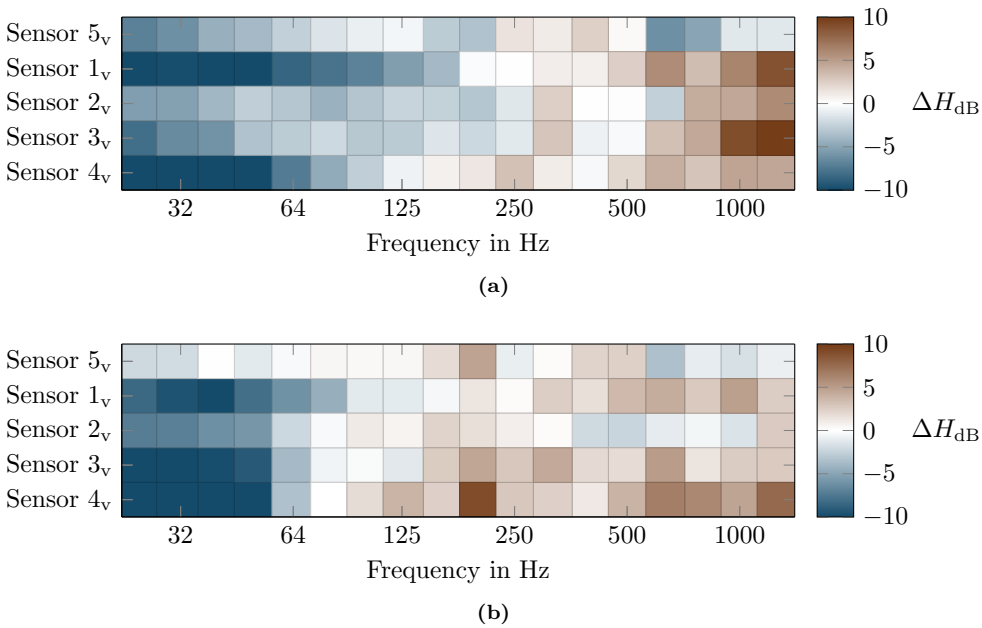

Fig. 20: Similarity measures for vertical excitation at (a) $\mathrm{II_c}$ and (b) $\mathrm{II_f}$.

4. Discussion

This paper presents two approaches for the modelling of the dynamic response of a slab track. Here, a comparison of both methods in terms of their assumptions, advantages, limitations and numerical efficiency is presented.

As both models are based on the finite element method, numerical efficiency is an important factor leading to the need for different simplifications in the models. In the finite element (FE) model, the computational demands were reduced by modelling the SCC-layer and the soil as non-interacting springs and dampers. Modelling the concrete slab and support layer as linear shell elements instead of solid elements decreased the computational cost of the FE-model even more. In the waveguide finite element (WFE) model, the length of the track is represented only by the assumption of propagating waves along its constant cross-section. In addition, since the geometries of the rail and the remaining parts of the track are evaluated independently, the global stiffness matrices are comparatively small. The independent calculation of the free response of the rail furthermore implies that the rail response can be pre-calculated since no rail parameters are altered during the calibration.

These simplifications have several implications regarding the advantages and limitations of each of the models. Due to the three-dimensional mesh of the slab track when using the FE-model, the boundaries between the panel slabs and between track sections can be taken into account. Furthermore, it is possible to include a model of the fish-plates within the structure. As shown in Sec. 3.2, this discontinuity has a large effect on a resonant system such as the rail. The most prominent advantage of the WFE-model is that it can be used at higher frequencies compared to the FE-model. The FE-model, which uses a Rayleigh–Timoshenko description of the rails, gives accurate results up to about 1.5 kHz, whereas a WFE-model of the rails has previously been used even up to 80 kHz [16]. In this paper, frequencies above 1.5 kHz were not considered, since the focus was on the response of the slab. The upper limit was chosen due to the increasing dynamic decoupling of the slab from the vibrations in the rail with increasing frequency. Above 1.5 kHz, this led to a low coherence in the measurements and, more practically, it implies that these frequencies are not as relevant when it comes to e.g. sound radiation from the slab or ground-borne vibration. Finally, as the accuracy of the hammer contact position on the railhead to some extent determines which rail modes are being excited, it is advantageous to be able to specify the input location across the railhead in the WFE-model, especially at higher frequencies. However, this feature was not used in the calibration due to the inherent uncertainty in the hammer placement.

The main reason to reduce the computational cost of the models is the employed Genetic Algorithm (GA). For each iteration in the GA, the receptances need to be evaluated for each individual in the population. The computational demands of calculating the receptances depend on how many excitation positions and frequency lines that are considered. Here, 156 frequency lines were considered in the calibration, with four excitation positions in the FE-model and eight excitation positions in the WFE model. With these settings and one CPU-core, the time to generate updated system matrices of the track and calculate the receptances for the FE-model was about 50 minutes. The corresponding time for the WFE-model was only around one minute. Note that if it is relevant to only tune the rail pad stiffness in the calibration, the receptances of both the rail and the remaining parts of the track in the WFE-model can be pre-calculated

and the calibration can be reduced to a few seconds. When using the FE-model, the computational cost is reduced by using 20 CPU-cores in parallel, see Fig. 9, which means that the average time to generate new system matrices and calculate the receptance is around 2.5 minutes. Finally, this means that running the GA for the FE-model when using 30 iterations and 50 in population size takes around 60 hours.

It is apparent that there exists a trade-off between model complexity (and thus, accuracy) and numerical efficiency. In this paper, the presented models were consciously chosen in order to provide an appropriate compromise. However, improvements could be made to both models to either increase their numerical efficiency or their accuracy. The FE-model can be extended to include features such as lateral dynamics and a solid mesh for the SCC layer, see Ref. [20]. Furthermore, a rather small set of parameters has been included in the GA. In a pre-study to this paper, it was (as expected) found that when including a larger set of track parameters in the GA, it converges towards a slightly closer match than presented here. However, here only the most important parameters were included in the calibration. Another factor that could benefit both models in terms of accuracy is to introduce a more elaborate model of the rail pad, for example by implementing a frequency-dependent stiffness and damping.

Regarding the discrepancies when comparing the models with the measurements, there are also several uncertainties about the test rig and the measurement that can be discussed. First of all, the boundary conditions between the panel slabs are unknown. In addition, the influence of the floor on both sides of the support layer has been neglected in the models as there was no further information about its properties. The influence of the floor might be especially relevant for the lateral dynamics studied in the WFE-model. As mentioned previously, a large uncertainty is the discontinuous rails, leading to uncertain boundary conditions and rail modes due to reflections at the rail ends. This problem was elaborated on in the study performed by Cox et al. [32], where boxes of sand were used to reduce the boundary effects. Further, the contact position of the hammer with the rail influences the excitation of the rail. In this case, there is a possibility for inaccuracies in the order of 1 cm radius around the desired impact point. This inaccuracy is also relevant in terms of the contact angle, which might deviate from the desired purely vertical or lateral direction. Finally, it was observed that the measurements often showed a rather low coherence for frequencies below about 50 Hz. For such low frequencies, it can be assumed that the hammer excitation did not suffice to excite levels of vibrations above the background noise.

Overall, both calibrated models capture the trend of the measurements for multiple excitation positions and sensor locations within a rather small margin compared to the overall dynamic range. This implies that both models can successfully represent the dynamic properties of the considered slab track.

5. Conclusion

In this paper, two models of the dynamic response of a slab track have been calibrated and validated using SIMO measurements in a full-scale test rig. The measurements consisted of hammer impact measurements from which multiple cross-receptances were evaluated. The calibration was divided into two steps. In the first step, the stiffness of the rail pad was tuned based on a parameter study, and in the second step, the dampings of the rail pad and soil were calibrated using a genetic algorithm.

Both models capture the trend of the SIMO measurements for multiple excitation positions and sensor locations within a rather small margin compared to the overall dynamic range. This implies that both models can successfully represent the dynamic properties of the test rig. Regarding the differences between the simulations and measurements, there are several uncertainties. Concerning the measurements, this includes the boundary conditions at the fishplates and between the slab panels, the accuracy of the excitation position and the influence of the adjacent structure on either side of the track. In addition, there are simplifications in the models that need to be considered including the assumption of using non-interacting springs and viscous dampers for several layers of the track in the finite element model and the assumption that the rail and remaining parts of the track are infinite waveguides in the waveguide finite element model.

By using the calibrated and validated models obtained in this paper, a range of investigations and studies can be conducted. In particular, the finite element model will be used to assess the risk of crack initiation in the slab panel, while the waveguide finite element model will be used to model the sound radiation from slab track.

6. Acknowledgments

This work was performed in collaboration between the Swedish National Centre of Excellence CHARMEC (Chalmers Railway Mechanics) in Gothenburg, Sweden, and the Southwest Jiaotong University, Chengdu, China. Parts of the study have been funded within the European Union's Horizon 2020 research and innovation programme in the project In2Track2 under grant agreement No 826255. The simulations were performed using resources at Chalmers Centre for Computational Science and Engineering (C3SE) provided by the Swedish National Infrastructure for Computing (SNIC).

References

[1] C. Esveld, Recent developments in slab track, European Railway Review 9 (2) (2003) 81–85.

[2] P.-E. Gautier, Slab track: Review of existing systems and optimization potentials including very high speed, Construction and Building Materials 92 (2015) 9–15.

[3] K. Knothe, S. Grassie, Modelling of railway track and vehicle/track interaction at high frequencies, Vehicle System Dynamics 22 (3-4) (1993) 209–262.

[4] D. Connolly, G. Kouroussis, O. Laghrouche, C. Ho, M. Forde, Benchmarking railway vibrations – Track, vehicle, ground and building effects, Construction and Building Materials 92 (2015) 64–81.

[5] J. C. O. Nielsen, A. Igeland, Vertical dynamic interaction between train and track – Influence of wheel and track imperfections, Journal of Sound and Vibration 187 (5) (1995) 825–839.

[6] D. J. Thompson, B. Hemsworth, N. Vincent, Experimental validation of the TWINS prediction program for rolling noise, part 1: Description of the model and method, Journal of Sound and Vibration 193 (1) (1996) 123–135.

[7] W. Zhai, X. Sun, A detailed model for investigating vertical interaction between railway vehicle and track, Vehicle System Dynamics 23 (S1) (1994) 603–615.

[8] Z. Li, T. Wu, Modelling and analysis of force transmission in floating-slab track for railways, Proceedings of the Institution of Mechanical Engineers, Part F: Journal of Rail and Rapid Transit 222 (1) (2008) 45–57.

[9] E. Aggestam, J. C. O. Nielsen, R. Bolmsvik, Simulation of vertical dynamic vehicle–track interaction using a two-dimensional slab track model, Vehicle System Dynamics 56 (11) (2018) 1633–1657.

[10] X. Lei, B. Zhang, Analysis of dynamic behavior for slab track of high-speed railway based on vehicle and track elements, Journal of Transportation Engineering 137 (4) (2010) 227–240.

[11] X. Lei, J. Wang, Dynamic analysis of the train and slab track coupling system with finite elements in a moving frame of reference, Journal of Vibration and Control 20 (9) (2014) 1301–1317.

[12] M. Steenbergen, A. Metrikine, C. Esveld, Assessment of design parameters of a slab track railway system from a dynamic viewpoint, Journal of Sound and Vibration 306 (1-2) (2007) 361–371.
[13] X. Yang, S. Gu, S. Zhou, J. Yang, Y. Zhou, S. Lian, Effect of track irregularity on the dynamic response of a slab track under a high-speed train based on the composite track element method, Applied Acoustics 99 (2015) 72–84.
[14] J. Zhang, Y. Zhao, Y. Zhang, X. Jin, W. Zhong, F. W. Williams, D. Kennedy, Non-stationary random vibration of a coupled vehicle–slab track system using a parallel algorithm based on the pseudo excitation method, Proceedings of the Institution of Mechanical Engineers, Part F: Journal of Rail and Rapid Transit 227 (3) (2013) 203–216.
[15] C. M. Nilsson, C. J. C. Jones, D. J. Thompson, J. Ryue, A waveguide finite element and boundary element approach to calculating the sound radiated by railway and tram rails, Journal of Sound and Vibration 321 (3-5) (2009) 813–836.
[16] J. Ryue, D. J. Thompson, P. R. White, D. R. Thompson, Investigations of propagating wave types in railway tracks at high frequencies, Journal of Sound and Vibration 315 (1-2) (2008) 157–175.
[17] W. Zhai, K. Wang, C. Cai, Fundamentals of vehicle–track coupled dynamics, Vehicle System Dynamics 47 (11) (2009) 1349–1376.
[18] W. Zhai, H. Xia, C. Cai, M. Gao, X. Li, X. Guo, N. Zhang, K. Wang, High-speed train–track–bridge dynamic interactions – Part I: Theoretical model and numerical simulation, International Journal of Rail Transportation 1 (1-2) (2013) 3–24.
[19] W. Zhai, S. Wang, N. Zhang, M. Gao, H. Xia, C. Cai, C. Zhao, High-speed train–track–bridge dynamic interactions – Part II: Experimental validation and engineering application, International Journal of Rail Transportation 1 (1-2) (2013) 25–41.
[20] S. Zhu, C. Cai, Stress intensity factors evaluation for through-transverse crack in slab track system under vehicle dynamic load, Engineering Failure Analysis 46 (2014) 219–237.
[21] M. Shahraki, C. Warnakulasooriya, K. J. Witt, Numerical study of transition zone between ballasted and ballastless railway track, Transportation Geotechnics 3 (2015) 58–67.
[22] E. Poveda, C. Y. Rena, J. C. Lancha, G. Ruiz, A numerical study on the fatigue life design of concrete slabs for railway tracks, Engineering Structures 100 (2015) 455–467.
[23] T. Real, C. Zamorano, C. Hernández, J. García, J. Real, Static and dynamic behavior of transitions between different railway track typologies, KSCE Journal of Civil Engineering 20 (4) (2016) 1356–1364.
[24] J. Sadeghi, A. Khajehdezfuly, M. Esmaeili, D. Poorveis, Investigation of rail irregularity effects on wheel/rail dynamic force in slab track: Comparison of two and three dimensional models, Journal of Sound and Vibration 374 (2016) 228–244.
[25] S. Zhu, J. Yang, C. Cai, Z. Pan, W. Zhai, Application of dynamic vibration absorbers in designing a vibration isolation track at low-frequency domain, Proceedings of the Institution of Mechanical Engineers, Part F: Journal of Rail and Rapid Transit 231 (5) (2017) 546–557.
[26] X. Sheng, C. J. C. Jones, M. Petyt, Ground vibration generated by a load moving along a railway track, Journal of Sound and Vibration 228 (1999) 129–156.
[27] X. Sheng, C. J. C. Jones, D. J. Thompson, Responses of infinite periodic structures to moving or stationary harmonic loads, Journal of Sound and Vibration 282 (1-2) (2005) 125–149.
[28] X. Sheng, T. Zhong, Y. Li, Vibration and sound radiation of slab high-speed railway tracks subject to a moving harmonic load, Journal of Sound and Vibration 395 (2017) 160–186.
[29] X. Zhang, D. J. Thompson, Q. Li, D. Kostovasilis, M. G. Toward, G. Squicciarini, J. Ryue, A model of a discretely supported railway track based on a 2.5D finite element approach, Journal of Sound and Vibration 438 (2018) 153–174.
[30] D. Thompson, Chapter 3 - track vibration, in: D. Thompson (Ed.), Railway Noise and Vibration, Elsevier, Oxford, 2009, pp. 29 – 95.
[31] Standard, Swedish Standards Institute, Stockholm, Sweden, 'SS-EN 15461:2008+A1:2010' (2008).
[32] S. Cox, A. Wang, C. Morison, P. Carels, R. Kelly, O. Bewes, A test rig to investigate slab track structures for controlling ground vibration, Journal of Sound and Vibration 293 (3-5) (2006) 901–909.
[33] M. Wang, C. Cai, S. Zhu, W. Zhai, Experimental study on dynamic performance of typical non-ballasted track systems using a full-scale test rig, Proceedings of the Institution of Mechanical Engineers, Part F: Journal of Rail and Rapid Transit 231 (4) (2017) 470–481.
[34] A. Zangeneh, C. Svedholm, A. Andersson, C. Pacoste, R. Karoumi, Dynamic stiffness identification of portal frame bridge–soil system using controlled dynamic testing, Procedia Engineering 199 (2017) 1062–1067.
[35] M. Tarifa, X. Zhang, G. Ruiz, E. Poveda, Full-scale fatigue tests of precast reinforced concrete slabs

for railway tracks, Engineering Structures 100 (2015) 610–621.
[36] D. J. Thompson, Experimental analysis of wave propagation in railway tracks, Journal of Sound and Vibration 203 (5) (1997) 867–888. doi:10.1006/jsvi.1997.0903.
[37] G. Squicciarini, D. J. Thompson, M. G. Toward, R. A. Cottrell, The effect of temperature on railway rolling noise, Proceedings of the Institution of Mechanical Engineers, Part F: Journal of Rail and Rapid Transit 230 (8) (2016) 1777–1789.
[38] D. J. Thompson, W. Van Vliet, J. Verheij, Developments of the indirect method for measuring the high frequency dynamic stiffness of resilient elements, Journal of Sound and Vibration 213 (1) (1998) 169–188.
[39] D. J. Thompson, J. Verheij, The dynamic behaviour of rail fasteners at high frequencies, Applied Acoustics 52 (1) (1997) 1–17.
[40] C. Andersson, T. Abrahamsson, Vertical and lateral track dynamics: Measurements, model and calibration, Tech. rep., Department of Applied Mechanics, Chalmers University of Technology, Gothenburg, Sweden (2003).
[41] J. Theyssen, A. Pieringer, W. Kropp, The influence of track parameters on the sound radiation from slab tracks, paper presented at the International Workshop on Railway Noise, Ghent, Belgium (2019).
[42] Abaqus, Abaqus Documentation, Dassault Systèmes, Providence, RI, USA, 2018.
[43] E. Kabo, J. C. O. Nielsen, A. Ekberg, Prediction of dynamic train-–track interaction and subsequent material deterioration in the presence of insulated rail joints, Vehicle System Dynamics 44 (Supplement) (2006) 718–729.
[44] J. C. O. Nielsen, High-frequency vertical wheel–rail contact forces – Validation of a prediction model by field testing, Wear 265 (9–10) (2008) 1465–1471.